ALMA MATER STUDIORUM
UNIVERSITÀ DI BOLOGNA

Facoltà di Scienze Matematiche Fisiche e Naturali
Dipartimento di Astronomia

Dottorato di Ricerca in Astronomia
Ciclo XXI (2006-2008)

Multiwavelength study of GRB emissions and TORTORA Project

Dottorando:
Giuseppe Greco

Relatore:
Chiar.mi Profs. C. Bartolini, G. Beskin, A. Guarnieri
Co-relatore:
Dott. S. Karpov

Coordinatore:
Chiar.mo Prof. L. Moscardini

Esame Finale Anno 2009

SCUOLA DI DOTTORATO IN SCIENZE MATEMATICHE, FISICHE E ASTRONOMICHE
SETTORE SCIENTIFICO DISCIPLINARE: AREA 02 - SCIENZE FISICHE
FIS/05 ASTRONOMIA E ASTROFISICA

Contents

Introduction

PhD Work Plan

The Phd thesis entitled *Multiwavelength study of GRB emissions and TORTORA Project* concerns my collaboration in TORTORA Project starded during my diploma thesys in 2003. T.O.R.T.O.RA (stands for Telescopio Ottimizzato per la Ricerca dei Transienti Ottici RApidi) was designed to study optical properties of cosmic γ-ray burst with a photometric time-resolution comparable with the strong variability that characterizes the flux-emission at higher energies of these objects. The complete randomness of the angular distribution of γ-ray bursts on the sky forced to build an astronomical instrument with a wide Field of View in order to capture the *unpredictable transients*. For this reason several monitoring system with a considerably large FOV have been built over the years. However, the optical monitoring systems which operated in the past and those still working, like ROTSE, RAPTOR, Pi of the Sky are not able to resolve the temporal structure of prompt optical emission down to timescale shorter than 5–10 seconds. To solve this problem, the design of wide-field optical camera with high time resolution was developed. TORTORA is the second version of a prototype named FAVOR placed at North Caucasus near Russian 6-m telescope. Nowadays, the wide-field optical camera is mounted on top of REM robotic telescope at La-Silla (Chile) and has been operating since May 2006.

The TORTORA project was supported by University of Bologna, (Progetti Pluriennali 2003) by the Presidium of the Russian Academy of Sciences Program and by the essential collaboration of Brera-Merata Observatory.

I discuss the main phases of implementation of TORTORA camera on the top of REM telescope and the principal scientific outputs obtained during the opti-

cal serendipity sky survey. Detailed analysis are been performed for the Prompt Optical Emission occurred simultaneously with naked-eye GRB 080319B that represents the most significant result achieved by this research program.

The high temporal resolution reached by TORTORA optical monitoring-system (0.13 sec exposure time without gap between two consecutive frames) sheds new light on the on the physical mechanisms involved during the stellar black hole formation. For the first time, joining the high TORTORA temporal resolution analysis to the high-energy measurements obtained from satellite programs (SWIFT/BAT and KONUS/WIND), we are able to analyze the different physical components responsible for the prompt-emission using a comparable sampling-time from higher to lower energy.

In detail, the PhD Work Plan is divided in 6 chapter.

- As usual, the first chapter presents a brief introduction to the γ–ray burst (GRB) phenomenon. The argument is summarized by providing a short background on important events that have gradually improved and made to evolve the scientific knowledge about these objects.

- In the second chapter an broad overview of the identified GRB correlation in the literature over the past twenty years is given.

- The possibility to image on time scales of seconds the behavior of transient events that seem to populate the universe at any epochs, has suggested to try to seek additional informations using the rescalated range analysis methods. In particular the use of the Hurst exponent will be extensively covered in Chapter 3 for an homogeneous sample of the γ-light curve detected by BAT/SWIFT.

- Our statistical analysis and the new discovered correlations are shown in chapter 4.

- In the chapter 5 a technical description of the TORTORA and REM complex and their scientific output are presented.

- The sixth chapter presents the complete high resolution photometry of the prompt optical emission occurred in GRB 080319B captured with TORTORA wide-field optical camera mounted on REM robotic 60–cm telescope

located at La Silla (Chile). The analysis of the time variability are discussed in great detail using different statistical approches.

Finally, in the last chapter the general conclusion to our phd work are discussed.

I briefly summarize the main results obtained in this work and the guidelines of the phd thesis.

It is shown that the observational properties of the prompt γ–ray emission do not seem to follow any cosmological evolution trend and they are the manifestation of same physical phenomenon that is self–affinity at every scale and at any epoch of the universe, while the optical data gathered here show a cosmological evolution trend on various intrinsic GRB features. That means that the intrinsic optical afterglow luminosity follows the cosmological evolution of a circumburst environment which determines the optical afterglow luminosity rate. Strong correlation is found between the peak occurred during the afterglow emission, and their redshift. Furthermore, there are correlations between the luminosity, the total energy and the duration of the γ-ray and optical emission separately, which can arise from universal features of the observed lightcurves. Furthermore the field of the Naked-Eye Burst GRB080319B was imaged by TORTORA before, during and after its γ-ray activity with sub-second temporal resolution and discovered its fast optical variability. The similarity of the overall structure of the optical and γ-ray light curves, namely the presence of two stages of emission with different average levels, a nearly simultaneous rise and fall of the emission, suggests that they reflect the same prolonged activity of the inner engine. Moreover the presence of four nearly equidistant peaks in the optical light curve may suggest the periodicity of the inner engine activity. Finally the observational parameters derived for the prompt optical emission ($\sim$ 1 delay between the γ–ray and optical peaks in the rest frame of the source) appear to satisfy the predictions of Li & Waxman, (2008). According to this theory the optical emission could be produced by "residual" collisions at large radii. We rule out the possible interpretation of the optical flash resulted from external shock emission (Zou et al., 2009) as well as that the optical emission may arise from internal forward-reverse shocks (Yu, Wang & Dai 2008).

Chapter 1

Gamma-Ray Burst: An Overview

For theorists who may wish to enter this broad and growing field, I should point out that there are a considerable number of combinations, for example, comets of antimatter falling onto white holes, not yet claimed.

M. Ruderman, 1975.

Gamma Ray Bursts (GRBs) are the most instantaneously powerful explosions in the Universe and are identified as brief, intense and completely unpredictable flashes of high energy γ-rays on the sky, likely associated with the births of stellar-size black holes or rapidly spinning, highly magnetized neutron stars.

In this chapter we present a short general introduction into the field of γ-ray bursts research, summarizing the past and the present status. We give an ensemble view of the GRBs observations to date, both in the prompt emission phase as well as in the afterglow evolution.

1.1 Historical background

GRBs made their first appearance in history during the years of Cold War in the '60s, when the US Defence Department launched a series of spy satellites designed to verify the conditions of the Nuclear Test Ban Treaty, whose signatories, including the United States, Britain, and the Soviet Union, agreed not to test nuclear devices in the atmosphere or in space. Called Vela, from the Spanish verb velar (to watch), the satellites did record short bursts of γ-ray in keV-Mev energy range, lasting from 0.1 up to 30 seconds. Historically the first γ-ray burst was detected on July 2, in 1969.

This became publish information only several years later, in 1973, when Klebesadel, Strong and Olson (Klebesadel et al., 1973) published a report paper.

The results from Vela satellites were quickly confirmed by data from the Soviet Konus satellites. The theoreticians became very interested in the new natural phenomenon and just within a couple of decades more than one hundred GRBs models had been proposed (Nemiroff, 1994). The phenomenon of γ-ray bursts is without precedence in the modern astronomy, having no observed property that would be a direct indicator of their distance and no counterpart object in another wavelength region. Their brief, random appearance only in the γ-ray region has made their study difficult. Most of theoretical models invoke supernovae, neutron stars, flare stars, antimatter effects, white hole and so on. Basically, taking into account the distance scales only, the models can be divided in three main groups: those in which the candidate objects are situated in the Galactic Disc ($\sim$ few hundred parsec), in the halo ($\sim$ tens of kilo–parsec) or at cosmological distances ($\sim$ giga–parsec parsec). Until the 1990s, the large consensus within the scientific community was that GRBs are local events related to the galactic old neutron stars population.

A new era in GRB research opened in 1991 with the launch of Compton Gamma-ray Observatory (CGRO) carrying on board the Burst and Transient Source Experiment (BATSE). The most significant results came from the all-sky survey in which recorded over 2700 bursts: it showed that GRB were essentially isotropically distributed in the sky, with no significant dipole or quadrupole moments (fig.1), suggesting a cosmological distribution (Brings et al., 1996).

The GRB field was revolutionized on February 28, 1997, when the Italian-Dutch satellite BeppoSAX discovered the first afterglow; a X -ray counterpart to

GRB970228 (Costa et al., 1997). In the meantime, GRB970228 had also become the first GRB for which an optical and radio counterparts was found (van Paradijs et al. 1997; Frail et al., 1997). Subsequent deep images (Sahu et al., 1997) confirmed that the burst was hosted by a distant galaxy at a redshift of 0.695.

A huge step forward was made still in 1997, when spectroscopic observations of the afterglow of GRB970508 provided the first redshift determination (Metzger et el., 1997). Accepting that GRBs are extragalactic distant sources, the equivalent isotropic energy implied is huge: 10^{51} – 10^{54} erg (Bloom et al., 2001) Nowadays the fast and accuracy localization of GRBs by Swift mission and its capability to alert fast-slewing robotic telescope within few seconds after burst has provided detailed multi- wavelength measurements of numerous GRBs and their afterglows. The transition phases between the prompt emission and the early afterglow can be studied with great frequency thanks to the capability of Swift satellite to repointing very quickly the X-ray and the UltraViolet/Optical space-telescopes (XRT and UVOT, respectively) at the location of the new burst. Moreover the new generation of the optical monitoring system (they are discussed in detail in chap.3) are able to capture multi-wavelength information before and after the random explosion. In spite of all the growing technological capabilities, much work still needs to be done to get data close the gamma satellite trigger with a high multi-frequency temporal resolution comparable to the fast-random variability that characterizes the prompt emission phases of the GRB phenomenon. To date diagnostics within seconds of GRB formation is only provided in the remarkable case of naked-eye GRB 080319B. At late times the fireball is already decelerated and has entered a self-similar regime, in which precious information about the early ultra-relativistic phase is lost (Zhang et al., 2003). More generally the most timely observations better characterize the behavior of the central–engine which produces the GRB-event (see chap 4).

1.2 Observational Properties: Prompt Emission

In this sections, some of the main temporal and spectral properties of the GRB emission are described. The GRB detection rate for the BATSE-CGRO detector was about one per day during its operation period 1991-2000. Assuming no source evolution, this would correspond to roughly speaking one event per million years

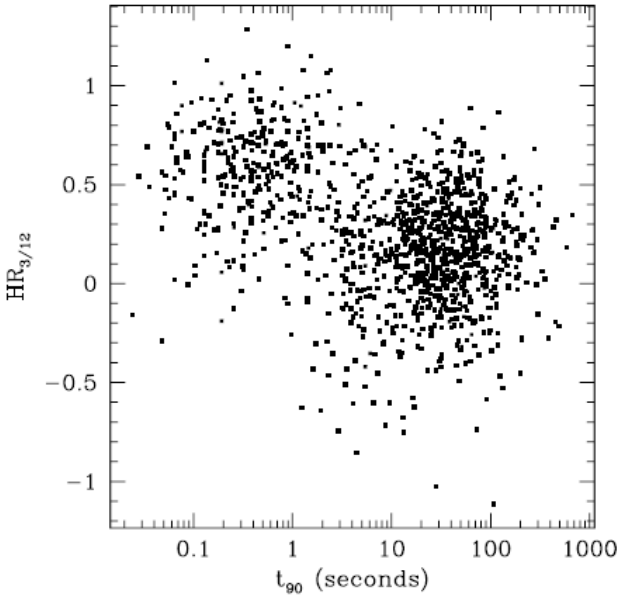

Figure 1.1: The bimodality (Kouveliotou et al. 1993) in hardness ratio and T_{90} is suggestive of two classes of GRBs.

per galaxy (Cohen & Piran, 1995). If the GRBs are beamed, the rate increases by a factor depending on the opening angle and could become even five orders of magnitude greater for highly collimated jets (Rhoads, 1997).

1.2.1 Bimodality distribution

The duration of GRBs ranges from about 5 ms to almost 1000 s. The duration is defined as the time T_{90} (T_{50}) needed to accumulate from 5 % to 95% (from 25% to 75%) of the counts in the 50-300 keV band. The distribution of burst duration is bimodal (Kouveliotou et al., 1993). Those typically lasting two seconds or less and having hard prompt emission spectra (short/hard GRBs) and those lasting typically longer than two seconds and having softer prompt spectra often showing strong hard-to-soft spectral evolution (long/soft GRBs) (Kouveliotou et al., 1993).

The hardness ratio(HR) is defined as the ratio of total counts in two energy bands. In particular for BATSE these are the 100–300 keV and 25– 100 keV bands. This γ–ray hardness is plotted versus observed burst duration for a number of BATSE bursts in Figure 1.1.

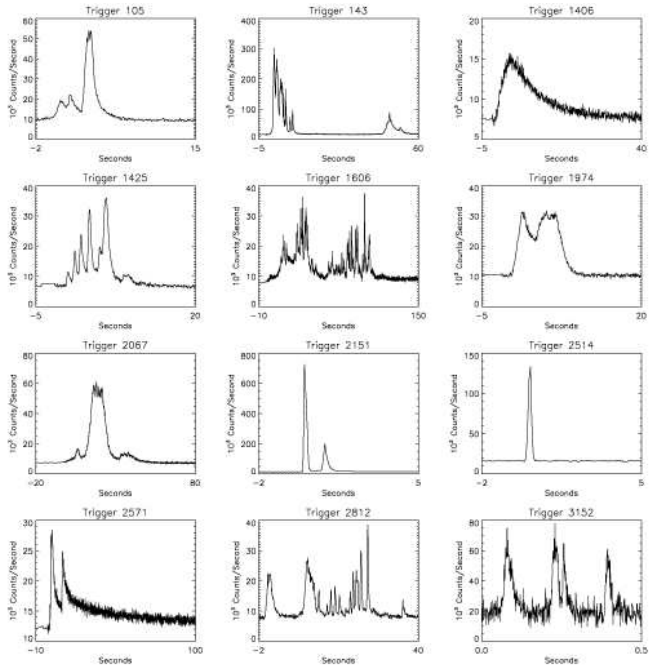

Figure 1.2: A sample of BATSE GRB light curves (from http://www.batse.msfc.nasa.gov/batse/).

1.2.2 Morphology

The time profiles of GRBs exhibit pulse-like shapes of a great diversity (fig. 1.2). Fishman & Meegan (1995) made an attempt to roughly classify them in four classes: a) single pulse or spike events; b) smooth, either single or multiple, well-defined peaks; c) distinct, well-separated episodes of emission; d) very erratic, chaotic and spiky bursts. The variability of the γ-ray emission can reach a scale as low as ms (Walker et al., 2000) suggesting a compact central engine.

1.2.3 Spectrum

One of the key feature of a GRB is its non-thermal spectrum.

The energy flux peaks at a few hundred keV and in many bursts there is a long high energy tail extending in cases up to GeV. The spectrum varies strongly from one burst to another. An excellent phenomenological fit for the spectrum was introduced by Band et al., (1993) using two power laws joined smoothly at a

break energy $(\tilde{\alpha} - \tilde{\beta})E_0$:

$$N(\nu) = N_0 \begin{cases} (h\nu)^{\tilde{\alpha}} \exp(-\frac{h\nu}{E_0}) & \text{for } h\nu < (\tilde{\alpha} - \tilde{\beta})E_0 \ ; \\ [(\tilde{\alpha} - \tilde{\beta})E_0]^{(\tilde{\alpha}-\tilde{\beta})} (h\nu)^{\tilde{\beta}} \exp(\tilde{\beta} - \tilde{\alpha}), & \text{for } h\nu > (\tilde{\alpha} - \tilde{\beta})E_0, \end{cases} . \quad (1.1)$$

There is no particular theoretical model that predicts this spectral shape. Still, this function provides an excellent fit to most of the observed spectra. For most observed values of $\tilde{\alpha}$ and $\tilde{\beta}$, $\nu F_\nu \propto \nu^2 N(\nu)$ peaks at $E_p = (\tilde{\alpha} + 2)E_0$. For about 10% of the bursts the upper slope is larger than -2 and there is no peak for νF_ν within the observed spectrum. Another group of bursts, NHE bursts, (no high energy) Pendleton et al., 1997 does not have a hard component (which is reflected by a very negative value of $\tilde{\beta}$). The typical energy of the observed radiation is E_p. The break frequency and the peak flux frequencies are lower on average for bursts with lower observed flux.

Before the BATSE era various satellites reported observations of absorption and emission lines in few GRBs (Fenimore et al., 1988). In spite of this, more recent data from BATSE detector failed to support previous findings. In other words, there is no clear observational evidence for the existence of spectral features (Band et al., 1997).

1.3 Observational Properties: Afterglows

A rich trove of information on the burst and afterglow physics has come from detailed XRT light curves, starting on average 80-100 s after the trigger. In 98% of cases the X–ray counterpart is detectable in X-Ray Telescope re-pointing. In the same way UVOT satellite telescope has been regularly collecting optical photons $\sim$ 100s after the BAT triggers for a large amount of GRBs. Ground-based robotic telescopes have promptly observed a substantial amount of target. However, the majority of bursts have very dim or undetectable optical afterglows (Roming et al. 2009).

1.3.1 Canonical X-ray afterglow behavior

One of the major discoveries of Swift is the identification of a canonical X-ray afterglow behavior (Nousek et al. 2006; Zhang et al. 2006c see Fig. 1.3). Besides the prompt emission phase (denoted by 0), there are a total of five components in

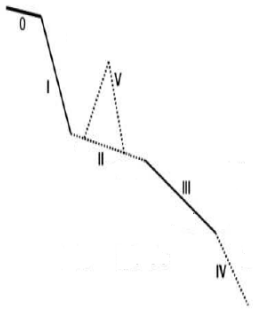

Figure 1.3: A cartoon picture (from Zhang et al. 2006a). Segment I is generally attributed to high latitude emission. Segment II is due to continuous energy injection by the central engine. Segment III is the normal spherical decay of the afterglow. Segment IV is the post-jet break decay. Segment V is due to flares which can occur during any phase.

the X-ray light curves. Not every burst has all five components, so that their light curves may vary from one another. In any case, their afterglow light curve components could be generally fit into this generic picture. The five main components are outlined below:

I. Steep decay phase: Typically smoothly connected to the prompt emission with a temporal decay slope ~ -3 or steeper (sometimes up to ~ -10.

II. Shallow decay phase: Typically with a temporal decay slope ~ -0.5 or flatter extending to $\sim (10^3 - 10^4)$s, at which a temporal break is observed before the normal decay phase.

III. Normal decay phase: Usually with a decay slope ~ -1.2, and usually follows the predictions of the standard afterglow model

IV. Post Jet break phase: Occasionally observed following the normal decay phase, typically with a decay slope ~ -2,

V. X-ray flares: Appear in nearly half of GRB afterglows. In rare cases (e.g. GRB 050502B) the flare fluence could be comparable with that of the prompt emission.

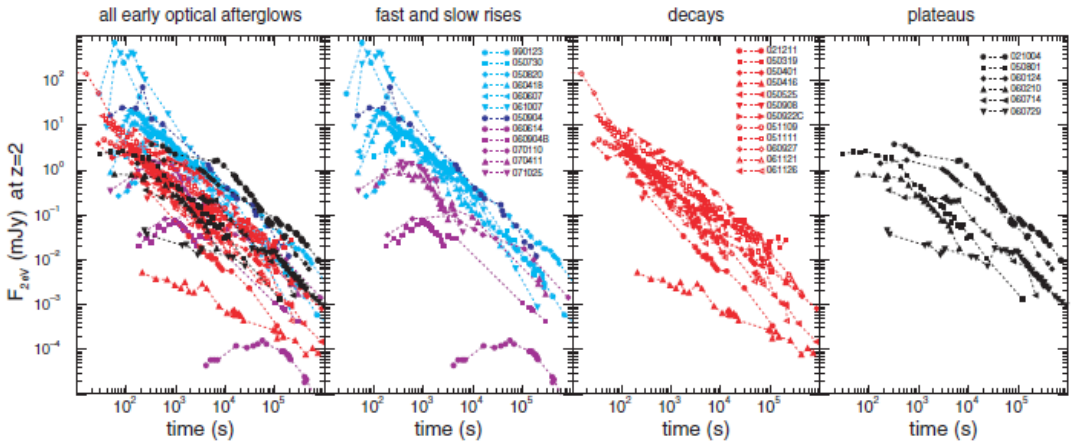

Figure 1.4: four classes for the early optical emission (from Panaitescu & Vestrand 2008).

While elements of this canonical picture is seen in most X-ray afterglows, few afterglows contain all 5 components. Moreover canonical jet breaks are rarely observed in the XRT light curves (Racusin et al.,2007).

1.3.2 NIR/Optical Afterglows

Panaitescu & Vestrand (2008), studying the temporal behaviour of the early optical emission from γ–Ray Burst afterglows, show that is reliable to divided them in four classes: fast-rising with an early peak, slow-rising with a late peak, flat plateaus, and rapid decays since first measurement (fig.1.4).

The overall evolution of the afterglow optical light curves can generally be described well by one or more power-law decays:

$$F(t) \sim t^{-\alpha} \tag{1.2}$$

R-band magnitude at one day is roughly between 17 and 24 which, together with their rapid decline in flux, explains why it is so important a rapid response by the ground based telescopes to search and follow up the afterglow as soon as possible after the trigger.

Although the afterglow light curves can basically be well described with a power-law, a number of mechanisms may alter the decay index in the form of breaks and subsequent steepening in the light curve. Some burst afterglows have even been observed to exhibit extended plateau periods of constant brightness

and/or even periods of significant rebrightening. In addition light curves have, for some bursts, revealed the presence of late-time bumps of varying magnitude, interpreted as due to a supernova component superposed on the afterglow light curve, that rises when the afterglow emission drops down following power-law decay.

1.3.3 Radio Afterglow

Due to a higher mean redshift of Swift bursts than that of pre-Swift bursts, the efficiency to detect radio afterglows is lower in the Swift era. According to GCN Circular statistics $\sim$ 25 radio afterglows were detected among about 300 GRBs detected by Swift in the first 3 years. Short-lived radio transients have been seen in some of these bursts. The first radio afterglow was detected in the case of GRB 970508 (Frail et al., 1997); the fluctuations shown by this radio afterglow for about one month have been interpreted as interstellar scintillation effects, connected with the small angular dimension of the source. Since the distance to this burst was known by the optical afterglow observation, it has been possible to estimate the size required to ease this effect, and hence the expansion velocity of the fireball, that came out to be relativistic (fig 1.5).

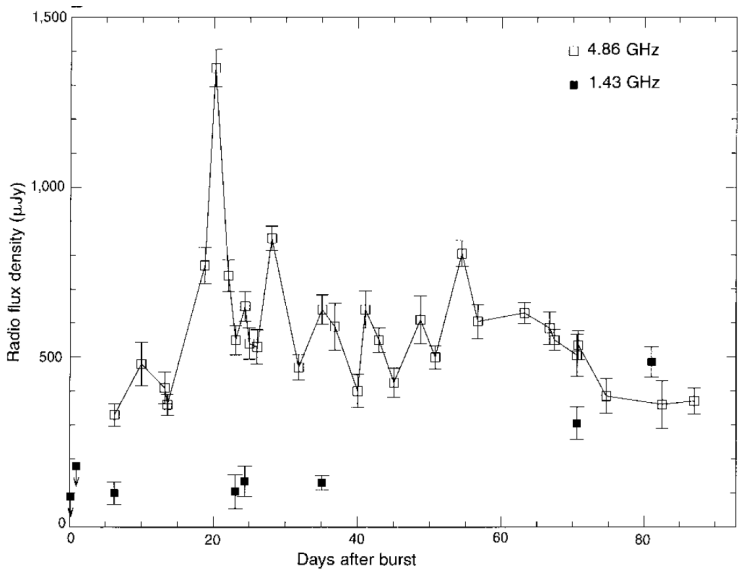

Figure 1.5: Radio variations of the afterglow of GRB970508. From Frail et al., 1997.

1.4 The physics of the GRBs and their afterglows

There are several generally accepted ingredients in all current GRB models. A quick overview of the basic physical concepts of GRB is presented

1.4.1 Compactness and relativistic motion

As reported in the previous section, GRBs show a non-thermal spectrum with a significant high energy tail. A naive calculation implies that the source is optically thick. The fluctuations over a time scale δt imply that the source is smaller than $c\delta t$. Given an observed flux F, a duration T, and an distance d we can estimate the intrinsic energy E. For a typical photon's energy $\bar{E}_\gamma$ this yields a photon density $\approx 4\pi d^2 F/\bar{E}_\gamma c^3 \delta t^2$. two γ rays can annihilate and produce e^+e^- pairs, if the energy in their center of mass is larger than $2m_e c^2$. The optical depth for pair creation is:

$$\tau_{\gamma\gamma} \approx \frac{f_{e^\pm}\sigma_T 4\pi d^2 F}{\bar{E}_\gamma c^2 \delta t} \tag{1.3}$$

where, $f_{e^\pm}$ is a numerical factor denoting the average probability that photon will collide with another photon whose energy is sufficient for pair creation. For typical values and cosmological distances, the resulting optical depth is extremely large $\tau_{e^\pm} \sim 10^{15}$. This is inconsistent with the observed non-thermal spectrum.

The compactness problem can be resolved if the emitting matter is moving relativistically towards the observer. I denote the Lorentz factor of the motion by Γ. Two corrections appear in this case. First, the observed photons are blue shifted and therefore, their energy at the source frame is lower by a factor Γ. Second, the implied size of a source moving towards us with a Lorentz factor Γ is $c\delta t\Gamma^2$.

The first effect modifies $f_{e^\pm}$ by a factor $\Gamma^{-2\alpha}$ where α is the photon's index of the observed γ (namely the number of observed photons per unit energy is proportional to $E^{-\alpha}$.). The second effect modifies the density estimate by a factor Γ^{-4} and it influences the optical depth as Γ^{-2}. Together one finds that for $\alpha \sim 2$ one needs $\Gamma \geq 100$ to obtain an optically thin source.

The requirement that the source would be optically thin can be used to obtain direct limits from specific bursts on the minimal Lorentz factor within those bursts. A complete calculation requires a detailed integration over angular integrals and

over the energy dependent pair production cross section. The minimal Lorentz factor depends also on the maximal photon energy, $E_{\max}$, the upper energy cutoff of the spectrum. Lithwick & Sari (2001) provide a detailed comparison of the different calculations and point out various flaws in some of the previous estimates.

Practically all current GRB models involve a relativistic motion with a Lorentz factor, $\Gamma > 100$. This is essential to overcome the compactness problem. At first this understanding was based only on theoretical arguments. However, now there are direct observational proofs of this concept. It is now generally accepted that both the radio scintillation and the lower frequency self-absorption provide independent estimates of the size of the afterglow, $\sim 10^{17}$cm, two weeks after the burst. These observations imply that the afterglow has indeed expanded relativistically. While all models are based on ultra-relativistic motion, none explains convincingly (this is clearly a subjective statement) how this relativistic motion is attained. There is no agreement even on the nature of the relativistic flow. While in some models the energy is carried out in the form of kinetic energy of baryonic outflow in others it is a Poynting dominated flow or both.

1.4.2 Jets in GRBs

The jets are present in many astrophysical phenomena, such as young stellar objects, microquasars, blazars, active galactic nuclei. In this context, the speculation that jets may appear in GRBs also was quite natural (Rhoads, 1997). The notion jet has two different meanings: geometrical and relativistic (Piran, 2006). In the first case we are dealing with a relativistic flow of matter intrinsically collimated into an angle θ. In the other case, a reference to a relativistic effect is made: the radiation from a source that radiates (isotropically in the comoving frame) and moves with a Lorentz factor Γ toward the observer, is beamed into an angle $\Gamma^{-}1$ around the direction of motion. The angular size of a causally connected region is Γ^{-1}, therefore as long as $\Gamma^{-1} < \theta$ the equations describing the dynamics of a spherical ejecta still holds locally. But, once $\Gamma^{-1} > \theta$, a change is expected in the dynamics; a sideways expansion, with the Lorentz factor decreasing exponentially with radius, it is assumed to take place in the comoving frame.

As a consequence, an achromatic break will appear in the light curve. There are several well observed afterglows with known redshifts for which a break was observed in the light curve and allowed the calculation of the jet opening angle.

When $\Gamma^{-1} < \theta$ there is a balance between the dimming of the surface brightness of the jet and an increasing in the observed emitting area; as soon as $\Gamma^{-1} = \theta$ and later on when $\Gamma^{-1} > \theta$, the emitting area, limited by the size of the cone, stays constant.

Writing the observed specific flux in a general form $F_\nu \propto t^\alpha \nu^\beta$, the isotropic energy in the comoving frame is

$$E_{iso} = 4\pi D_L^2 F (1+z)^{(\alpha-\beta-1)} \tag{1.4}$$

where F is the observed fluence. The resulting energies for GRBs are huge, ranging from 10^{51} up to 10^{54} erg. But if the energy is emitted in some solid angle (a jet), the situation is different.

In the isotropic:

$$E_{iso} = 4\pi \frac{dE}{d\Omega'} \tag{1.5}$$

Assuming a conical collimated flow, with the half-opening angle θ_j, it is obtained:

$$E_{jet} = \Omega \frac{dE}{d\Omega'} \tag{1.6}$$

The relation between isotropic energy and collimated emission is:

$$E_{jet} = E_{iso} \frac{\Omega}{4\pi} \tag{1.7}$$

In spherical coordinates $d\Omega = sin\theta d\theta d\varphi$

$$\Omega = 2 \int_0^{\theta_j} \int_0^{2\pi} \tag{1.8}$$

The factor 2 take in account the two jet oriented in opposite directions. The result is:

$$\Omega = 2\pi(1 - cos\theta_j) \tag{1.9}$$

writing the cosine function in series of Taylor, it is obtained

$$\Omega \approx 2\pi\theta_j^2 \tag{1.10}$$

$$E_{jet} \approx E_{iso}\frac{\theta_j^2}{2} \tag{1.11}$$

An important parameter in the study of GRBs is the event rate. Recent estimations give a value between one and 10 bursts per galaxy at every million years. But, if the emission is collimated, then the true event rate is higher by a factor $4\pi/\Omega$ (Rhoads, 1997).

Most GRBs jet models consider an outflow that is uniform within some finite, well defined opening angle around its symmetry axis, and where the Lorentz factor and energy density drop sharply beyond this opening angle (Rhoads, 1997). Such a uniform jet is referred to as "uniform jet". The possibility that GRBs jets can display an angular structure, where the kinetic energy per unit solid angle and the Lorentz factor vary as a power-law with respect to the jet axis, was proposed by several authors (§6). This kind of outflow is referred to as "structured jet" or "anisotropic jets". The structured jet model has been invoked to explain the extraordinary luminosity of the GRB 0080319B.

1.5 Progenitor models

The long/soft GRBs have been related spectroscopically (e.i. Galama et al. 1998; Hjorth et al. 2003) to the deaths of massive stars, the so-called collapsar model (Woosley 1993). Historically it was with the GRB occurred on April 25, 1998 that the first observational evidence of the connection between supernovae (SNe) and GRBs came out. Galama et al. (1998) indeed reported the discovery of an optical transient, in the BeppoSAX WFC error box of GRB 980425, which occurred within about a day of the γ-ray burst. It was the GRB030329 that provided the first spectroscopic evidence that a very energetic supernova (hypernova) was temporally and spatially coincident with a GRB (Fig. 1.6, Left panel). The timing of the supernova indicated that it exploded within a few days of the GRB (Hjorth et al. 2003). Stanek et al. (2003) reported on the early observations of the afterglow of GRB030329 and the spectroscopic discovery of its associated supernova SN 2003dh. They obtained spectra (wavelength range of 350-850 nm) of the afterglow each night from March 30.12 (0.6 days after the burst) to April 8.13 (UT) (9.6 days after the burst). The spectra taken after 2003 April 5 show broad peaks in flux characteristic of a supernova. Correcting for the afterglow emission,

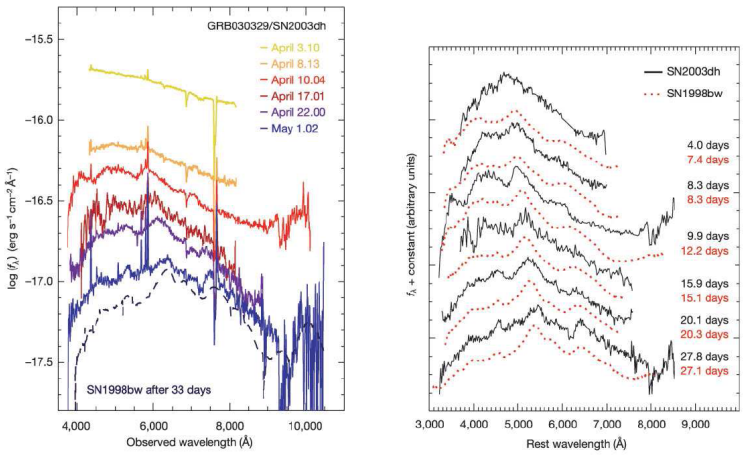

Figure 1.6: (Left panel) spectral evolution of the combined optical flux density of the afterglow of GRB030329, the associated SN 2003dh, and its host galaxy (Stanek et al. 2003). The lower spectra, dominated by SN 2003dh, reveal the supernova signatures. The dashed line represents (for comparison) the spectrum of SN 1998bw after 33 days shifted to the GRB030329 redshift. (Right panel) comparison of the spectral evolution of SN 2003dh and SN 1998bw (Hjorth et al. 2003). The striking similarity between the spectra of these supernovae is clearly seen.

they found that the spectrum of the supernova was remarkably similar to the type Ic hypernova SN 1998bw (Fig. 1.6 Right panel). This strongly suggested that core collapse events can give rise to GRBs, thereby favouring the collapsar model.

Recent observations show that some long duration GRBs are different. No SN emission accompanied the long duration GRBs 060505 and 060614 (Della Valle et al., 2006) down to limits fainter than any known Type Ic SN and hundreds of times fainter than the archetypal SN1998bw that accompanied GRB980425. Multi-band observations of the early afterglows, as well as spectroscopy of the host galaxies, exclude the possibility of significant dust obscuration. Furthermore, the bursts originated in star-forming galaxies, and in the case of GRB 060505 the burst was localized to a compact star-forming knot in a spiral arm of its host galaxy. The properties of the host galaxies, the long duration of the bursts and, in the case of GRB 060505 the location of the burst within its host, all imply a massive stellar origin. The absence of a SN to such deep limits therefore suggests a new phenomenological type of massive stellar death. On the other hand the most favored model for short/hard GRBs is the merger of two compact objects, i.e. two neutron stars or a neutron star and a black hole (Piran 2005 and reference therein). Due of their brevity only recently, only recently it is able to identify well-localized

afterglows in X , in optical and in radio bands. Thus allowing for the first time an association between some short/hard GRBs and galaxies at moderate redshift that show no evidence of recent star-formation. Thus, at least some short/hard GRBs must stem from a different progenitor class than long/soft GRBs, and several lines of evidence favor the compact object merger models. Superflares of Soft Gamma-Repeaters (SGRs) have also been suggested as a source for part of the short GRB population. For recent reviews on short/hard GRBs, see Nakar (2007) and reference therein.

1.6 Theoretical model

1.6.1 Fireball model

Cavallo & Rees (1978) were the first to study the behaviour of an ultra-relativistically expanding source, produced by releasing a very large photon energy ($\sim 10^{51}$ erg) in a very small volume of radius (10–1000 km). The expanding *ball* naturally forms a shell due to the relativistic motion. If the inner engine is active for some time, several shells with different Lorentz factors can be produced. It is believed that collisions between these shells, the so-called internal shocks, power the gamma-ray burst itself. The shells will merge into one flow and later on sweep up matter in the interstellar medium. When the rest-mass energy of this matter will balance the initial energy of the fireball, the flow will slow down converting its kinetic energy into radiation (the external forward shock). Although it is not clear how they are formed, magnetic fields present in the flow cause the electrons that were picked up to produce synchrotron radiation. The electrons move at different speeds, or Lorentz factors. Assuming that their Lorentz factors (their energies) are distributed as a power-law, the resulting emitted spectrum also is a power-law. As the shell slows down in the course of time (also as a powerlaw), the typical Lorentz factor and the corresponding peak emission frequency (ν_m) do the same, causing the entire spectrum to shift toward lower frequencies. Hence, when an afterglow is observed at a specific frequency, the flux will decrease as a power-law in time. When the external forward shock is formed, a reverse shock is produced, moving back into the ejecta.

The mechanism for the afterglow is thought to be syncrotron radiation, which is confirmed by the often observed broken power-law shape of the broad band

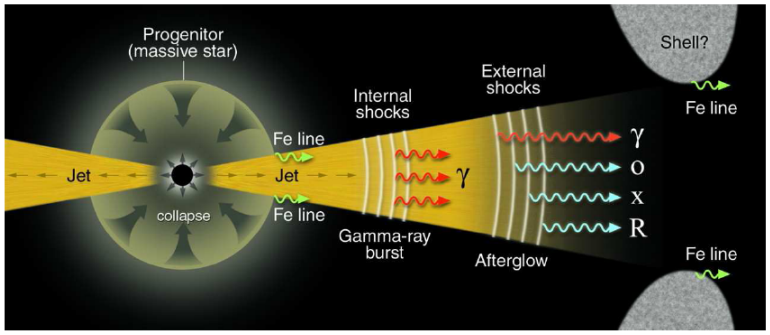

Figure 1.7: Fireball model. The internal shocks, producing a burst of γ-rays and (as it decelerates through interaction with the external medium) an external shock afterglow, which leads successively to X-rays, optical, and radio.

spectrum. Electrons in the fireball are accelerated to ultra-relativistic velocities and produce the observed synchrotron radiation. A schematic representation of the afterglow spectrum, which is generally observed on time scales of hours to weeks after the burst, is shown in Figure 1.8. t_0 represents the time corresponding to the change from radiative expansion to fully adiabatic expansion of the fireball, when $\nu_c = \nu_m$. (a) Fast cooling, which is expected at early times ($t < t_0$). The spectrum consists of four segments, identified as A, B, C, and D. Self-absorption is important below ν_a. The frequencies, ν_m, ν_c and ν_a, decrease with time as indicated; the scalings above the arrows correspond to an adiabatic evolution, and the scalings below, in square brackets, correspond to a fully radiative evolution. (b) Slow cooling, which is expected at late times ($t > t_0$). The evolution is always adiabatic. The four segments are identified as E, F, G, and H.

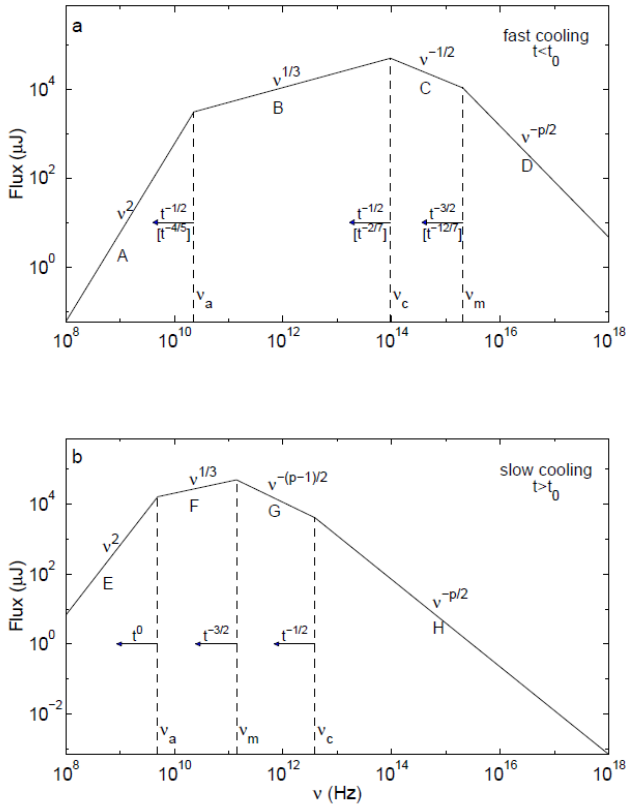

Figure 1.8: Synchrotron spectrum of a relativistic shock with a powerlaw electron distribution (Sari, Piran & Narayan 1998).

Chapter 2

Gamma–ray burst statistical correlations

If you have seen one γ–ray burst....
you have seen one γ–ray burst!

Sarah Yost
Saturday Morning Physics

In the first part of this chapter a short overview of the phenomenological relations of the γ-ray burst emissions is provided. The statistical GRB review is an introduction to our statistical work for focusing the current status of research.

Statistically, the vast quantity of the empirical relationships, that has rapidly progressed in recent years, are divided in 3 sub-groups:

- **Prompt γ-ray emission relationships**
- **Afterglow relationships**
- **Multiwavelength relationships**

In the first sub-group, the relations related to GRB prompt emission parameters are collected. The second sub-group shows the statistical afterglow behaviour and

finally the relations that connect the prompt emission properties with the afterglow properties are discussed in *Multiwavelength empirical relationships* section.

2.1 Prompt Emission Relationships

1.1 *Luminosity-spectral lag relation*

Luminosity-spectral lag relation (Norris relation) suggests that more luminous bursts have shorter spectral lags (τ_{lag}). For long-soft GRBs the detected relation is (Norris, 2000):

$$L_{iso} \propto \tau_{lag}^{1.2} \tag{2.1}$$

It is confirmed in Swift-era by Gehreals et al. (2006), including the peculiar long-soft GRB 060218 (Liang et al., 2006)

Norris established this relationship using the cross correlation lags between low (25-50 KeV) and high (100-300 KeV and $>$ 300 KeV) energy bands for a set of 6 bursts with confirmed redshift observed by `CGRO/BATSE` and `BeppoSax`, although GRB 980425 associated with SN 1998 bw falls below the extrapolated power law. The lag and the isotropic luminosity values for the above-mentioned GRB are 4-5 sec and 1.3×10^{47} erg s^{-1}, respectively. Nowdays the correlation is independently verified by several authors using a large sample of GRBs (e.i. Scheafer, 2007; Dainotti et al., 2009)

Tsutsui et al. (2008) introduces a new redshift-dependent lag-luminosity relation consistent with the original one from Norris (2000). They use 565 BATSE GRBs and their corresponding redshifts are derived from the Yonetoku relation and lag–luminosity relation.

In the new lag-luminosity relation, the power law index is about a factor of 4 smaller than that in the original lag-luminosity relation and it was introduced an additional term $(1 + z)^{\alpha}$ which takes into account the cosmological evolution effect. Statistically the redshift evolution is invoked because Norris lag–luminosity relation is incompatible with the Yonetoku relation; the extrapoleted redshifts in the two relationship are completely different. However, if if one takes into account the effect of the redshift evolution shown in equation, the above mentioned relations are compatible with one another.

$$L_{iso} = 7.5 \times 10^{50}(1+z)^{2.53}\tau_{lag}^{-0.282}, [erg/s] \tag{2.2}$$

The spectral lag estimation also plays a key role in support of the existence of a hypothetical local group population. Vianello et al. (2008) confirm with a high significance level the clustering of faint long duration bursts with long spectral lag around the supergalactic plane.

The association of low luminosity GRBs with the supergalactic plane is not proof that they are associated with clusters of galaxies but indicates that clusters may play a role. A merger involving a white dwarf should produce a long GRB that is likely to be fainter than the formation of a black hole in cosmological GRBs. There will be no supernova in the merger of a white dwarf with a neutron star or black hole, and probably a faint afterglow. In addition, the merger could take place in the intercluster region without a host galaxy if the binary is ripped from its host in the merger interaction involving the cluster galaxies (Foley et al. (2008) and reference therein).

Negative lags, which violate the typical hard-soft evolution of GRBs, have been observed in a small minority of cases (e.g. Chen et al., 2005) (measured spectral lags in time between the low (25-55 keV) and high (110-320 keV) energy channel in BATSE/CGRO experiment) and may be more prevalent in short bursts (Yi et al., 2006).

Short hard bursts also tend to have lower luminosities than classical long GRBs, and therefore are not consistent with the anti-correlation observed between lag and luminosity for long GRBs (Norris, 2002).

Finally Norris (2000) reports anticorrelations between the energy-dependent lag of the long-soft GRB and γ/X peak flux ratio, BATSE spectral hardness ratio and isotropic γ-ray peak luminosity.

1.2 *Relative spectral lag*

Zhang et al. (2006a) put forward a new redshift/luminosity estimator using the relative spectral lag (RSL, $\tau_{rel,31}$), which is defined as the the ratios between the spectral lag between energy bands 1 and 3 of BATSE catalogue and the full width at half-maximum of the pulses ($FWHM$). Based on analyzing the RSL for 9 long BATSE GRBs with known redshift, they found that the RSLs are also tightly correlated with the redshift or luminosity, as follows:

$$logz = a - b\tau_{rel,31} \tag{2.3}$$

$$logL_{iso} = \eta - \xi\tau_{rel,31} \tag{2.4}$$

where $a = 1.56 \pm 0.24, b = 9.66 \pm 1.86, \eta = 55.44 \pm 0.63, \xi = 23.07 \pm 4.88$ and $\tau_{rel,31}$ is normally distributed with a mean value of $\mu = 0.102$ and a standard error of $\sigma = 0.045$. The spearman rank-order correlation coefficients of the two relations are -0.88 ($p \sim 1.5 \times 10^{-3}$) and -0.83 ($p \sim 5 \times 10^{-3}$). It needs to clarify that the redshifts of all sources (with the exception of a grb) are derivated from Yonetoku empirical relation

Peng et al. (2007) from a sample of 82 GRB pulses find that the spectral lags are correlated with the pulse widths, however, there is no correlation between the relative spectral lags and the relative pulse widths.

The physical basis underlying spectral lags is not yet well understood. The observed lag of a burst is a direct consequence of its spectral evolution because the peak of the νF_ν spectrum, E_{peak}, decays with time (Kocevski & Liang, 2003; Hafizi & Mochkovitch, 2007). The internal shock model allows for three possible sources of temporal variations in GRB pulses: cooling and geometric angular effects. Cooling is unable to fully account for the time lag since the synchrotron timescale is much shorter than the lag timescale (Wu & Fenimore, 2000). It has been proposed that the lag-luminosity relation may arise kinematically, based on the viewing angle at which the GRB jet is observed (Salmonson, 2000). In this interpretation, a high-luminosity GRB with short spectral lag corresponds to a jet with a small viewing angle, while a low-luminosity GRB with long spectral lag corresponds to a jet with a large viewing angle (Ioka & Nakamura, 2001). A correlation has also been observed between spectral lag (or luminosity) and jet-break time, thereby connecting the prompt and afterglow phases of GRBs. This may be understood in terms of a model in which the Lorentz factor decreases away from the axis of the GRB jet (Salmonson & Galama, 2002). The connection between spectral lag and the timescales involved in the hydrodynamic processes and radiative mechanisms of the burst has been discussed by Daigne & Mochkovitch (2003).

1.3 *Maximum Spectral lags and redshift correlation*

The maximum spectral lags, τ_{max}, is defined as the largest lag of all the pulses in one burst. By analyzing the BATSE GRBs, Yi, Xie, & Zhang (2008) find a new anti-correlation between τ_{max} and z, excluding GRB 980425. The correlation coefficient is $R = 0.89$ and a change probability is p $= 2.4 \times 10^{-3}$. The best fit power-law model for τ_{max}-z relation

$$log(z) = (-0.28 \pm 0.11) + (-0.44 \pm 0.10) log(\tau_{max}) \tag{2.5}$$

To further they confirm the detected relation, but with slightly different slope, using 10 available HETE–2 GRB data with known redshifts.

It is not clear whether this anti-correlation is present also in Swift GRBs because the γ light curves have not high signal-to-noise ratio for CCF calculation.

1.4 *Quiescent Time and Adjacent Emission correlation*

Quiescent times is defined as the intervals between adjacent episodes of emission during which the γ-ray count rate drops to the background level. Ramirez-Ruiz & Merloni (2001) find a quantitative relation between the duration of an emission episode and the quiescent time elapsed since the previous episode Drago & Pagliara (2008) do not confirm the correlation found by Ramirez-Ruiz & Merloni (2001).

1.5 *Amati and Yonetoku relation*

The correlation between the cosmological rest–frame νF_ν spectrum peak energy, E_{peak}, and the isotropic equivalent radiated energy, E_{iso}, discovered by (Amati et al., 2002) and confirmed/extended by subsequent observations Amati et al. (2006), is one of the most intriguing and debated observational evidences in Gamma–Ray Bursts (GRB) astrophysics. The best fit power–law of the aforementioned correlation obtained by accounting for sample variance is:

$$E_{peak} = 95 \times E_{iso}^{0.49} \tag{2.6}$$

Sub–energetic GRBs (980425 and possibly 031203) and short GRBs are found to be inconsistent with the E_{peak}–E_{iso} correlation.

A related relation discovered by Yonetoku et al. (2004) is:

$$E_{peak} \sim L_{iso}^{0.5} \tag{2.7}$$

where L_{iso} is the isotropic peak luminosity.

Butler et al. (2007) show that pre-Swift correlations found by Amati et al. (2002); Yonetoku et al. (2004); Firmani et al. (2006) (see following section) are likely unrelated to the physical properties of GRBs and are likely useless for tests of cosmology. Also, an explanation of these correlations in terms of a detector threshold provides a natural and quantitative explanation for why short-duration GRBs and events at low redshift tend to be outliers to the correlations This activity has lead to a debate about the usefulness of GRBs as standard candles with both discouraging (Li et al., 2007); (Butler et al., 2007) and encouraging (Amati et al., 2008); (Firmani et al., 2006); (Schaefer, 2007) and (Ghirlanda et al., 2004) results.

1.6 *Firmani relation*

Firmani et al. (2006) proposed a new Gamma Ray Burst luminosity relation that showed a significant improvement over the $L_{iso} - E_{peak}$ relation:

$$L_{iso} = 10^{52.11\pm0.03} \left(\frac{E_{peak}}{10^{2.37} keV}\right)^{1.62\pm0.08} \left(\frac{T_{0.45}}{10^{0.46} s}\right)^{-0.49\pm0.07} \frac{erg}{s}. \tag{2.8}$$

L_{iso} is the isotropic peak luminosity and E_{peak} is the photon energy of the spectral peak for the burst. The new proposed relation simply modifies the E_{peak} value by multiplying it by a power of $T_{0.45}$, where $T_{0.45}$ is a particular measure of the GRB duration. There has been no proposed interpretation of this relation. Collazzi et al. (2008) find that the addition of a duration does not add any significant improvement to the $L_{iso} - E_{peak}$ relation. They also present a simple and direct derivation of the Firmani relation from *both* the $L_{iso} - E_{peak}$ and Amati relations. In brief, they conclude that the Firmani relation neither

has an independent existence nor does it provide any significant improvement on previously known relations that are simpler.

1.7 *Luminosity-variability relation*

A possible Cepheid-like luminosity estimator for the long gamma-ray bursts based on the variability of their light curves.

This relation suggests that more luminous burst tend to have more variable V light curve (Reichartet al., 2001):

$$L \sim V^{3.3^{+1.1}_{-0.9}} \tag{2.9}$$

More recently, Guidorzi et al. (2006) applied the D'Agostini (2005) method, (accounting for the sample variance of the data sets) obtain shallower slopes than those by Reichartet al. (2001) and larger scatters. In particular, for the sample of 32 GRBs with firm redshift they obtained $m = 1.7 \pm 0.4$, $\sigma_{\log V_{\rm R}} \sim 0.34$.

Rizzuto al. (2007) test the variability/peak luminosity (V/L) correlation with a homogeneous sample of 36 GRBs detected with `Swift/BAT` in the 15–350 keV energy band with firm redshift determination.

The correlation is confirmed, as long as the 6 GRBs with low luminosity ($< 5 \times 10^{50}$ erg s^{-1} in the rest-frame 100-1000 keV energy band) are ignored. They confirm that the considerable scatter of the correlation is not due to the combination of data from different instruments with different energy bands, but it is intrinsic to the correlation itself. Thanks to the unprecedented sensitivity of Swift/BAT instrument, the variability/peak luminosity correlation tested on low–luminosity γ-ray burst population highlights that these GRBs are definite outliers.

1.8 N_{peak}–*luminosity relation*

This correlation suggests that the number of peaks is a fast way to spot some high luminosity GRBs:

$$\log L \geq 50.32 + 2\log[N_{peak}] \quad \text{for } N_{peak} \geq 2. \tag{2.10}$$

For $N_{peak} = 1$, there is no lower limit on the luminosity. For example, if Swift sees a faint burst with many peaks, then the burst must be at high redshift (Schaefer, 2007). The number of peaks in a light curve depends on how many collisions between packets of material in the jet occur during the duration of the burst. This number will be determined by many factors, including the exact realization of turbulence in the source and the distribution of velocities and densities in the jet. However, some of the individual peaks might occur sufficiently close in time that these peaks will appear as one. If the individual pulse durations are somewhat longer than the separation in time, then the two pulses will not be distinguishable as being separate. The pulse durations (D_{pulse}) scale as the rise times (Nemiroff, 2000).

For high luminosity bursts all collisions will result in distinct pulses in the light curve, while low luminosity events will have many of the collisions resulting in overlapping broad pulses. Thus, a burst with many peaks can only be a high luminosity event because this is the only way to get narrow peaks that avoid merging together. A burst with one or a few peaks could either be high luminosity (with few shell collisions) or low luminosity (with all the collisions producing merged peaks). This analysis was a theoretical prediction that was tested and shown by Schaefer (2003).

1.9 τ_{RT}–*luminosity relation*

The minimum rise time τ_{RT} in the GRB light curve is taken to be the shortest time over which the light curve rises by half the peak flux of the pulse (Schaefer, 2003):

$$\log L = 52.54 - 1.21\log[\tau_{RT}(1+z)^{-1}/0.1s]. \tag{2.11}$$

For bright bursts, it is an easy calculation to search time intervals before each peak for the shortest one in which the rise is half the peak brightness. In cases where the rise from one time bin to the next is greater than half-peak, the

rise time is determinated as the appropriate fraction of the bin width. The rise times will depend on the exact choice of the first bin. To calculate the exact rise times for faint bursts where the normal background noise provides large Poisson fluctuations, Schaefer (2007) suggest to adopted the average of the derived rise times over all possible start bins as being the minimum rise time. The uncertainty in the minimum rise time is then the rms of the values for all the start bins.

1.10 *Correlations Between Lag, Luminosity, and Duration in Gamma-ray Burst Pulses*

Hakkila et al. (2008) found that each pulse appears to be characterized by its own lag; lag is a consequence of pulse evolution rather than a burst property. Burst peak luminosity and the CCF lag are not fundamental properties, but result from pulse combinations.

The best-fit functional form of *pulse width vs. pulse peak luminosity* relation in the rest frame of the source is:

$$\log(L_{51}) = E + F\log(w_0) \tag{2.12}$$

with $E = 1.53 \pm 0.02$ and $F = -0.85 \pm 0.02$ (E in units of 10^{51} ergs s^{-1})

Again, the exception to the rule is under luminous GRB 980425.

For GRBs with multiple fitted pulses, they also find that pulse spectral hardness is anti-correlates with pulse lag and duration, and correlates with pulse intensity. The same correlations are found in GRB 950325a, and imply that spectral evolution is present both across pulses and within them.

Pulse lag, pulse luminosity, and pulse duration strongly correlate, could imply that most GRB pulses have similar physical mechanisms; these are more consistent with internal than external shocks. Short pulses presumably indicate a collision of material at larger relative Lorentz factor than long pulses, and a large Lorentz factor requires a cleaner fireball with less baryonic matter. The fireball opacity dictates the emission timescale, so a clean, high amplitude fireball should have a short decay and a short lag, while a dirty, low-amplitude fireball should produce a long decay and a long lag.

1.11 *Fractal dimension cluster*

Arkhangelskaja (2002) presents a work on GRB time profile fractal analysis using BATSE catalog. The fractal index is a time profile characteristic which is sensitive to change of shape, if there are two bursts with the same form of time profile but different duration, the fractal indexes of these bursts will be the same. She find that there are four subgroups in fractal dimension distribution for short GRB (D = 1.05 ± 0.03, D = 1.31 ± 0.05, D = 1.51 ± 0.04, D = 1.90 ± 0.03) and six subgroups for intermediate one (D = 1.05 ± 0.09, D = 1.24 ± 0.08, D = 1.44 ± 0.07, D = 1.51 ± 0.08, D = 1.64 ± 0.07, D = 1.91 ± 0.1)

1.12 *The power-complexity relation*

Omodei, Bellazzini & Montangero (2004) have applied the Diffusion Entropy (DE) analysis to study and statistically characterize Gamma-Ray Burst light curves. This method allows the study of correlated non-stationary time series and allows the discrimination between signal and uncorrelated noise. DE provides a quantitative measure of the complexity by means of a scaling index δ. They found that the mean values of δ for the whole BATSE catalog in the four energy bands are 0.80, 0.82, 0.79, and 0.62 respectively. The case of completely correlated noise, also known as ballistic motion for which the walker always jumps in the same direction with a constant jump length, is the upper bound for the value δ =1. The distribution of the values in the first three channels indicates that the diffusive process is close to the ballistic case. This means that, in general, GRB signals are highly correlated signals. They find a logarithmic dependence of the complexity of the data with respect to the fluence of the GRB: the higher the measured power, the greater the complexity of the GRB system.

$$\delta(F) = A + Blog(F) \tag{2.13}$$

with A = 1.2 and B = 0.07. The fluence is a measure of the energy conversion efficiency in the GRB source, so the relationship between δ and the fluence can be interpreted as the increase of the complexity of the energy conversion process.

1.13 *The Peak Energy-Duration Correlation*

Chang (2006) had investigate the correlation between the peak energy and the burst duration using available long GRB data with known redshift, whose

circumburst medium type has been suggested via afterglow light curve modeling. They find that the peak energy and the burst duration of the observed GRBs are correlated both in the observer frame and in the GRB rest frame. The Spearman rank-order correlation values ~ 0.75 and ~ 0.65 with the chance probabilities P=1.0 times 10^{-3} and P=6.0 times 10^{-3} in the observer frame and in the GRB rest frame, respectively.

1.14 *Power-law index of Power Density Spectra correlation and redshift correlation*

Chang, Yoon & Choi (2002) speculate on the possibility of using the Fourier transform analysis method as a distance estimator of the observed γ-ray bursts. It is based on a hypothetical empirical relation between the redshift and the power-law index of power density spectra (PDSs) of the observed GRBs. This relation is constructed by using the fact that the observed power-law index is dependent upon a characteristic timescale of GRB light curves. The rms error of redshift estimates is 0.42 for an empirical relation obtained with the 7 long ($T_{90} > 15$) GRBs observed by the BATSE whose redshift information is available. The estimator is not yet robust, and they conclude that redshift estimates are subject to the stochastic nature of the observed PDSs and accuracy of estimates are limited by unknown properties of the GRBs.

1.15 *Successive time intervals, Successive pulse amplitudes, Pulse amplitudes and Adjacent time intervals correlations*

McBreen et al. (2004) have analized the temporal properties of a large sample of bright gamma-ray bursts (GRBs) with durations between 0.05 s and 674 s. The large range in duration (T_{90}) is accompanied by a similarly large range in the median values of the pulse timing properties including rise time, fall time, FWHM and separation between the pulse. Four times diagrams relating these pulse properties to T_{90} are presented and show the power law relationships between the median values of the four pulse timing properties and T_{90}, but also that the power laws depend in a consistent manner on the number of pulses per GRB. The timing diagrams are caused by the correlated properties of the pulses in the burst and can be explained by a combination of factors including the Doppler boos factor

G, a jet and emission from below the photosphere. GRBs with similar values of T_{90} have a wide range in the number of pulses. The pulses in GRBs have seven distinctive statistical properties including correlations between successive time intervals, correlations between successive pulse amplitudes, an anticorrelation between pulse amplitudes and adjacent time intervals. The timing diagrams and correlated pulses suggest that GRBs are powered by accretion processes signaling jets from the formation of black holes.

1.16 *Peak of the Power Density and redshift*

Yang et al. (2005) presents a possible luminosity estimator for the long gamma-ray bursts based on the γ-light curves. They use the methods of temporal variability analysis in time domain to calculate the power density spectrum (PDS) of the 12 gamma-ray bursts (GRBs) with known redshifts observed by CGRO/BATSE. The peak of the power density P measures the variability intensity of each light curve and a strong correlation is found between P and the isotropic peak luminosity. It's a new relationship between the temporal quantities and the luminosities of long GRBs, succeeding the lag-luminosity relation suggested by Norris et al.(2000) and variability-luminosity relation shown by Reichart et al. (2001).

2.2 Afterglow empirical relationships

2.1 *shallow decay phase of GRB X-ray afterglows and redshift*

Stratta et al. (2008) selected and analyzed all the *Swift*/XRT afterglows at known redshift observed between March 2005 and June 2008 featuring a shallow decay phase in their X-ray lightcurves. For 21 GRBs they find an anticorrelation of the logarithm of the duration of the shallow phase with redshift, with a Spearman rank-order correlation coefficient of $r = -0.4$ and a null hypothesis probability of 5%. When we correct the durations for cosmological dilation, the anticorrelation strenghtens, with $r = -0.6$ and a null hypothesis probability of 0.4%. Finally they found an anticorrelation between the energy of the burst and the shallow phase duration, with $r = -0.80$ and a null hypothesis probability of 1.8%, using only GRBs that have a well-measured burst peak energy (8 out of

21).

2.2 *Luminosity Time correlation*

Dainotti, Cardone, & Capozziello, (2008) look for statistical correlation using data on the X- ray decay curve and spectral index of GRBs observed with the Swift/XRT satellite. They found a correlation between the X - ray luminosity $L_X(T_a)$ and the time constant T_a of the afterglow light curve. The linear relation between $\log[L_X(T_a)]$ and $\log[T_a/(1+z)]$ presents an intrinsic scatter $\sigma_{int} = 0.33$ comparable to previously reported relations. The authors suggest that the high Spearman correlation coefficient, the low value of the fit residuals and the modest intrinsic scatter renders the $L_X(T_a)$ - T_a relation a new valid tool to standardize GRBs.

2.3 *Peak flux-Peak epoch* & *post-peak relation*

Panaitescu & Vestrand (2008), studing the temporal behaviour of the early optical emission from γ–Ray Burst afterglows, show that is realible to divided them in four classes: fast-rising with an early peak, slow-rising with a late peak, flat plateaus, and rapid decays since first measurement. The fast-rising optical afterglows display correlations among peak flux, peak epoch, and post-peak power-law decay index. the peak flux-peak epoch relation exhibited by the fast and slow-rising optical light-curves could provide a way to use this type of afterglows as standard candles.

2.4 *Afterglow Luminosity cluster*

Hints of standardization of the X-ray afterglow luminosities were first discovered by Boër & Gendre (2000), who found evidences for clustering in the X-ray luminosity of BeppoSAX afterglows, and confirmed later by Gendre & Boër (2005). This study was completed by Nardini et al. (2006) and Liang & Zhang (2006b) who found independently that optical afterglows were also clustered in luminosity, and by Gendre et al. (2008) who extended this study towards infrared wavelengths.

2.5 ***Correlation between the duration and the X-ray luminosity of the shallow decay phase***

Sato et al. (2007) have investigated the characteristics of the shallow decay phase in the early X–ray afterglows of GRBs observed by Swift X-Ray Telescope (XRT) during the period of January 2005 to December 2006. They find that the intrinsic break time at the shallow-to-normal decay transition in the X-ray light curve T^0_{brk} is moderately well correlated with the isotropic X-ray luminosity in the end of the shallow decay phase ($L_{X,end}$) as

$$T^0_{brk} = (9.39 \pm 0.64) \times 10^3 s (L_{X,end}/10^{47} ergs/s)^{(-0.71+/-0.03)} \tag{2.14}$$

while T^0_{brk} is weakly correlated with the isotropic γ-ray energy of the prompt emission $E_{\gamma,iso}$

2.6 ***Apparent magnitude and the Rate of Decay correlation***

Oates et al. (2008) present the first statistical analysis of 27 UVOT optical/ultra-violet lightcurves of GRB afterglows. They have found, through analysis of the lightcurves in the observer's frame, that a significant fraction rise in the first 500s after the GRB trigger, that all light–curves decay after 500s, typically as a power-law with a relatively narrow distribution of decay indices, and that the brightest optical afterglows tend to decay the quickest. They find that at 99.8 % confidence, there is a correlation, in the observed frame, between the apparent magnitude of the light–curves at 400s and the rate of decay after 500s. However, in the rest frame a Spearman Rank test shows only a weak correlation of low statistical significance between luminosity and decay rate.

2.3 Multiwavelength empirical relationships

3.1*Frail and Ghirlanda correlation*

Frail et al. (2001) and Bloom et al. (2003) found that the beaming-corrected gamma-ray energy is essentially constant;

$$E_{\gamma,iso}\theta_j^2 = E_j \sim const. \tag{2.15}$$

Ghirlanda et al. (2004) found that the beaming-corrected gamma-ray energy is not constant, but is related to the rest-frame spectral peak energy:

$$E_p \propto E_{\gamma,iso}^{1/2} t_j^{1/2} \tag{2.16}$$

Notice that the Ghirlanda relation and the Frail relation are incompatible with each other.

3.2 *Liang-Zhang relation*

Liang & Zhang (2005) had proposed an empirical relation among three observables, namely E_p, $E_{\gamma,iso}$ and the *optical band break time* t_b. The relation gives $E_p \propto E_{\gamma,iso}^{0.52} t_b^{0.64}$. The Liang-Zhang relation is the the Ghirlanda and Amati relations projected onto a plane.

3.3 *Willingale correlation*

Willingale et al. (2006) performed a systematic study of the shallow to normal decay transition breaks in the early X-ray afterglows of a sample of Swift GRBs. They found a new sequence of correlation which is parallel to the Ghirlanda relation. This is effectively a new series of $E_p - E_{\gamma,\mathrm{iso}} - t_b$ relation but by replacing the optical breaks by X-ray breaks. The fact that the two correlations form a parallel sequence is intriguing.

3.4 *Prompt Emission and X/Optical Flux correlation*

Nysewander, Fruchter & Peér (2008) present a comparative study of the observed properties of the optical and X-ray afterglows of short- and long-duration γ-ray bursts. Using a large sample of 37 short GRBs and 421 long GRBs, they find a strong correlation between afterglow brightness measured after 11 hours and the energy release in the prompt emission, measured in both the optical (R band) and X-ray flux and $E_{\gamma,\mathrm{iso}}$:

$$F_{R,X} \propto {E_{\gamma,\mathrm{iso}}}^{\alpha} \tag{2.17}$$

with $\alpha \simeq 1$ in both cases.

Furthermore, the constant of proportionality is nearly identical for long and short bursts. A similar correlation between the optical afterglow and the γ-ray fluence is also reported by Kann et al. (2008).

3.5 *Optical, X-ray and γ-ray emissions correlation*

Gehrels et al. (2008) analyze short and long bursts. It is found for both classes that the optical, X-ray and γ-ray emissions are linearly correlated, but with a large spread about the correlation line; stronger bursts tend to have brighter afterglows, and bursts with brighter X-ray afterglow tend to have brighter optical afterglow. Short bursts are, on average, weaker in both prompt and afterglow emissions. No short bursts are seen with extremely low optical to X-ray ratio as occurs for "dark" long bursts. Although statistics are still poor for short bursts, there is no evidence yet for a subgroup of short bursts with high extinction as there is for long bursts. Long bursts are detected in the dark category at the same fraction as for pre-Swift bursts. Interesting cases are discovered of long bursts that are detected in the optical, and yet have low enough optical to X-ray ratio to be classified as dark. For the prompt emission, short and long bursts have different average tracks on flux vs fluence plots. In Swift, GRB detections tend to be fluence limited for short bursts and flux limited for long events.

3.6 *Peak Spectral Energy and Peak Bolometric Luminosity of SNe correlation*

Based on the four pairs of GRBs and SNe with spectroscopically confirmed connection Li (2006) find a tight correlation between the peak spectral energy of GRBs and the peak bolometric luminosity of the underlying SNe. The recent discovery of X-ray flash 080109 associated with a normal core-collapse SN 2008D confirmed this relation and extended the GRB-SN connection.

3.7 *Extrapoleted X-ray flux, prompt-$\gamma - ray$ fluence and Extrapoleted v-band magnitude* The Swift Ultra-Violet/Optical Telescope has observed 200 gamma-ray bursts (GRBs) in its first two-and-a-half years of operation. From this collection of observations Roming et al. (2009) have obtained 40 well sampled light curves. Using this dataset they present general optical/UV properties of GRBs, including filter dependent temporal slopes and color–color relationships. Finally they also show that correlations exist between both the 11 hour X–ray flux (0.3-10 keV) and the promot γ-ray fluence (15-150 keV) and $V - band$ magnitude

at $\sim$ 2000 s.

3.8 *Pulse lag, peak luminosity and the jet-break time correlations*

Salmonson & Galama (2002) show a correlation between the pulse lag and the jet-break time for seven BATSE gamma-ray bursts with known redshifts. As pulse lag and luminosity have been found to be correlated, this also represents a correlation between peak luminosity and jet-break time. Observed timescales (variability or spectral lags), as well as peak luminosity, naturally have a strong dependence on the Lorentz factor of the outflow, so we propose that much of the variety among GRBs has a purely kinematic origin (the speed or direction of the outflow). They explore a model in which the variation among GRBs is due to a variation in jet opening angles and find that the narrowest jets have the fastest outflows. They also explore models in which the jets have similar morphology and size, and the variation among bursts is caused by variations in viewing angles and/or due to velocity profiles. The relations between luminosity, variability, spectral lag, and jet-break time can be qualitatively understood from models in which the Lorentz factor decreases as a function of angle from the jet axis. One expects to see high luminosities, short pulse lags, and high variability as well as an early jet–break time for bursts viewed on-axis, while higher viewing inclinations will yield lower luminosities, longer pulse lags, smoother bursts, and later jet-break times.

Chapter 3

Prompt Emission: Nonlinear Analysis

A cloud is made of billows upon billows upon billows that look like clouds. As you come closer to a cloud you don't get something smooth, but irregularities at a smaller scale.

B. Mandelbrot

In this chapter the study of morphological features of the prompt γ–ray emission is presented in detailed manner. It is introduced a new suitable statistical tool, *Hurst exponent*, to characterize the complex and random structures that these emissions manifest during their short and erratic duration. It is shown that the observational properties of the prompt γ–ray emission do not seem to follow any cosmological evolution trend and they are the manifestation of same physical phenomenon that is self–affinity at every scale and at any epoch of the universe.

3.1 Time series analysis of SWIFT/BAT data

The time properties of BAT γ-ray burst emission are elaborated in a detailed manner through nonlinear time series analysis methods. We focus primarily on the properties of the type soft-long GRBs. The timescale of intensity variations in γ-ray bursts phenomenon is an important observational parameter because this timescale can be used to place an upper limit on the size of the γ-ray emitting region and more generally for understanding the nature of the process responsible for the GRB light curves. The temporal profiles of GRBs are often very variable and each time profile looks very different. Fishman & Meegan (1995) made an attempt to roughly classify them in four classes (§1.2.2). High energy emission of GRBs exhibit a vast range of complex temporal behaviors, so any morphological classification scheme seem to appear not be comprehensive and systematic. However, their main properties could appear simpler using suitable statistical analysis. In fact, any linear, nonlinear or chaotic dynamical phenomena can be described and quantified, so that it can be distinguished from each other and some conclusions about the possible underlying mechanism may be obtained. A dynamical system is linear if the response characteristics are additive (superposition) and homogeneous (scaling). The term additive means that the output to a sum of inputs is equal to the sum of the outputs produced by each input individually. The term homogeneous means that the output to a sum of inputs is equal to the sum of the outputs produced by the input alone. Furthermore a nonlinear system is one whose behavior is not simply the sum of its parts or their multiples and as such it is often difficult (or impossible) to model it. Moreover its evolution with respect to a given variable e.g. time, is sometimes difficult to predict or even impossible after a given time duration. Typical nonlinear systems are the Navier-Stokes equations. A really interesting category of nonlinear systems are the chaotic systems. Chaotic systems have the unique ability to appear, through their realization, as random systems but in fact they comprise a special category of nonlinear systems characterized by a small number of independent variables.

Unfortunately GRBs are transient phenomena so that each GRB brings insufficient information to make a conclusive analysis. A more powerful quantitative analysis can be done using samples of many bursts studying the statistical behavior of these objects (Stern, 1999).

In the following section we propose to analyze the underlying structure of

prompt emission of GRBs using the Hurst exponent. This statistical tool is able to characterize the same statistical behavior without having neither the same time duration nor fixed occurrence time, making the time series comparable with each other.

Initially we try to evaluate a method of research in order to provide a correct estimation of Hurst exponent in SWIFT/BAT light curves. We decided to use an homogeneous sample of bright light curves provided by BAT instrument to avoid inconsistent estimates due to the effect of the internal variability in different energy satellite channels.

After we calculate the Hurst exponents for the GRB with known redshift. It is found that the value of the Hurst exponents for all analized light curves is more than 0.5 and futhermore it is not correlated with the redshift.

The results suggest that the prompt emission can be due to realizations of the same physical process which is self-affinity at any time-scale and the lack correlation with the redshift suggest that the underlying process producing the observed prompt emission do not follow a cosmological evolution trend.

3.1.1 Data Reduction and Sample

The BAT is a highly sensitive, large field of view (FOV) (1.4 sr for >50% coded FOV and 2.2 sr for >10% coded FOV), coded-aperture telescope, which detects and localizes GRBs in real time. The fast and accurate BAT GRB positions with 1-3 arc-minute error radii are the key to autonomously slewing the spacecraft to point the XRT and the UVOT. The BAT GRB position, light curves, and the detector plane image (BAT scaled map) are transmitted through TDRSS to the ground within 20–200 s after the burst trigger. The BAT detector plane is composed of 32,768 pieces of CdZnTe (CZT: $4 \times 4 \times 2$ mm), and the coded-aperture mask is composed of $\sim$ 52,000 lead tiles ($5 \times 5 \times 1$ mm) with a 1-m separation between mask and detector plane. The energy range is 15-150 keV for imaging or mask weighting[1] with a non-coded response up to 350 keV.

Immediately after the first attempt to fit the Crab spectrum with the pre-launch detector energy response matrices (DRM), BAT team noticed that there were systematic errors in the pre-launch DRM at low energies (below 25 keV)

[1]Mask weighting is a background subtraction technique based on the modulation resulting from the coded mask.

and also at high energies (above 80 keV). To overcome these problems, the BAT team has released the software tool, `batphasyserr`, and the CALDB file (swbsyserr20030101v002.fits) to apply the energy dependent systematic errors to the PHA file.

Rizzuto et al. (2007) suggest that the BAT light curves of most GRBs with raw counts, not masked, are not suitable for temporal variability studies. Therefore the BAT event files were retrieved from the *Swift* public archive [2] and analyze through the standard BAT analysis software distributed within FTOOLS v6.1. For each GRB we extract mask-tagged light curves for a number of different binning times in the total nominal energy band (15–350 keV) [3], through the tool *batmaskwtevt* adopting the ground-refined coordinates provided by the BAT team for each burst. These curves are therefore already background subtracted according to the coded mask technique (Barthelmy et al. 2005). We also applied the energy calibration to the event file making use of the closest-in-time gain/offset file through the tool *bateconvert*, as suggested by the BAT team[4]. Finally these light curves are expressed as count rates with uncertainties: the rates are background-subtracted counts per second per fully illuminated detector for an equivalent on-axis source, as the default corrections are applied: *ndets, pcode, maskwt, flatfield*.

Rizzuto et al. (2007) also studied the behaviour of the background fluctuations and they found that the mask-tagged rates, r_i, fluctuate compatibly with a white noise with sigma σ_{r_i} (r_i and σ_{r_i} are the rate and its uncertainty of the i-th bin, respectively). An upper limit of $\sim$ 2–4% (4–6%) at 90% (99%) confidence level can be derived on the presence of a possible extra variance (of instrumental origin, for instance) in addition to that due to the Poisson counting statistics, implicitly assumed during the light curve extraction with the tool *batbinevt*. Similar correction are applied in our data analysis.

The sample includes 109 GRBs with confirmed redshift detected by *Swift*/BAT between the launch (2004, November 20) and December 2008. Their redshift distribution are plotted in fig. 3.1.

[2] http://swift.gsfc.nasa.gov/docs/swift/archive/

[3] The effective band is 15–150 keV, because photons with energy above 150 keV become transparent to the coded mask and are treated as background by the mask-weighting technique (e.g., Sakamoto et al. 2006).

[4] http://swift.gsfc.nasa.gov/docs/swift/analysis/threads.

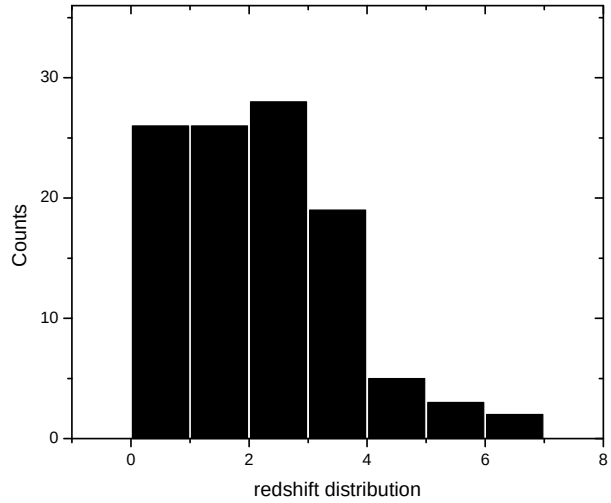

Figure 3.1: Redshift distribution BAT/SWIFT sample.

3.2 Hurst exponent: statistical methodology for non-periodic cycles

The first analysis method usually applied in a time series data set coming from a given source is the Power Spectral Density (PSD). The application of this method indirectly implies the existence of patterns in the data set that can be broke down into a sum of sinusoids with different frequencies and amplitudes. Unfortunately the underlying radiation mechanism of a GRB producing the observed γ-ray flux is not structured on the basis of periodic cycles. This can be readily seen from the form of their PSD exhibiting no significant peaks (Beloborodov Stern & Svensson, 2000; see fig.3.2.).

In the case that a multicomponent physical system, such the one of an GRB or AGN, does not exhibit any periodic cycles at all within its realizations, possible nonperiodic cycles might still be present. These nonperiodic patterns usually demonstrate the same statistical behavior without having neither the same time duration nor fixed occurrence times in comparison to the classical periodic systems. The existence of cycle can be studied through the estimation of the Hurst exponent H.

It is worth noticing that very different processes (e.g. hydrodynamical turbu-

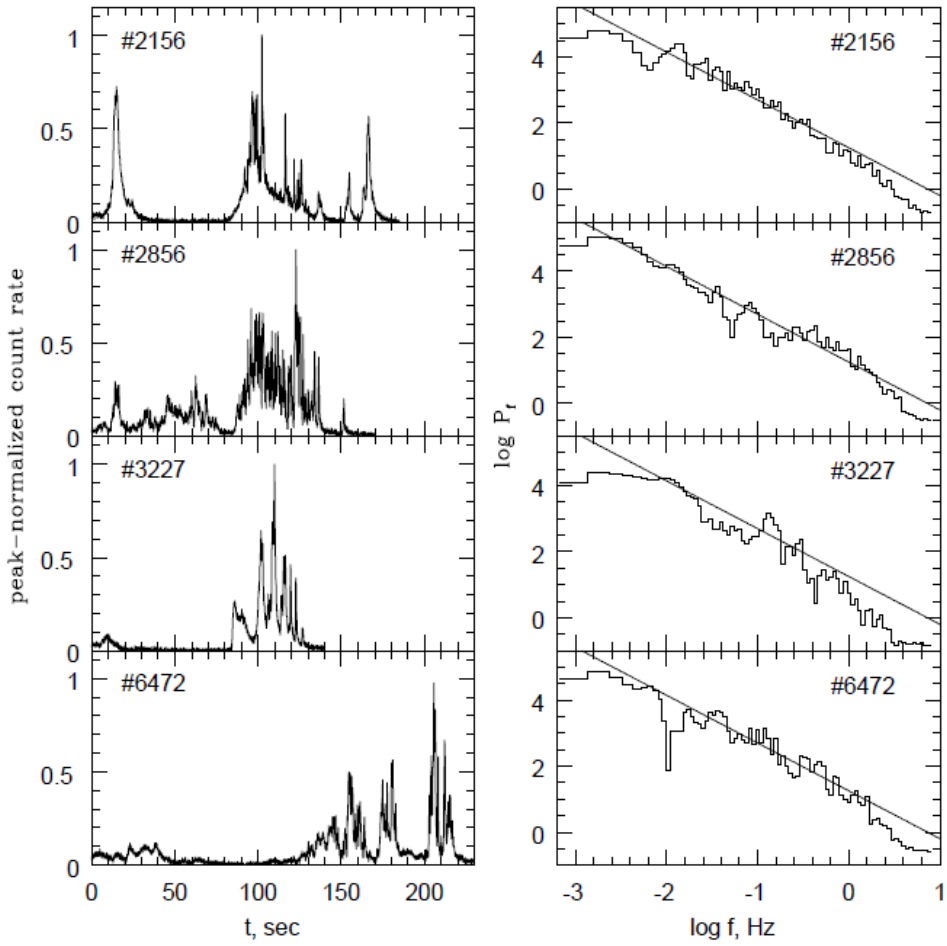

Figure 3.2: BATSE light curves and their PDSs for the four brightest bursts, from Beloborodov Stern & Svensson (2000). The underlying radiation mechanism of a GRB producing the observed γ-ray flux is not structured on the basis of periodic cycles. This can be readily seen from the form of their PSDs exhibiting no significant peaks

lence, standard and anomalous diffusion) are able to produce signals characterized by scaling laws that can be discriminated on the basis of their Hurst exponent.

3.3 Hurst exponent, Fractal Dimension and Power Spectrum and Autocorrelation Function

Hurst (1951) [5] developed his own analytical method to explain the non-periodic cycles. To identify a non-random process, he had used the Einstein's work on Brownian motion. Brownian motion is a widely accepted model for a random walk. In a random walk there is no correlation between any element and future element. Einstein studied the properties of the Brownian motion found that the distance R covered by a particle undergoing random collisions is directly proportional to the square-root of time T:

$$R = k \times T^{0.5} \tag{3.1}$$

where k is a constant which depends on the time-series. Hurst generalized the equation valid for the Brownian motion in order to include a broader class of time series. The generalization proposed by Hurst was:

$$R/S = k \times T^{H} \tag{3.2}$$

- H=0.5, the behaviour of the time-series is similar to a random walk;
- H<0.5, the time-series covers *less distance* than a random walk;
- H>0.5, the time-series covers *more distance* than a random walk.

where S is the standard deviation of the time series. For the reasons mentioned previously the Hurst exponent gives an estimate of the average non-periodic cycle length, with $0 < H < 0.50$, they are more volatile than a random walk.

The Hurst exponent is also directly related to the fractal dimension, which gives a measure of the roughness of a surface. The relationship between the fractal

[5] H was originally developed in hydrology for the practical matter of determining optimum dam sizing for the Nile river's volatile rain

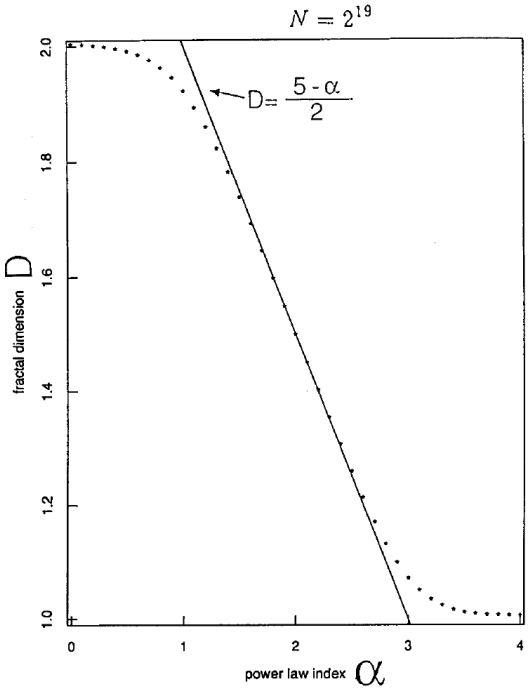

Figure 3.3: The calculated fractal dimension as a function of the power law index from Higuchi 1990

dimension D and the Hurst exponent H is (Feder, 1988)

$$D = 2 - H \tag{3.3}$$

It is now accepted that when the power spectrum of an irregular time series is expressed by a single power law $f^{-\alpha}$, the time series shows a property of a fractal curve. As the fractal length $L(k)$ of the time series is expressed as $L(k) \propto k^{-D}$ where k is the time interval, the fractal dimension D is expected to be closely related to the power law index α (see fig. 3.3). The relation between α and D has been investigated by Higuchi (1990) using numerical simulation and it is given by

$$D = \frac{5 - \alpha}{2} \tag{3.4}$$

The decay of the autocorrelation function for γ-ray light curve is a power law:

$$p(k) = C \times K^{-\varrho} \tag{3.5}$$

In Equation 3.5, C is a constant and $p(k)$ is the autocorrelation function with

lag k. The Hurst exponent is related to the exponent ϱ in the equation by (Feder, 1988):

$$H = 1 - \frac{\varrho}{2} \tag{3.6}$$

3.3.1 Rescaled range analysis

Rescaled range analysis measure characterising the divergence of time series defined as the range of the sum of the deviations of data from the mean divided by the sample standard deviation (Mandelbrot et al, 1972) Both range R and standard deviation S measure the divergence of the time-series, but the first is a measure of dispersion based on a sum of the data, the second is a measure based on the squared data. For some processes (like white Gaussian noise, which has no persistence) the two measures of dispersion are similar and R/S is asymptotically constant with T, duration of the data sample. For other processes R/S is proportional to a power of T.

Roughly speaking the method consists of the following steps. The data set is partitioned into non-overlapping subsets of the same length N_A and then the cumulative deviation D_A is estimated for each one of them. Finally the statistical range R_A and the standard deviation S_A for all the subsets are computed and a mean value of their ratio $(R/S)_{NA}$ is derived. The same exactly procedure is then repeated having another partitioning configuration of different N_A. Then H can be estimated by linear regression as it consists the slope of the straight line passing through the points $((R/S)_{NA}, N_A)$ in a $log - log$ representation

In detail, if we consider a stationary time series data set consisting of N measurements, x_i, measured at discrete times t_i with (i = 1, . . . ,N) separated by Δt time units. Starting from the beginning, the data set is partitioned into A non-overlapping subsets of N_A successive number of points. This procedure is performed for $N_A = 2, \ldots$, N and the last points which can not form a complete subset are simply dropped. The total number of subsets for a given N_A is equal to the greatest integer less than or equal to N/N_A, therefore A = 1, . . . , $[N/N_A]$. At the end there are N -1 groups each one consisting of A subsets of N_A points. The total number of points within each group is A $\times$ N_A and should be the closest possible to N. Initially the arithmetic mean, the standard deviation and the cumulative deviation respectively for every subset (among the A) consisting of N_A

points within a group, is estimated

$$\overline{x_A} = \frac{\sum_{n=1}^{N_A} x_{n,A}}{N_A} \tag{3.7}$$

$$S_A = \sqrt{\frac{\sum_{n=1}^{N_A}(x_{n,A} - \overline{x_A})^2}{N_A - 1}} \tag{3.8}$$

$$D_A = \sum_{n=1}^{k}(x_{n,A} - \overline{x_A}) \tag{3.9}$$

Then, the statistical range of D_A, R_A, is estimated and it is normalized to the S_A. That gives the rescaled range statistic for a given subset of a given group

$$\frac{R_A}{S_A} = \frac{1}{S_A}(max[D_A] - min[D_A] \tag{3.10}$$

Finally the mean value of the rescaled range statistics is computed for all subsets A within the same group and the same exactly computations are performed for all the $N-1$ groups.

$$\left(\frac{R}{S}\right)_{N_A} = \frac{\sum_{A=1}^{[N/N_A]}}{[N/N_A]} \tag{3.11}$$

for N_A= 1,..., N–1 The Hurst exponent H for the initial data set is then computed based on the following relation

$$\left(\frac{R}{S}\right)_n = Cn^H \tag{3.12}$$

and by taking the logarithms of both sides this yields

$$\log\left(\frac{R}{S}\right)_n = logC + H\log n \tag{3.13}$$

The abscissa of this point N_p defines the mean time duration (i.e. $N_p \times \Delta_t$) when the long-term memory of the system starts to dissipate The corresponding group, consisting of subsets each one being $N_p \times \Delta$t time units long, displays the biggest deviations from the mean and therefore it will be the one with the dominant trend. Practically the Hurst exponent H is equal to the slope of the linear regression model fitted to the ensemble of points $(2,(R/S)_2),(3,(R/S)_3),...,(N_p,(R/S)N_p)$.

The classical R/S analysis since it is the original one proposed by Mandelbrot

(1972) for the estimation of the Hurst exponent. In general there is a big variety of methods aiming to a more robust and less biased estimation of H. All methods different from the aforementioned analysis only in the normalization factor of R_A, S_A (eq.3.67). As it was shown from Davies & Harte (1987) the conventional R/S analysis using a Hurst regression can be biased towards accepting a long-term dependence hypothesis even when the true process is first order autoregressive (AR). Moreover another crucial issue is that the measurements of a data set might exhibit short-range dependencies (i.e. autocorrelations) fact that make them depended. Usually small data sets have statistical different properties from their parent distributions in the sense that they might have significant different S_A from their parent distribution (heteroscedasticity) (Levenbach 1973). A final matter is that the various estimates $((R/S)_{NA}, NA)$ might be distributed around non-Gaussian distributions converging very slowly to Gaussian distributions. All these issues give raise to biases concerning the estimations of the coefficients of the linear regression model.

3.3.2 Higushi method

Higuchi (1988)develops a method for calculating the fractal dimension D_H suitable to characterize nonstationary signals.

D_H may be calculated in a time window containing few data points and the window can be moved along the signal. Using moving window one obtains running fractal dimension that shows changes of the signal complexity in time. Higher values of D_H correspond to presence of higher frequencies in the signal Fourier spectrum measuring the complexity and relative changes of the signal. Higushi Method is as follows.

We take a finite set of time series taken at a regular interval:

$$X(1), X(2), X(3), ..., X(N). \tag{3.14}$$

From the given time series, we construct a new time series,

$$X(m), X(m+k), X(m+2k), ..., X(m+[(N-m)/k].k) \tag{3.15}$$

where both k and m (m = 1, 2, 3,...,k) are integers, m and k indicate the initial time and the interval time respectively. Then k sets of new time series are obtained.

We define the length of the curve of the new time series as follows:

$$L_m(k) = \{(\sum_{i=1}^{[(N-m)/k]} |X(m+ik) - X(m+(i-)k|) \frac{N-1}{[(N-m)/k].k} \}/k \qquad (3.16)$$

The length of the curve for the time interval k, $\langle L(k) \rangle$ is defined as the average value over k sets of $L_m(k)$. If $\langle L(k) \rangle \propto k^{-D}$, we judge the curve is fractal with dimension D. We deduce fractal dimension D from the slope of the best fitted line corresponding to the plot of log $\langle L(k) \rangle$ against log k. Fractal dimension and Hurst exponent are related by equation 1.3.

3.4 Evalutation of a reserch method for the estimation of Hurst exponent in BAT light curves

Nowadays a lot of methods for the estimation of Hurst coefficients in time series are available. All methods different from the aforementioned analysis only in the normalization factor of R_A, S_A

For a careful estimation, we use more than one estimate method [6] and draw plot evaluating the quality of the estimation in terms of accuracy.

We considered the following different algorithms for the evaluation of Hurst coefficient:

- method of the Aggregate Variance
- method of the Modulus of the Aggregate series
- Higuchi method
- R/S Method
- Dispersional Analysis (DA)
- Detrended Fluctuation Analysis (DFA)

[6] The theories of the methods can be found in Murad's Taqqu, Vadim Teverovsky and Walter Willinger's paper "Estimators for long-range dependence: an empirical study" or other related papers.

- Periodogram method

- Wavelet method

The *Aggregate Variance* (Taqqu et al., 1996) a time domain method useful for non-stationary time series that obtains the multi-scale analysis with the aggregation of adjacent points and measures the similarity in terms of variance. The *Modulus of the Aggregate* series method (Taqqu et al., 1996) is similar to the previous one but it uses modulus instead of variance. The *Higuchi method* (Higuchi,1988) is a time domain method useful for non-stationary series too, but performs the multi-scale analysis with the creation of subseries, in following iterations, with points taken at different distances each other. In this case the similarity is described beginning from the partial sums of the original time series (derived from sub-series) and finding a normalized length (Higuchi length) of the sub-series. *DA* (Bassingthwaighte & Raymond, 1995) is the differential version of the Aggregate Variance method, useful for stationary series. *DFA* (Peng et al., 1994) is the well-known estimator with detrend, working in the time domain. It is effective both with stationary and non stationary time series. The *Periodogram* (Taqqu et al., 1996) is a frequency domain method, suited for stationary time series, that evaluates the slope of the spectrum (calculated by a Discrete Fourier Trasform) near the zero-frequency axis in a log-log plot. The value of this slope is correlated to the Hurst's coefficient by known relations. The function *waveletFit* computes the Discrete Wavelet Transform, averages the squares of the coefficients of the transform, and then performs a linear regression on the logarithm of the average, versus the log of the scale parameter of the transform. The result should be directly proportional to H providing an estimate for the Hurst exponent.

The reliability of these methods was tested by applying theme to synthetic and observed time series with high signal to noise. We found that for High non-stationary series the best estimates are provided by Higuchi method and Aggregate Variance method. The Detrend Fluctuation Analysis works well for certain types of nonstationary time series especially slowly varying trends and it can not provide values for all analyzed curves in our Swift sample.

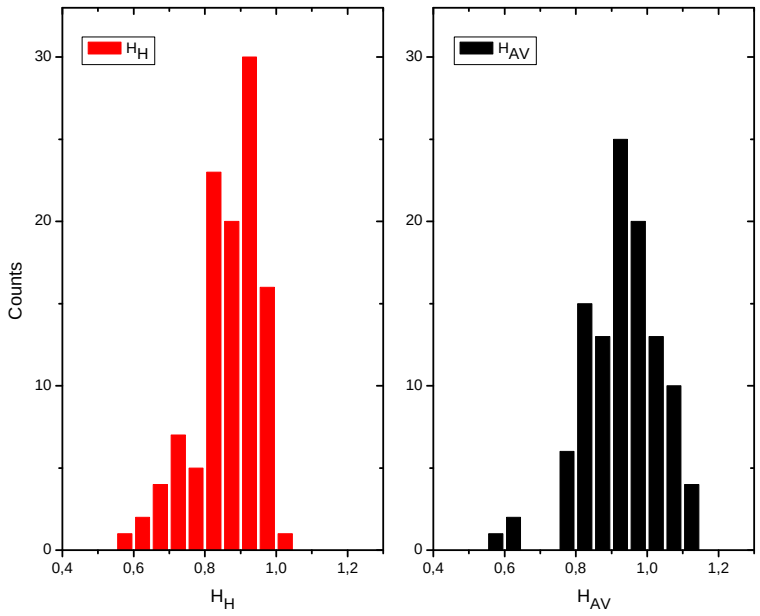

Figure 3.4: Histograms of Hurst exponent distribution. Left panel: Higuchi method. Right panel: Aggragate Variance method.

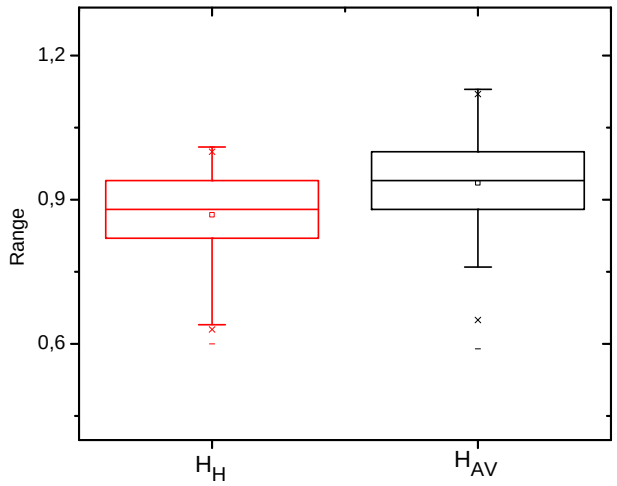

Figure 3.5: Box Charts of Hurst exponent distribution. Left panel: Higuchi method. Right panel: Aggragate Variance method.

3.4.1 Results: far from a random walk

In our analysis we found H ~ 0.8 (see table 3.2). This value is significantly larger than the value of 0.5 that would correspond to variations produced by a white-noise process indicating that the physics that produces the prompt γ emission is a correlated random process. Periodically correlated random processes (PCRP, also known as Cyclostationary or periodically non-stationary) is an adequate model for describing the physical phenomena, where stochasticity and recurrence play significant role. In table 1 we report the Hurst exponent for an homogeneous Swift/BAT light curve with known redshift using the methods mentioned above. Our result is surprising in many respects, as mentioned in the introduction, a narrow clustering of the Hurst exponent centered at $\langle H \rangle \sim 0.9$ with small dispersion $\sigma \sim 0.1$ point out that the physical process is far from white noise with the characteristic property of self-affinity (see table 3.1 and graphs 3.4/3.5). In mathematics, self-affinity refers to a fractal whose pieces are scaled by different amounts in the x– and y–directions. This means that in order to appreciate the self similarity of these fractal objects, they have to be rescaled using an anisotropic transformation. A structure is said (strictly) self-similar if it can be broken into arbitrarily small pieces, each of which is a small replica of the entire structure. However, there are several variants of the mathematical definition of self–similarity. Dealing with erratic signals typical of GRB γ–ray light curves, we are mainly interested in the statistical self–similarity and self–affinity where the small replica may be somewhat distorted (for example skewed) with respect to the whole.

Higuchi Method				
mean	std	min	median	max
0.87	0.09	0.60	0.88	1.01

Aggregate Variance				
mean	std	min	median	max
0.94	0.10	0.60	0.94	1.13

Table 3.1: Statistical values for Hurst exponent methods. Right table: Higuchi method. Left table: Aggregate Variance method.

3.4.2 Hurst exponents and redshift

The correlation coefficients between redshift and Hurst exponent caculated using Higuchi method H_H and Aggregate Variance H_{AV} are $r_H = -0.1$ and $r_{AV} = -0.15$

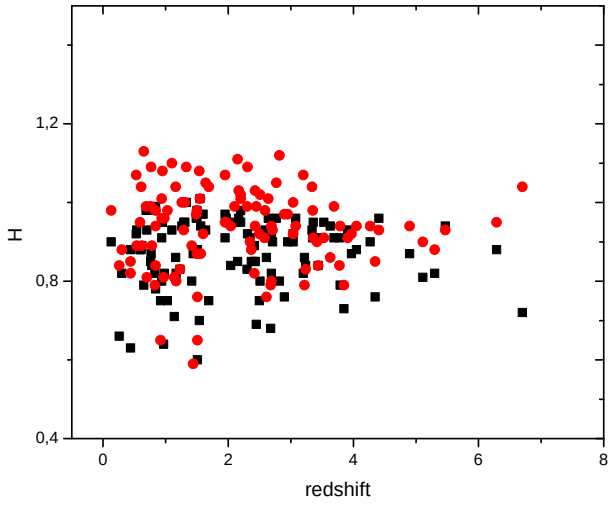

Figure 3.6: Hurst exponent versus redshift. Black squares: Aggregate Variance method. Red filled points: Higuchi method.

respectively. These results can suggest that the physics that produces the prompt emission is a correlated random process and that it is the same type of process at any distance and at any cosmological epoch. The phenomena of interest seem to present specific self-similarity patterns that do not evolve with redshift (see fig. 3.6).

Khan & Tanizuka (2001) analyze the time series data of QSO radio wave flux density using Higuchi method. They have found a relationship between z and H. In in subsequent analysis Khan & Tanizuka (2002) speculate that the relation reflects directly the source dynamics, if there is negligible effect on the wave through its propagation (the effect of the external noise accumulated on the original radio wave at the time of the wave passing through the space from the cosmological distance).

The above mentioned effects seem do not to occur in GRB high energy emission that show a universal curve structure characterized by circular dependence of similar statistical behavior in time scales having unequal duration. These nonperiodic cycles occur in various time scales probably kept alive by the central engine of GRB.

3.4.3 Noise in the time series

The errors of the data points in the SWIFT/BAT light curves are symmetric around the actual estimates, meaning that the distribution of the parent distribution is considered to be Gaussian.

A method to incorporate the measurements errors into a statistical method is through Monte Carlo simulations [7]. During each simulation every measurement is replaced by a randomly selected value coming from a Gaussian distribution having as mean the actual value of data points and as standard deviation its error. The same procedure is then repeated 1000 times and every time the same statistical method, intended to be used for analyzing the original data set, is applied to the surrogated light curves yielding an ensemble of results. Based on the distribution of the latter one can check how the measurement errors affect the method and up to which significance level the results are robust. To taking into account these errors and so consolidate the significance of our statistical result based on the quality of the data, we used the method of Timmer & Koenig (1995). In this method is randomized both the phase and the amplitude of the Fourier transform of the data set according to the noisy nature of the process.

3.5 Discussion: universal structure

In a different approach Beloborodov et al., (2000), used Fourier analysis to study the power spectral density of 214 long GRB, reveal that the diversity of GRB is due to realizations of the same process which is self–similarity over a range of time scales. The slope of the PSD was $-5/3$ suggesting that GRBs are related to fully developed turbulence. The PDS slope found by Beloborodov et al., (2000) coincides with the Kolmogorov law. The calculation of Hurst exponent in our analysis suggest opposite conclusion. The H = 1/3 value is the boundary value for the homogeneous Hurst exponent theoretically identified by Kolmogorov below which efficiency enhancing turbulence may occur.

We try to investigate the reason of the two different results.

The power spectrum analysis has been conventionally used as a useful and efficient method for analyzing an irregular time series. Especially when the power

[7] Press,W. H., Teukolsky, S. A., Vetterling, W. T., & Flannery, B. P. 1992, Numerical recipes in FORTRAN. The art of scientific computing (Cambridge: University Press, c1992, 2nd ed.)

spectrum follows the power law; the exponent α is considered to be the index for representing the irregularity of a time series. In the actual analysis of the experimental and observational data, the power spectrum shows noisy fluctuations superposed on the power law spectrum. In order to get a stable power law index, we have to take an ensemble average of the power spectra over a long interval in which the fluctuations are assumed to be statistically stationary. However, since the statistical characteristics of fluctuations often vary for a short time interval, it is not appropriate to take an average of the power spectra over a long interval. Recently studies have been done about quantitative investigation of a time series which shows non-periodic and turbulent behavior, since new ideas for describing an irregular time series have been developed. The fractal dimension is introduced as the index for describing the irregularity of a time series in place of the power law index. the power spectrum follows a single power law over all ranges of frequency. In contrast, a Kolmogorov power, spectra is valid only within the inertial range. When a time series changes its structure in time domain across a certain characteristic frequency, it is difficult to determine power law indices and a characteristic time scale from the power spectrum.

The power spectrum analysis method intrinsically requires the ensemble average of the power spectrum to get a stable result, so it tends to be significant for a lot of data points. The fractal analysis is an efficient and economical alternative to the spectral analysis for examining the irregular and self-similar time series. Moreover the work of Arkhangelskaja (2002) show an a wide range of distribution of fractal dimension of BATSE GRB with t_{90} longer than 3 seconds. The sample of Arkhangelskaja consists of 100 GRB, comparable with our Swift sample. Our results is in agree for the first peaks found in the fractal dimension distribution, although our distribution is much less scatter without the presence of multiple-modality. Fractal dimension D is tied to the Hurst exponent used to equation 2.3. Fractal dimension for Swift GRB with known redshift is D $\sim$ 1.1.

3.6 Prospective

The aim of this work is to apply this method to study and statistically characterize γ-ray burst light curves. Hurst exponent give a quantitative measure of the complexity of the signals and it represents a new sensitive observational parameter

to constrain and test GRB models and their simulated light curves. The simple relationship linking the Hurst exponent of the other methods complete the statistical description of the phenomenon in compact way and readily usable. Using Hurst exponent we obtain information on power Spectrum and autocorrelation function through a specific method for highly non-stationary and series and with a limited number of sampling points. Our analysis suggest to use for short transient phenomena the Higuchi and Aggregate Variance Method to calculate the Hurst exponent.

3.6.1 AGN and GRB

The H exponent is a time profile characteristic which is sensitive to change of shape, if there are two bursts with the same form of time profile but different duration, the H indexes of these bursts will be the same. This properties suggest us, for example, to comparison different astrophysical object: AGN and GRB. Ghisellini (2004) believe that the radiation that we receive from (GRBs) and radio loud Active Galacti Nuclei (AGNs) originates from the transformation of bulk relativistic motion into random energy. Mechanisms to produce, collimate and accelerates the jets in these sources are uncertain, and it may be fruitful to compare the characteristics of both class of sources in search of enlightening similarities. He discuss the way in which the energy in bulk relativistic motion can be transformed into beamed radiation, and consider the possibility that both classes of sources can work in the same way, namely by an intermittent release of relativistic plasma at the base of the jet: shells ejected with slightly different velocities collide at some distance from the central engine, dissipating part of their kinetic energy, and keeping the rest to power the extended radio lobes (in AGNs) or to produce the afterglow (in GRBs).

In the work of Gliozzi et al. (2002) the Hurst exponent for the X-ray emission in Ark 564 is H $\sim$ 0.3. A similar analysis was performed by Greenhough and collaborators (2002) on RXTE light curves of three galactic objects: the Crab nebula, Cygnus X-1 and the micro-quasar GRS 1915+105. The three mentioned object have a Hurst exponent consistent with the values found for Ark 564. Moreover, as reported in § Khan et al., (2001) analyze the time series data of QSO radio wave flux density using Higuchi method. They have found a relationship between z and H

Considering H $\sim$ 0.9 for BAT/Swift GRB light curve and the above mentioned H values, at this stage we can only speculate that the prompt γ–ray emission is produced by a mechanism *not exactly random* (accretion black-hole system), which reflects the work done by the central engine (quasi-periodic oscillation) during the burst generation. The explosions at lowest energy may follow a *more random pattern* with more degrees of freedom due to the properties of the surrounding cosmological environment.

The Gamma-Ray Large Area Telescope (GLAST) is able to collect more data and, thanks to its short dead time, it will record GRB signals from the deep Universe with a temporal resolution never reached before. The light curves of the GRB will be resolved up to the millisecond time scale, and their structure will be better understood. Finally the optical monitoring system like TORTORA or FAVOR (§5.2) able to capture fast transient with high time resolution sheds new light on the intrinsic properties of these objects providing multi-frequency observations characterizing the internal dynamics of the engine and its physical properties. Here we propose to characterize transient events and variable phenomena using this non-linear analysis method with the advantage that various astrophysical object (AGN, GRB) can be compared.

Table 3.2

GRB	**redshift**	H_H	**Std**	H_{AV}	**Std**
050126	1.29	0.95	0.04	0.93	0.05
050223	0.59	0.88	0.03	0.95	0.04
050315	1.95	0.97	0.02	0.95	0.04
050318	1.44	0.87	0.03	0.59	0.05
050319	3.24	0.84	0.02	0.83	0.05
050401	2.9	0.76	0.05	0.97	0.04
050416A	0.65	0.79	0.09	1.13	0.15
050502A	3.79	0.79	0.04	0.94	0.05
050505	4.27	0.9	0.02	0.94	0.05
050525	0.61	0.88	0.03	1.04	0.06
050603	2.82	0.8	0.04	1.12	0.08
050724	0.26	0.66	0.02	0.84	0.05

Continued on next page

Table 3.2 – continued from previous page

GRB	redshift	H_H	Std	H_{AV}	Std
050730	3.97	0.87	0.04	0.92	0.05
050801	1.56	0.94	0.01	0.87	0.04
050814	5.3	0.82	0.04	0.88	0.07
050820A	2.61	0.86	0.04	0.76	0.06
050824X	0.83	0.82	0.05	0.79	0.06
050826	0.3	0.82	0.04	0.88	0.05
050904	6.29	0.88	0.04	0.95	0.04
050908	3.34	0.93	0.03	1.04	0.07
050922C	2.2	0.95	0.02	1.01	0.06
051016B	0.94	0.8	0.03	0.96	0.07
051109A	2.35	0.91	0.02	0.9	0.05
051111	1.55	1.01	0.01	1.01	0.04
060115	3.53	0.95	0.03	0.91	0.04
060124	2.3	0.83	0.02	0.99	0.06
060202	0.78	0.84	0.05	0.89	0.06
060206	4.05	0.88	0.02	0.94	0.05
060210	3.91	0.93	0.02	0.91	0.06
060223A	4.41	0.96	0.02	0.93	0.04
060418	1.49	0.96	0.01	0.97	0.04
060502A	1.51	0.6	0.03	0.65	0.08
060510B	4.9	0.87	0.03	0.94	0.05
060512	0.44	0.88	0.03	0.85	0.06
060522	5.11	0.81	0.03	0.9	0.06
060604	2.68	0.68	0.04	0.79	0.06
060526	3.22	0.86	0.02	0.79	0.07
060605	3.78	0.91	0.05	0.84	0.06
060607A	3.08	0.96	0.02	0.94	0.05
060614	0.13	0.9	0.01	0.98	0.04
060707	3.42	0.91	0.03	0.9	0.06
060714	2.71	0.9	0.04	0.93	0.05
060729	0.54	0.93	0.02	0.89	0.05

Continued on next page

Table 3.2 – continued from previous page

GRB	redshift	H_H	Std	H_{AV}	Std
060814	0.84	0.98	0.02	0.98	0.03
060904B	0.7	0.93	0.02	0.81	0.06
060906	3.69	0.91	0.02	0.99	0.05
060908	2.43	0.85	0.03	1.03	0.05
060926	3.2	0.82	0.02	1.07	0.09
060927	5.47	0.94	0.01	0.93	0.03
061006	0.44	0.63	0.04	0.82	0.04
061007	1.26	0.94	0.01	1	0.04
061110A	0.76	0.85	0.03	0.99	0.04
061110B	3.44	0.84	0.03	0.84	0.05
061121	1.31	0.95	0.01	1	0.1
061126	1.16	0.86	0.03	1.04	0.05
061222B	3.36	0.95	0.03	0.91	0.06
070208	1.17	0.82	0.03	0.8	0.06
070306	1.5	0.96	0.03	0.87	0.06
070318	0.84	0.99	0.01	0.94	0.04
070411	2.95	0.9	0.04	0.97	0.05
070419A	0.97	0.64	0.03	0.81	0.07
070506	2.31	0.92	0.01	1.09	0.1
070529	2.5	0.75	0.02	0.92	0.06
070611	2.04	0.84	0.04	0.94	0.06
070612A	0.62	0.89	0.04	0.89	0.06
070714B	0.92	0.75	0.03	0.65	0.02
070721B	3.63	0.94	0.03	0.86	0.06
070802	2.45	0.69	0.03	0.99	0.07
070810A	2.17	0.96	0.01	1.03	0.06
071003	1.6	0.97	0.01	0.92	0.04
071010A	0.98	0.82	0.05	0.96	0.1
071010B	0.95	0.95	0.01	1.08	0.06
071020	2.15	0.85	0.06	1.11	0.1
071031	2.69	0.82	0.03	0.8	0.06

Continued on next page

Table 3.2 – continued from previous page

GRB	redshift	H_H	Std	H_{AV}	Std
071117	1.33	1	0.01	1.09	0.11
071122	1.14	0.71	0.03	0.81	0.06
080129	4.35	0.76	0.04	0.85	0.07
080210	2.64	0.96	0.01	1.01	0.05
080310	2.42	0.89	0.03	0.82	0.06
080319B	0.94	0.91	0.02	1.01	0.04
080319C	1.95	0.91	0.02	1.07	0.06
080330	1.51	0.88	0.02	0.76	0.04
080411	1.03	0.75	0.05	0.98	0.04
080413	2.43	0.85	0.02	0.94	0.03
080413B	1.1	0.93	0.03	1.1	0.09
080430	0.77	0.87	0.04	1.09	0.08
080520	1.54	0.7	0.03	1.08	0.17
080603B	2.69	0.91	0.01	0.94	0.04
080604	1.42	0.8	0.04	0.89	0.06
080605	1.64	0.93	0.01	1.05	0.05
080607	3.04	0.92	0.02	1	0.04
080707	1.23	0.83	0.02	0.83	0.04
080710	0.84	0.78	0.07	0.84	0.05
080721	2.59	0.93	0.02	0.98	0.05
080804	2.2	0.98	0.02	1.02	0.05
080805	1.5	0.98	0.02	0.98	0.04
080810	3.35	0.91	0.01	0.98	0.04
080905B	2.37	0.85	0.02	0.88	0.05
080913	6.7	0.72	0.02	1.04	0.08
080916A	0.69	0.98	0	0.99	0.03
080928	1.69	0.75	0.05	1.04	0.05
081007	0.53	0.92	0.01	1.07	0.08
081008	1.97	0.96	0.04	0.95	0.04
081028	3.04	0.9	0.05	0.92	0.06
081029	3.85	0.73	0.04	0.79	0.06

Continued on next page

Table 3.2 – continued from previous page

GRB	redshift	H_H	Std	H_{AV}	Std
081118	2.58	0.92	0.04	0.91	0.06
081121	2.51	0.8	0.01	1.02	0.05
081203	2.1	0.95	0.01	0.99	0.04
081222	2.77	0.96	0.01	1.05	0.04

Chapter 4

Investigation of γ-ray bursts with known redshifts: Statistical analysis of parameters.

Over ten and a half years, from February 28, 1997, to December 31, 2008, $\sim$ 580 GRBs are discovered and the redshifts are determinated for $\sim$ 150 events [1]. Such a vast volume of data already allows one to analyze general properties of GRBs, for example, to search for correlations between their particular characteristics. Such studies have already been carried out as the observational data were accumulated. This has already motivated several groups to perform a systematic analysis of observational data from various GRB observational parameters (see §2 for an exhaustive review about the detected GRB correlations).

4.1 Introduction

In this work we analyze statistical properties of 87 long-GRBs with confirmed redshift and well-sampled light curves observed in R-band (see table 4.3). The optical data gathered here show a cosmological evolution trend on various intrinsic GRB features. In particular, we find that the optical burst duration, the isotropic optical luminosity at the observed maximum and the time integrated isotropic energy are all redshift dependent. The lack of correlations between the redshift and the observational GRB quantities (i.e. optical fluence and observed peak flux) points

[1] http://www.mpe.mpg.de/ jcg/grbgen.html

out that the detected trends are not affect by significant selection effects. This fact suggests that the intrinsic optical afterglow luminosity follows the cosmological evolution of a circumburst environment which determines the optical afterglow luminosity rate. It is interesting to note that the similar analysis performed for the main parameters of the γ-ray emission show no evidence for a hypothetical redshift-dependent effect according to which the characteristics of a GRB-event depend on its location in the universe. Furthermore, there are correlations between the luminosity, the total energy and the duration of the γ-ray and optical emission separately, which can arise from universal features of the observed light curves. The linear analysis performed on the observational properties of the high energy γ–ray emission fully confirm the nonlinear analysis investigation developed in the previous chapter.

4.1.1 Subject of Investigation

The goal of this paper is a search for possible regularities in GRB properties through a statistical analysis of their characteristic parameters using the fullest possible sample of objects. As the studied quantities, we chose the optical and γ-ray emission characteristics obtained from observational data under a minimum of model assumptions. The crucial point was a study of both directly measured parameters and those reduced to the proper GRB frame, which eliminated the effects of cosmological factors. By the proper frame we mean the frame associated with a close observer located outside the object itself but at a sufficiently small distance from it. The light propagation effects due to the relativistic motion of the emitting matter (see, e.g., the review by Piran (2005) and references therein) are identical for both close and ground-based observers; as a result, the descriptions of the physical processes in these frames are equivalent. The difference between them lies only in the allowance for the cosmological GRB localization. Our sample includes 87 GRBs, from GRB 970228 to GRB 081203, with known redshifts and well-sampled optical afterglows observed in the R-band (Due to the much denser sampling in the Cousin R- band). These GRBs are characterized by the set of parameters listed below:

The **redshift** z [2] was taken from publication devoted to spectroscopic observation.

[2]http://www.mpe.mpg.de/ jcg/grbgen.html

The observed **optical peak flux** F_{opt} was obtained using the calibration of Fukugita et al. (1995) and corrected for galactic extinction (based on the map of Schlegel et al. (1998)) and for the brightness of the host galaxy (if this value is available). Host galaxy reddening correction A_R is not applied; it appears to have minimal effect on the parameter distribution.

$$F_{opt} = 1568 \times (2.15 \times 10^{-9} \times 10^{-0.4 \times mag}), [erg\, s^{-1} cm^{-2}] \tag{4.1}$$

The **isotropic equivalent Luminosity** L_{opt} optical peaks is related to the peak optical flux F_{opt} by

$$L_{opt} = 4\pi \kappa_{opt}(z) D_l^2(z) F_{opt} \tag{4.2}$$

where $D_l^2(z)$ is the luminosity distance for the cosmological standard model and $\kappa_{opt}(z)$ is the cosmological κ correction that takes into account the transformation of the R passband in the proper GRB frame:

$$\kappa_{opt} = \frac{\int_{\frac{\nu R_0}{(1+z)}}^{\frac{\nu R_1}{(1+z)}} \nu^{-\beta} d\nu}{\int_{\nu R_0}^{\nu R_1} \nu^{-\beta} d\nu} = \frac{1}{(1+z)^{1-\beta}} \tag{4.3}$$

Here, ν_{R0} and ν_{R1} are the frequency boundaries of the R band and β is the power-law index in the optical spectrum $F_\nu \propto \nu^{-\beta}$. In the absence of information about β, we used $\beta = 0.7$, which is close to its statistically mean estimate, for the specific GRB.

The **optical fluence** S_{opt} was determined by numerically integrating the afterglow light curve in the interval from the earliest observation to the latest one with a power-law interpolation of the flux in the segments between the experimental points. Since only part of the optical afterglow can be recorded in practice, this parameter is a lower limit for the fluence.

The **isotropic equivalent of the total optical energy** in R band E_{opt} in the rest frame of the source was determinates from the optical fluence S_{opt} using the relation:

$$E_{opt} = \frac{4\pi\kappa_{opt}(z)D_l^2(z)S_{opt}}{(1+z)} \tag{4.4}$$

The **optical duration** $t_{90,opt}$ was determined as the time since the afterglow detection during which 90 % of the optical fluence was received.

The prompt optical emission in the proper frame $T_{90,opt}$ was calculated as $t_{90,opt}/(1+z)$

The **delay of the optical peak** relative to the time of burst detection in γ-ray, t_{peak}, and the corresponding delay in the proper frame $T_{peak} = t_{peak}/(1+z)$

The **power–law index** α of the flux decay with time in the dependence $F \propto t^{-\alpha}$ at the initial observed afterglow phase. Combined residual test are applied to obtain the best-fit power law at early stage.

The **γ-ray fluence** S_γ was determined from published observations by reducing them to the energy range 15–150 keV. In this case, only the time-integrated (averaged) γ-ray spectrum was used. The **isotropic equivalent of the peak γ–ray luminosity** in the energy range 15–150 keV for the proper burst frame L_{iso} was calculated from the peak γ-ray flux using the formula

$$L_{iso} = 4\pi\kappa_\gamma(z)D_l^2(z)F_\gamma \tag{4.5}$$

where $\kappa_\gamma(z)$ is the k correction defined as (see, e.g., Bloom et al. 2001)

$$k_\gamma(z) = \frac{\int_{E_1/(1+z)}^{E_2/(1+z)} F_E(E)dE}{\int_{e_1}^{e_2} F_E(E)dE} \tag{4.6}$$

Here, F_E is the spectral flux density, e_1 and e_2 are the lower and upper boundaries of the energy range in which F_γ was obtained, E_1 and E_2 are the boundaries of the energy range of interest in the proper burst frame.

The **isotropic equivalent of the total γ–ray energy** (the energy range 15–150 keV in the proper burst frame) E_{iso} was derived from the γ–ray fluence using the formula

$$E_{iso} = \frac{4\pi\kappa_\gamma(z)D_l^2(z)S_\gamma}{(1+z)} \tag{4.7}$$

As the **GRB prompt emission duration** t_γ, we used the universally accepted parameter t_{90} that is published in the results of γ-ray observations.

The GRB duration in the proper frame was determined from the relation $T_\gamma = t_\gamma/(1+z)$ without applying any corrections for the change in the energy range.

The subsequent work was carried out with two samples: the *observed* one or the sample of observed parameters (z, F_{opt}, S_{opt}, t_{90opt}, t_{peak}, F_γ, S_γ, t_γ, α) and the *intrinsic* one or the sample of intrinsic parameters (z, L_{opt}, E_{opt}, T_{90opt}, T_{peak}, L_{iso}, E_{iso}, T_γ, α) Additional optical parameters are added to our investigation using the interpolated/extrapoleted light curves. We consider the **extrapolated optical luminosity** L_{exp} immediately after the corresponding duration of the prompt γ-ray emission in the rest frame of the source. The extrapolation is performed using the slope α calculated at early stage. Considering L_{tot} parameter, we extrapolate the **total energy** E_{tot} and **total time duration** T_{tot} of the optical afterglow.

To study in detail the dynamics of external shocks and their relation to the interstellar medium, do not take into account the optical peaks that occurred simultaneously with the prompt γ–ray emission phases (e.g, GRB 990123, GRB 050904, GRB 080319B). In 11 GRBs in our sample we detect well-observed peaks during the afterglow evolution when the γ–ray activity is ended or is below the detection threshold of satellites instruments. For this sub-sample of objects the peak luminosity is indicated with L_{peak} symbol (§4.3).

4.1.2 Statistical Analysis of Parameters

We determined the correlation coefficients for the parameters in various pair combinations and performed a linear least-squares fitting. (for the correlations with Pearson correlation coefficients $r > 0.5$). The differences in measurement accuracy were taken into account by weighting, where possible. Unfortunately, for some reasons, this procedure did not always yield satisfactory results. In particular, since we used a large number of sources of data obtained by different observational groups and published at different times, it was difficult to ensure that the confidence probabilities of the error estimates for all quantities coincided (e.g., for the 1 σ level). For some of the measurements, the errors were not published at all (in these cases, the relative error was taken to be 10 %). In addition, since the observations were carried out with different instruments using different techniques, the spread in errors is quite significant (up to an order of magnitude). For

this reason, the result was occasionally shifted to points with particularly small declared errors that did not correspond to the actual experimental accuracy. For example, in many cases, hundredths or even thousandths of a magnitude are given as the errors of optical observations, although the differences between the brightness estimates simultaneously obtained by different groups reach several tenths of a magnitude. The latter value probably corresponds to the actual measurement accuracy. Finally, even if the error estimates are comparatively reliable, the spread in parameters can exceed noticeably the errors themselves and weighting will change the formal regression accuracy only slightly, leading, nevertheless, to a distortion of the correlation coefficient due to the influence of several estimates with small formal errors. The results of our analysis of the pair correlations between the parameters of the *observed* and *intrinsic* samples are presented in Tables 4.1 and 4.2, respectively. The linear regression coefficients for the most significant correlations and the significance levels (SL), the probabilities of the errors of the first kind when the null hypothesis about the complete lack of correlation ($r = 0$) between the parent populations of the corresponding parameters is rejected, are given in each corresponding plot.

Table 4.2: Pearson correlation coefficients for the observed GRB parameters.
The calculation is performed in logarithmic values of the quantities. The *observed* quantities show a weaker correlation, which is indicative of the actual physical relationships between the characteristics of afterglows in their proper reference frame.

		log F_{opt}	**log** S_{opt}	**log** t_{opt}	**log** t_{peak}	**log** F_{iso}	**log** S_{iso}	**log** t_{iso}
z	0.15	-0.13	-0.40	-0.25	-0.51	-0.41	-0.01	-0.11
log F_{opt}		0.57	-0.14	-0.74	-0.09	0.01	0.02	-0.04
log S_{opt}			0.65	0.01	0.22	0.35	0.26	0.24
log t_{opt}				0.57	0.37	0.35	0.25	0.36
log t_{peak}					0.38	0.34	0.14	0.43
log F_{γ}						0.73	-0.06	0.47
log S_{γ}							0.42	0.31
log t_{γ}								-0.15

Table 4.1: Pearson correlation coefficients for the intrinsic GRB parameters.
The calculation is performed in logarithmic values of the quantities.

	$\log T_{\gamma}$	$\log T_{peak}$	$\log L_{opt}$	$\log E_{opt}$	$\log L_{peak}$	$\log T_{90}$	$\log L_{iso}$	$\log E_{iso}$	$\log \alpha$	$\log E_{tot}$	$\log L_{exp}$	$\log T_{tot}$
z	-0.22	-0.34	**0.57**	0.52	**0.92**	**-0.65**	0.35	0.38	-0.00	0.12	0.10	-0.24
$\log T_{\gamma}$		0.27	-0.24	-0.05	-0.55	0.14	-0.43	0.05	0.24	0.01	-0.07	0.24
$\log T_{peak}$			**-0.79**	-0.35	-0.04	0.53	-0.14	-0.18	0.41	0.46	0.30	1.00
$\log L_{opt}$				**0.76**	...	**-0.65**	0.39	0.48	-0.16	-0.06	0.03	**-0.76**
$\log E_{opt}$					**0.78**	-0.48	0.39	0.54	0.02	0.21	0.19	-0.28
$\log L_{peak}$						-0.53	0.48	0.32	-0.11	**0.92**	0.98	-0.01
$\log T_{90}$							-0.29	-0.34	0.15	0.16	0.18	0.51
$\log L_{iso}$								**0.79**	0.21	0.15	0.17	-0.00
$\log E_{iso}$									0.29	0.34	0.36	-0.05
$\log \alpha$										0.45	0.31	0.44
$\log E_{tot}$											**0.82**	0.45
$\log L_{exp}$												0.30

4.1.3 Correlations between Optical Afterglow Characteristics

Significant correlations were found between the total energies (E_{opt}) and peak luminosity (L_{opt}) of afterglows (r = 0.78), between the peak luminosity and the times of the peak T_{peak}, (r = -0.79), between the peak luminosity and durations of afterglows (T_{90opt}, r = -0.65). The analogues of these parameters in the *observed* quantities show a weaker correlation, which is indicative of the actual physical relationships between the characteristics of afterglows in their proper reference frame. For some of the parameters (primarily for L_{opt} and E_{opt}), similar relationships were established when smaller GRB samples were analyzed (Beskin et al. 2000; Bartolini et al. 2001; Greco et al. 2007). As was noted above, a overwhelming majority of the peak luminosity (or fluxes in the observed sample) actually correspond only to more or less early afterglow flux measurements. In other words, when the detection times of the optical emission from a GRB change, we observe different phases of its afterglow. In this case, it would be natural to assume that the detected correlations result from a comparative universality of the power-law pattern of these curves, $L(T) \propto T^{-\alpha}$. In particular, this is directly confirmed by the high significance of the $\log L_{opt}$ vs $\log T_{peak}$ correlation.

4.1.4 Correlations between γ-Ray Emission Parameters

Another type of clearly revealed correlation is the relationship between the γ-ray luminosity and total energies of bursts

By analogy with the above correlations, it would be natural to assume that these correlations also result from a universal pattern of the γ-ray light curves. Suppose that they are in the shape of pulses with a fast rise and an exponential decay (FRED pulses), L(T) $\propto L_0\, exp(-T/T_0)$, where L_0 and T_0 are the normalization coefficients. Then, $E_{iso,FRED}$ = [L(T_i)–L(T_f)]T_0, where the subscripts i and f correspond to the initial and final times of the exponential pulse decay and the time is measured from some zero point. If T_f is sufficiently large ($L(T_f) \longrightarrow 0$), then $\log E_{iso,FRED} \approx \log L(T_i) + \log T_0$. It is easy to verify that this relationship corresponds to the detected one at a characteristic time $T_0 \approx 1$ sec . Indeed, according to Piran (2005), this value is close to the mean pulse duration. Thus, if the above assumption is valid, then the brightest burst pulse makes a major

contribution to the γ-ray energy of the bursts with detected afterglows.

4.1.5 Optical Clusterization analysis

The clusterization phenomena in optical light curve at middle time after the main γ–ray emission was discovered by Nardini et al. (2006); Liang et a. (2006); Kann et al. (2008) and by Gendre et al. (2008) who extended this study towards infrared wavelengths. Hints of standardization of the X-ray afterglow luminosity were first discovered by Boër & Gendre (2000), who found evidences for clustering in the X-ray luminosity of BeppoSAX afterglows. The cluster is an other important observational clue who that suggests that the afterglow light curves have a universal structure. One scheme might be that GRB jets are initially structured

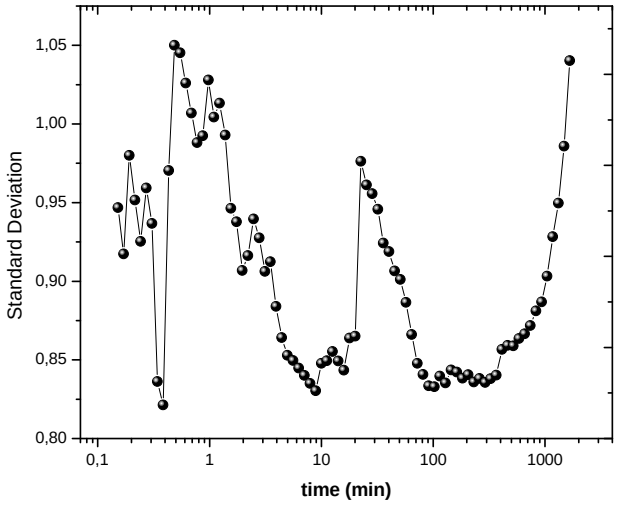

Figure 4.1: Standard deviation vs time in rest frame of the source.

(e.g, Rossi et al. 2002), and the early γ-ray and X-ray properties are sensitive to the observational viewing angle. The jet structure tends to smear out with time, so that at later times, the outflow is more isotropic and the viewing angle effect no longer plays an essential role (see §6). We interpolate the observational data and calculate the average bin-luminosity at different epochs. The average of the bin reported in table 4.2, grows exponentially according to the time of sampling and afterglow variability. The shocks with the interstellar medium should follow a smoother behavior than the internal shock interactions, so sudden changes in the

intrinsic afterglow variability do not expect. The graph 4.1 shows the standard deviation trends of the of the bin luminosity during the time for the extrapolated light optical curves. A substantial decrease in standard deviation are found at t=10 min and t > 100 min.

Our sample do not show statistical evidence for bimodality luminosity distribution claim by Nardini et al. (2006; 2008); Liang et al. (2006) and Kann et al. (2008) in any analyzed epoch. Also the ultra-luminous GRBs (GRB 080319B, GRB 050904, GRB 061007 and GRB 080319B) show intrinsic standard behavior at middle/late time stage of their afterglow decay.

Table 4.3: Statistical parameters for interpolated bin-luminosity at various epochs

time	N	mean	Std	sum	minimum	median	maximum
0.15	6	47.05	0.95	282.30	45.54	47.23	47.94
0.17	8	47.14	0.92	377.09	45.51	47.20	48.05
0.19	9	47.04	0.98	423.37	45.49	46.91	48.24
0.22	11	47.02	0.95	517.20	45.46	46.89	48.43
0.24	14	47.00	0.93	657.99	45.44	46.97	48.62
0.27	15	47.04	0.96	705.56	45.41	46.89	48.80
0.31	17	46.99	0.94	798.89	45.39	46.84	48.99
0.34	21	47.00	0.84	986.91	45.36	46.89	48.99
0.39	22	46.93	0.82	1032.43	45.34	46.81	48.86
0.43	23	47.02	0.97	1081.40	45.31	46.77	49.62
0.49	24	47.09	1.05	1130.11	45.29	46.86	49.57
0.55	26	46.99	1.05	1221.86	45.26	46.84	49.45
0.61	28	46.89	1.03	1312.82	45.24	46.78	49.31
0.69	28	46.85	1.01	1311.92	45.21	46.73	49.31
0.77	28	46.82	0.99	1311.00	45.19	46.69	49.31
0.87	29	46.74	0.99	1355.48	45.16	46.65	49.32
0.98	30	46.77	1.03	1403.22	45.14	46.62	49.49
1.10	31	46.77	1.00	1449.75	45.11	46.65	49.66
1.23	32	46.70	1.01	1494.26	45.09	46.57	49.71
1.38	34	46.74	0.99	1589.02	45.06	46.58	49.50
1.55	36	46.69	0.95	1680.72	45.03	46.58	49.30
1.75	38	46.61	0.94	1771.14	44.97	46.56	49.09
1.96	40	46.61	0.91	1864.35	44.94	46.56	48.98
2.20	41	46.53	0.92	1907.68	44.91	46.48	48.88
2.47	43	46.42	0.94	1995.99	44.86	46.39	48.79
2.78	43	46.37	0.93	1993.98	44.84	46.31	48.69
3.12	44	46.30	0.91	2037.22	44.83	46.16	48.59
3.51	45	46.22	0.91	2080.05	44.69	46.10	48.50
3.94	46	46.18	0.88	2124.25	44.76	46.10	48.40
4.43	47	46.15	0.86	2169.04	44.69	46.10	48.30
4.97	49	46.07	0.85	2257.52	44.63	46.07	48.21
5.59	50	46.05	0.85	2302.59	44.57	46.01	48.11
6.27	50	46.00	0.84	2299.84	44.50	45.91	48.01
7.05	50	45.95	0.84	2297.53	44.44	45.86	47.92
7.92	50	45.90	0.84	2295.20	44.38	45.84	47.82
8.89	51	45.84	0.83	2337.68	44.31	45.74	47.73
9.99	53	45.78	0.85	2426.31	44.25	45.67	47.63
11.22	53	45.74	0.85	2424.00	44.18	45.63	47.53
12.61	53	45.69	0.86	2421.65	44.12	45.58	47.44
14.16	53	45.65	0.85	2419.29	44.05	45.52	47.34
15.91	53	45.60	0.84	2417.01	43.98	45.42	47.24
17.87	55	45.60	0.86	2507.96	43.91	45.36	47.42
20.08	55	45.56	0.87	2505.81	43.85	45.37	47.39
22.55	56	45.46	0.98	2545.74	42.04	45.31	47.37
25.33	57	45.43	0.96	2589.76	42.11	45.29	47.28
28.46	56	45.40	0.96	2542.42	42.17	45.30	47.23
31.97	56	45.35	0.95	2539.71	42.17	45.26	47.19
35.91	57	45.29	0.92	2581.27	42.17	45.21	47.01

Continued on next page

Table 4.3 – continued from previous page

time(min)	N	mean	Std	sum	minimum	mediam	maximum
40.34	57	45.23	0.92	2578.24	42.19	45.12	46.86
45.31	58	45.18	0.91	2620.52	42.23	45.11	46.88
50.90	58	45.12	0.90	2617.16	42.28	45.01	46.86
57.17	59	45.07	0.89	2659.20	42.32	45.04	46.76
64.23	61	45.04	0.87	2747.38	42.37	45.07	46.65
72.15	61	44.99	0.85	2744.69	42.41	45.04	46.54
81.04	62	44.96	0.84	2787.73	42.46	45.05	46.47
91.04	63	44.92	0.83	2829.99	42.50	45.04	46.54
102.27	63	44.88	0.83	2827.68	42.49	44.97	46.61
114.88	64	44.85	0.84	2870.47	42.48	44.91	46.68
129.04	64	44.79	0.84	2866.47	42.47	44.85	46.75
144.96	64	44.75	0.84	2863.75	42.46	44.81	46.74
162.83	64	44.69	0.84	2860.37	42.30	44.76	46.68
182.92	67	44.64	0.84	2990.82	42.12	44.77	46.62
205.47	67	44.58	0.84	2987.08	41.95	44.72	46.57
230.81	68	44.51	0.84	3026.83	41.77	44.60	46.51
259.28	68	44.47	0.84	3023.65	41.60	44.57	46.45
291.25	69	44.41	0.84	3064.49	41.42	44.56	46.40
327.17	70	44.37	0.84	3105.84	41.25	44.52	46.34
367.52	70	44.32	0.84	3102.07	41.07	44.45	46.29
412.85	70	44.27	0.86	3099.19	40.90	44.43	46.31
463.76	71	44.24	0.86	3141.11	40.72	44.40	46.23
520.95	73	44.16	0.86	3223.66	40.55	44.24	46.15
585.20	74	44.10	0.86	3263.58	40.37	44.26	46.10
657.37	74	44.04	0.87	3258.79	40.20	44.10	46.05
738.44	76	43.99	0.87	3343.06	40.02	44.04	46.00
829.50	76	43.92	0.88	3337.81	39.84	43.96	45.94
931.80	78	43.86	0.89	3420.83	39.67	43.89	45.95
1046.72	79	43.79	0.90	3459.15	39.49	43.89	45.91
1175.80	79	43.71	0.93	3453.09	39.32	43.82	45.87
1320.80	79	43.65	0.95	3448.16	39.14	43.70	45.84
1483.69	79	43.58	0.99	3443.16	38.97	43.61	45.80
1666.67	79	43.52	1.04	3437.94	38.79	43.55	45.76
0.15	6	47.05	0.95	282.30	45.54	47.23	47.94
0.17	8	47.14	0.92	377.09	45.51	47.20	48.05
0.19	9	47.04	0.98	423.37	45.49	46.91	48.24
0.22	11	47.02	0.95	517.20	45.46	46.89	48.43
0.24	14	47.00	0.93	657.99	45.44	46.97	48.62
0.27	15	47.04	0.96	705.56	45.41	46.89	48.80
0.31	17	46.99	0.94	798.89	45.39	46.84	48.99
0.34	21	47.00	0.84	986.91	45.36	46.89	48.99
0.39	22	46.93	0.82	1032.43	45.34	46.81	48.86
0.43	23	47.02	0.97	1081.40	45.31	46.77	49.62
0.49	24	47.09	1.05	1130.11	45.29	46.86	49.57
0.55	26	46.99	1.05	1221.86	45.26	46.84	49.45
0.61	28	46.89	1.03	1312.82	45.24	46.78	49.31
0.69	28	46.85	1.01	1311.92	45.21	46.73	49.31
0.77	28	46.82	0.99	1311.00	45.19	46.69	49.31
0.87	29	46.74	0.99	1355.48	45.16	46.65	49.32
0.98	30	46.77	1.03	1403.22	45.14	46.62	49.49
1.10	31	46.77	1.00	1449.75	45.11	46.65	49.66
1.23	32	46.70	1.01	1494.26	45.09	46.57	49.71
1.38	34	46.74	0.99	1589.02	45.06	46.58	49.50
1.55	36	46.69	0.95	1680.72	45.03	46.58	49.30
1.75	38	46.61	0.94	1771.14	44.97	46.56	49.09
1.96	40	46.61	0.91	1864.35	44.94	46.56	48.98
2.20	41	46.53	0.92	1907.68	44.91	46.48	48.88
2.47	43	46.42	0.94	1995.99	44.86	46.39	48.79
2.78	43	46.37	0.93	1993.98	44.84	46.31	48.69
3.12	44	46.30	0.91	2037.22	44.83	46.16	48.59
3.51	45	46.22	0.91	2080.05	44.69	46.10	48.50
3.94	46	46.18	0.88	2124.25	44.76	46.10	48.40
4.43	47	46.15	0.86	2169.04	44.69	46.10	48.30
4.97	49	46.07	0.85	2257.52	44.63	46.07	48.21
5.59	50	46.05	0.85	2302.59	44.57	46.01	48.11
6.27	50	46.00	0.84	2299.84	44.50	45.91	48.01
7.05	50	45.95	0.84	2297.53	44.44	45.86	47.92
7.92	50	45.90	0.84	2295.20	44.38	45.84	47.82
8.89	51	45.84	0.83	2337.68	44.31	45.74	47.73

Continued on next page

Table 4.3 – continued from previous page

time(min)	N	mean	Std	sum	minimum	mediam	maximum
9.99	53	45.78	0.85	2426.31	44.25	45.67	47.63
11.22	53	45.74	0.85	2424.00	44.18	45.63	47.53
12.61	53	45.69	0.86	2421.65	44.12	45.58	47.44
14.16	53	45.65	0.85	2419.29	44.05	45.52	47.34
15.91	53	45.60	0.84	2417.01	43.98	45.42	47.24
17.87	55	45.60	0.86	2507.96	43.91	45.36	47.42
20.08	55	45.56	0.87	2505.81	43.85	45.37	47.39
22.55	56	45.46	0.98	2545.74	42.04	45.31	47.37
25.33	57	45.43	0.96	2589.76	42.11	45.29	47.28
28.46	56	45.40	0.96	2542.42	42.17	45.30	47.23
31.97	56	45.35	0.95	2539.71	42.17	45.26	47.19
35.91	57	45.29	0.92	2581.27	42.17	45.21	47.01
40.34	57	45.23	0.92	2578.24	42.19	45.12	46.86
45.31	58	45.18	0.91	2620.52	42.23	45.11	46.88
50.90	58	45.12	0.90	2617.16	42.28	45.01	46.86
57.17	59	45.07	0.89	2659.20	42.32	45.04	46.76
64.23	61	45.04	0.87	2747.38	42.37	45.07	46.65
72.15	61	44.99	0.85	2744.69	42.41	45.04	46.54
81.04	62	44.96	0.84	2787.73	42.46	45.05	46.47
91.04	63	44.92	0.83	2829.99	42.50	45.04	46.54
102.27	63	44.88	0.83	2827.68	42.49	44.97	46.61
114.88	64	44.85	0.84	2870.47	42.48	44.91	46.68
129.04	64	44.79	0.84	2866.47	42.47	44.85	46.75
144.96	64	44.75	0.84	2863.75	42.46	44.81	46.74
162.83	64	44.69	0.84	2860.37	42.30	44.76	46.68
182.92	67	44.64	0.84	2990.82	42.12	44.77	46.62
205.47	67	44.58	0.84	2987.08	41.95	44.72	46.57
230.81	68	44.51	0.84	3026.83	41.77	44.60	46.51
259.28	68	44.47	0.84	3023.65	41.60	44.57	46.45
291.25	69	44.41	0.84	3064.49	41.42	44.56	46.40
327.17	70	44.37	0.84	3105.84	41.25	44.52	46.34
367.52	70	44.32	0.84	3102.07	41.07	44.45	46.29
412.85	70	44.27	0.86	3099.19	40.90	44.43	46.31
463.76	71	44.24	0.86	3141.11	40.72	44.40	46.23
520.95	73	44.16	0.86	3223.66	40.55	44.24	46.15
585.20	74	44.10	0.86	3263.58	40.37	44.26	46.10
657.37	74	44.04	0.87	3258.79	40.20	44.10	46.05
738.44	76	43.99	0.87	3343.06	40.02	44.04	46.00
829.50	76	43.92	0.88	3337.81	39.84	43.96	45.94
931.80	78	43.86	0.89	3420.83	39.67	43.89	45.95
1046.72	79	43.79	0.90	3459.15	39.49	43.89	45.91
1175.80	79	43.71	0.93	3453.09	39.32	43.82	45.87
1320.80	79	43.65	0.95	3448.16	39.14	43.70	45.84
1483.69	79	43.58	0.99	3443.16	38.97	43.61	45.80
1666.67	79	43.52	1.04	3437.94	38.79	43.55	45.76

4.2 Cosmological evolution of the optical afterglow properties

Average cosmological evolution trend may be appreciated during particular time of the afterglow emission. In the following analysis we show that the intrinsic optical afterglow luminosity follows a redshift-dependent effect according to which the characteristics of the early afterglow event depend on its location in the universe.

The random detected peak luminosity in our sample have a dependence on redshift ~ 0.56.

This interesting picture invites us to divide the total sample into three parts:

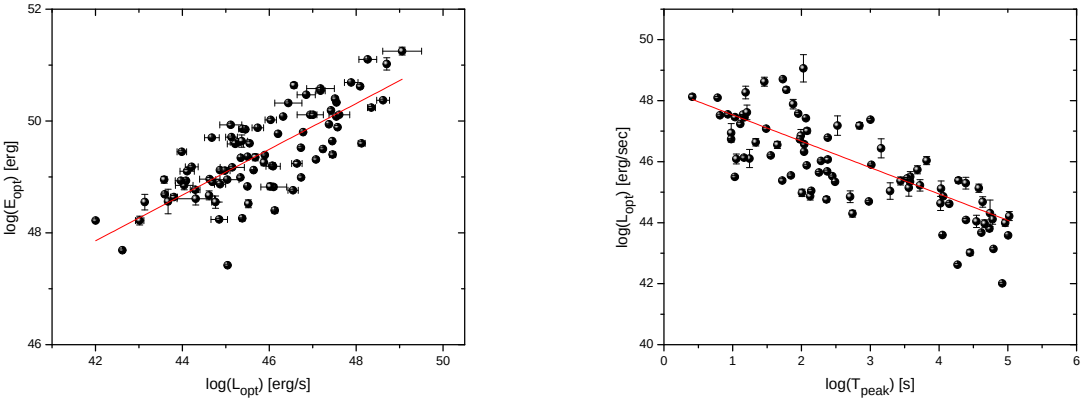

Figure 4.2: Left: E_{opt} vs L_{opt}. $E_{opt} = (30.67 \pm 16.08) \times L_{opt}^{(0.41 \pm 0.35)}$
Right: L_{opt} vs T_{peak}. $L_{opt} = (48.26 \pm 0.23) \times T_{peak}^{(-0.89 \pm 0.08)}$

I. Early Optical Luminosity: $L_{opt,<100}$, luminosity detected in the time range of the rest frame of the source in $t < 100$ sec.

II. Middle Optical Luminosity: $L_{opt,100-6000}$, luminosity detected in the time range of the rest frame of the source in $100sec < t < 6000$ sec.

III. Late Optical Luminosity: $L_{opt,>6000}$, luminosity detected in the time range of the rest frame of the source in $1000sec < t < 6000$ sec.

The time duration is chosen in order to obtain approximately the same number of events in each subsample and in according to the clusterization phases of the afterglow (see graph 1.1) At early stage the trend correlation is $r = 0.27$ for 30 points, at middle time r=0.78 (SL=6.50×10^{-8}) for 33 GRB and finally the correlation coefficient $r = 0.63$ for 24 (SL=7.74×10^{-4}) GRB at late time.

4.3 Luminosity optical peak and cosmological evolution

In our sample there are 11 well-detected peaks that are not coincident with the work of the γ-ray activity phase. To date: GRB 050730, GRB 060206, GRB 060210,GRB 060605, GRB 060904B, GRB 060926 GRB 070411A, GRB 070419A, GRB 071010A, GRB 071010B, GRB 080330. Their peak structure is far from 'γ–ray afterglow' (extended late time emission) They are important tool to study the

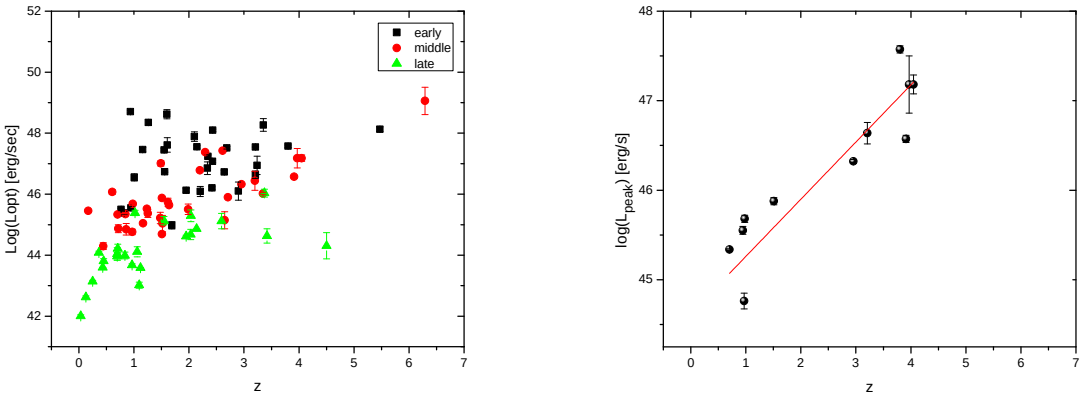

Figure 4.3: Left: *Lopt* vs z. The sample is divided in three sub-sample in according to the peak time in the rest frame of the source.
Right: L_{peak} vs z. $L_{peak} = (44.62 \pm 2.90) \times z^{(0.63 \pm 0.87)}$

properties of the interstellar medium and the physical mechanism of the external shock emission during the transition phases. The maximum peak Luminosity L_{peak} for these objects have a strong correlation with the redshift, r=0.92 ($SL = 5.46 \times 10^{-5}$).

Table 4.4: GRB sample with known spectroscopic redshift and well-sampled R-band light curves

GRB	redshift	GRB	redshift	GRB	redshift
970228	0.69	040924	0.86	061007	1.26
970508	0.83	041006	0.72	061121	1.31
971214	3.42	050315	1.95	061126	1.16
980613	1.10	050319	3.24	070125	1.55
980703	0.97	050401	2.90	070208	1.17
990123	1.60	050408	1.24	070411A	2.95
990510	1.62	050525	0.61	070419A	0.97
990712	0.43	050730	3.97	071003	1.60
991208	0.71	050801	1.56	071010A	0.98
991216	1.02	050820	2.61	071010B	0.95
000131	4.50	050904	6.29	071020	2.15
000301C	2.03	050908	3.34	071112C	0.82
000418	1.12	050922C	2.20	080210	2.64

Continued on next page

Table 4.4 – continued from previous page

GRB	redshift	GRB	redshift	GRB	redshift
000911	1.06	051109	2.35	080310	2.42
000926	2.04	051111	1.55	080319B	0.94
010222	1.48	060124	2.30	080319C	1.95
010921	0.45	060206	4.05	080330	1.51
011121	0.36	060210	3.91	080413A	2.43
011211	2.14	060218	0.03	080430	0.77
020124	3.20	060418	1.49	080603A	1.69
020405	0.69	060502	1.51	080603B	2.69
020813	1.25	060512	0.44	080605	1.64
020903	0.25	060526	3.21	080710	0.84
021004	2.34	060605	3.80	080721	2.59
021211	1.01	060614	0.13	080804	2.20
030226	1.99	060714	2.71	080810	3.35
030323	3.37	060904B	0.70	081203	2.10
030328	1.52	060908	2.43		
030329	0.17	060926	3.21		
030429	2.65	060927	5.47		

4.4 Discussion and conclusion

Our statistical analysis has tried to answer the following questions:

I. Are there evidence of cosmological evolution on γ-ray burst features?

II. Are there evidence of cosmological evolution on optical afterglow?

III. Despite the morphological differences between the high-energy emission and their afterglows, can we assume a universal underlying structure for both emissions?

IV. The intrinsic properties of prompt γ-ray emission show some degree of correlation with their afterglows or the afterglow 'forget' the initial physical conditions ?

The problem about the cosmological evolution of the GRB properties is interesting in many ways. It sheds new light on the possible progenitors because the

redshift of GRB span from 0.00856 to 6.695. Moreover if the GRB properties may evolve with redshift the proposed luminosity indicators should consider this.

Between the luminosity indicators proposed over the years and described previously ($E_{peak} - E_{iso}$, $E_{peak} - L_{iso}$, $L_{iso} - T_{0.45}$, $L_{iso} - V$, $N_{peak} - L_{iso}$, $L_{iso} - \tau_{lag}$) only the luminosity spectral lag relation is corrected for a possible cosmological trend from the work of Tsutsui et al (§1.1). However this correction was made using redshift derived from other reported relationship. There have been suggestions that prompt GRB properties may evolve with redshift (e.g. Amati et al. 2002; Wei & Gao 2003; Yonetoku et al. 2004).

We have demonstrated, for a sample of 87 GRB with confirm spectroscopic redshift, that the properties of the γ-ray emission are not affected by any cosmological evolution. On the other hand the first stage of the afterglow evolution has a dependence on redshift and is even clearer if we consider the peaks that arise when the prompt γ-ray emission has been completely extinguished.

It is generally accepted that both the GRB and the afterglow arise due to dissipation of the kinetic energy of the relativistic flow. The relativistic motion can be dissipated by either external or internal shocks. The first involve slowing down by the external medium surrounding the burst. This would be the analogue of a supernova remnant in which the ejecta is slowed down by the surrounding ISM. Like in SNRs external shocks can dissipate all the kinetic energy of the relativistic flow. On the other hand internal shocks are shocks within the flow itself. These take place when faster moving matter takes over a slower moving shell. In this scenario, the internal shock is not affected by the cosmological surrounding while the external shocks interact with the circum-burst environment and carry with them the signatures of different cosmological epochs.

However, it is not the whole evolution of afterglows to be redshift-dependent, but only particular stages of its evolution.

The internal shocks take place at a distance $R_{int} \sim c\delta t\Gamma^2$. These shocks last as long as the inner engine is active. The typical observed time scale for this activity $\sim$ 50sec (for long bursts) and $\sim$ 0.5sec (for short ones). External shocks begin at $R_{ext} \sim 10^{16}$cm. If $R_{ext}/\Gamma^2 \leq T = \Delta/c$, namely if the burst is long, the afterglows begins while internal shocks are still going on and the initial part of the afterglow overlaps the late (Sari, 1997) part of the GRB. So when the γ–ray afterglow is completely extinguished, the external shock following the evolution of the Universe around them. This phase lasts a few minutes, after the light curves

gradually standardize showing common behavior. We believe the the redshift-dependence is well-observed in the peaks that arise during the afterglow evolution, because their energy exceeds the residual γ–ray flow that contaminates the optical emission during the transition phase between internal/external shock.

Recently also Stratta et al., (2008) report a cosmological evolution in X-ray afterglow features (§2.2).

Finally the properties of prompt γ-ray flux seem do not show correlation with the intrinsic properties of their afterglows in according to the internal/external shock scenario.

Chapter 5

Tortora Project: sub-second universe analysis

Dietro ogni problema c'è sempre un'opportunità.

Galileo Galilei

This chapter presents my collaboration in TORTORA team; the scientific goal of the TORTORA project, the description of the set of equipment and the main installation phase on the top of the REM robotic telescope are described. The short introduction about the activity of GRB Coordinates Network (GCN) shows that the first available optical observations (with the exception of rare cases) have an essential instrumental delay. The loss of optical information at initial stage of γ-ray emission not allow us to study in detail the multi-frequency behaviour of the central engine. Internal spatial structure, dynamics of the GRBs and processes transforming their energy into γ–ray radiation are inevitably reflected within the temporal properties of the bursts (see Piran, 2005 and references therein). Indeed, while the full length of the GRBs varies in the 0.1 - 100 sec range, their light curves in 80% cases of the long bursts present substructures (§3). Moreover, millisecond features are discovered in the light curves of some long bursts (McBreen et al., 2004).

For successful observations of optical emission as well as possible optical precursors from γ-ray bursts, one should monitor the sky *continuously* to be independent from space–borne telescopes. The technology involved in TORTORA instrument seek to remedy these observational problems by combining two essential characteristics i.e. the wide field of view and the high time resolution. The *CCD + image intensifier layout* allows to observe sky in wide field with high temporal resolution effectively. Fast Wide-Field Camera TORTORA operated from May 2006 at the ESO-La Silla Observatory has successfully observed the prompt optical emission of the remarkable case of the naked-eye GRB 080319B (§ 6).

Here we describe the design and implementation of TORTORA camera (Telescopio Ottimizzato per la Ricerca dei Transienti Ottici RApidi) mounted on top of REM robotic telescope at La-Silla Observatory (ESO, Chile), and the complete two-telescope TORTOREM system developed by our group. A brief comparison with its prototype *FAVOR* (FAst Variability Optical Registration) placed near Russian 6-m telescope in North Caucasus are also given.

5.1 Communication System in GRB community

5.1.1 GRB Coordinates Network

Historically the dissemination of the spacecraft localisation information from onboard or ground analysis to the ground-based GRB follow-up community was first done through publications and informal channels; later, when the need for greater speed and higher efficiency became apparent, the BACODINE (BAtse COordinates DIstribution NEtwork) system was inaugurated in 1992 to rapidly communicate processed and analyzed GRB data from the BATSE instrument on the CGRO spacecraft to the community. After the spectacular success of the BeppoSAX spacecraft in rapidly providing a precise localisation of GRB 970228 and the subsequent discovery of the afterglow at many wavelengths, the BACODINE messaging system was transformed into the present GRB Coordinates Network (GCN) system (see fig. 5.1) which is situated physically at the NASA Goddard Space Flight Center and is aptly maintained by Scott Barthelmy (Barthelmy et al., 1998) [1]. The GRB Coordinates Network (GCN) is composed of 2 parts.

[1]The GCN contact is: Scott Barthelmy scott@lheamail.gsfc.nasa.gov

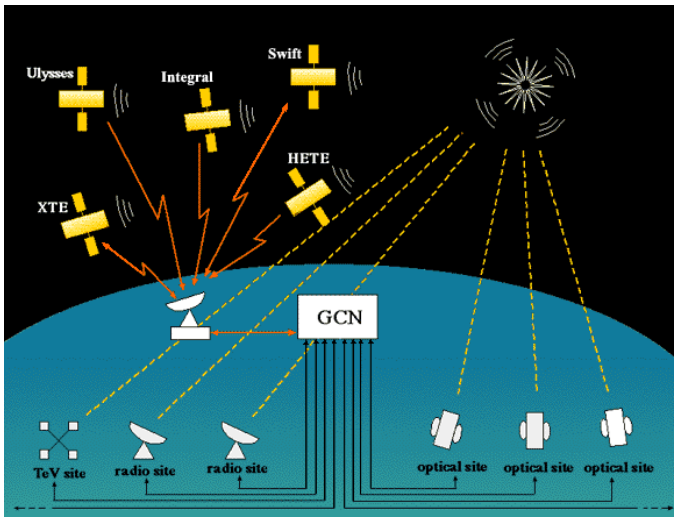

Figure 5.1: The physical GCN network.

I. The first part (Notices) distributes RA, Dec locations of GRBs detected by various instrument on spacecraft in real-time to ground-based and space-based follow-up observers. The Notices are simple email-based token-value style text messages and internet socket packets.

II. The second part (Circulars and Reports) consists of receiving from – and automatically distributing to – the GRB community prose-style e-mail messages about follow-up observations on various GRBs.

The Notices are the result of information received by GCN from the various spacecraft in real-time, processed into a standard format and automatically distributed to the those people wishing to receive specific Notices (based on a variety of filtering conditions). No humans are involved in the GCN portion of the sequence. This automation minimizes the time delay between when the γ-rays hit the instrument detectors and when the RA, Dec location information is available to the follow-up observers telescope. The token-value text style of the email form of the Notices is a compromise that allows both human reading and computer program parsing. The binary socket packet format and distribution method is **the fastest way to get the information to robotic telescopes.**

The figure 5.2 shows the fastest ultraviolet, optical and infrared observations obtained by the ground-based robotic telescopes and UVOT/Swift–satellite telescope after having received the GRB Coordinates Network alert (within one minute

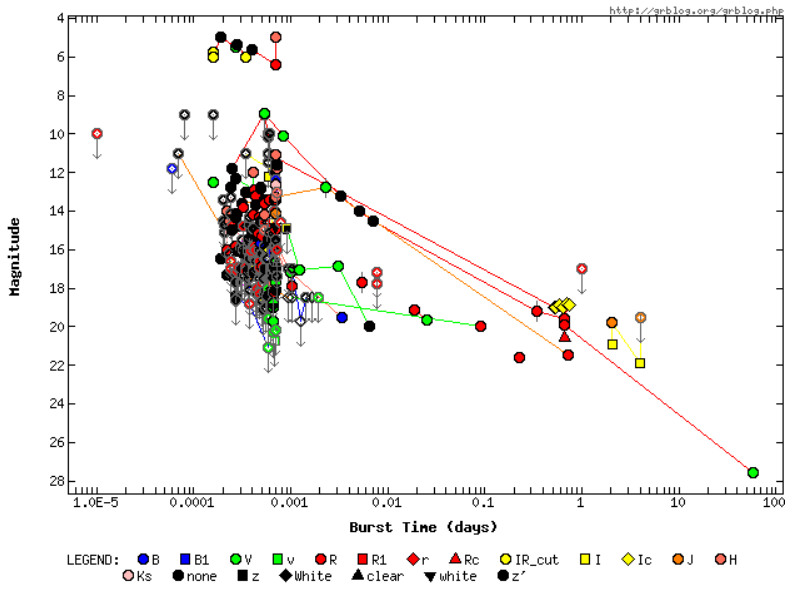

Figure 5.2: The fastest ultraviolet, optical and infrared observations obtained by the ground-based robotic telescopes and UVOT/Swift–satellite telescope after having received the GRB Coordinates Network alert. (within one minute from the explosion)

from the explosion). The total sample consists of 43 GRB afterglow light curves [2].

Systematically the regions close to the trigger range can never be sampled and a new research strategy is requires, e.g., independent activity monitoring by satellite surveys and by the alert system of the Gamma ray bursts Coordinates Network.

5.2 Optical Monitoring System & TORTORA Project.

To study short stochastic optical flares of different objects (GRBs, SNs, etc) of unknown localizations it is necessary to monitor large regions of sky with high time resolution (Piccioni et al., 1993). We have developed a system which consists of wide-field camera (FOV is 400-600 sq.deg.) using TV-CCD with time resolution of 0.13 sec to record and classify optical transients, and a fast robotic telescope aimed to perform their photometric investigation just after detection. Thus the two-telescope complex named *TORTOREM* combine the wide-field of view of the TORTORA camera and the precise and fast pointing of the robotic telescope REM

[2]http://grblog.org/grblog.php

(Molinari et al., 2006).

The systematic study of night sky variability on sub-second time scales still remains the important, but practically unsolved problem. This necessity for the search of non-stationary objects with unknown localization has been noted by Bondi (1970). Such studies have been performed (Schaefer, 1985), but due to technical limitations it has been possible either to reach high temporal resolution of tens of milliseconds in monitoring of $5'$ - $10'$ fields, or use 5 - 10 seconds time resolution in wider fields. The wide-field monitoring systems currently in operation, such as WIDGET (Tamagawa et al., 2005), RAPTOR (Borozdin et al., 2002), BOOTES (Castro-Tirado et al., 1999) and π of the Sky (Burd et al., 2005), while have good sky coverage and limiting magnitude, lacks the temporal resolution, which significantly lower their performance in study of transient events of sub-second duration (see table 5.1).

The optical transients of unknown localization may be very short. 30% of GRBs have the duration less than 2 seconds, and details of their light curves may be seen on time scales less than 1 ms (§1). Also, of great interest are the observations of very fast meteors which may be of extra-Solar System origin. To study the variability of large sky areas on such time scales, it has been proposed by Beskin et al. (1999) to use large low-quality mosaic mirrors of air Cerenkov telescopes. However, Karpov et al. (2005) and Zolotukhin et al. (2004) have demonstrated that it is possible to achieve the sub-second temporal resolution in reasonable wide field with small telescopes equipped with fast CCDs to perform fully automatic search and classification of fast optical transients. Moreover, the scheme of two-telescope complex (Karpov et al., 2004; Beskin et al., 2005a) able to study such transients in a very short time after detection has been proposed.

5.2.1 Design of wide-field cameras

The parameters of FAVOR prototype and TORTORA cameras in comparison with other wide-field monitoring systems currently in operation are presented in Table 5.1. The only cameras combining both wide field of view and high time resolution are the ones described here. Their technical characteristics are presented in Table 5.2, and images in fig. 5.3. Each camera consists of the main objective, the image intensifier used to downscale and amplify the image, transmission optics and the fast low-noise TV-CCD matrix (see fig.5.4). TORTORA camera also has

Figure 5.3: Images of prototype fast wide-field FAVOR camera -Special Astrophysical Observatory of Russia Academy of the Science, Russia and two-telescope complex TORTOREM -ESO La Silla Observatory, Chile.

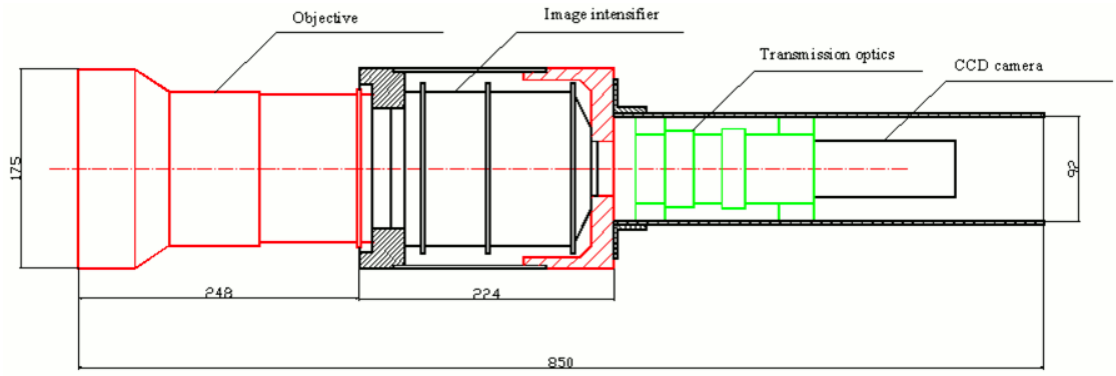

Figure 5.4: Schematic description of TORTORA system

the automatic focusing unit controlled through the PC parallel port interface. For FAVOR prototype, the focusing is performed by hands. TORTORA camera is installed on top of REM telescope, which has an alt-azimuthal mounting, while FAVOR has its own equatorial mounting.

The TV-CCD matrix of each camera operates in 7.5 frames per second regime with 0.128 s time exposure and gaps between frames negligibly small. The data from CCD is broadcasted through the gigabit local Ethernet network to the storage RAID array with 0.5 Tb capacity. The data flow rate for the system is about 20 Mb/s, and so the storage may keep the raw data only for one day, until next observational set. Also, the raw data are transmitted to the real-time processing

Table 5.1: Wide-field monitoring cameras currently in operation. For FAVOR and TORTORA the limits correspond to 3σ detection on a single frame, and differ from their real-time operational values.

Name	Field of View (degrees)	Time Resolution (seconds)	Limit
WIDGET	62 x 62	5	10^{m}
RAPTOR A/B	40 x 40	60	12^{m}
RAPTOR Q	180 x 180	10	10^{m}
BOOTES	16 x 11	30	12^{m}
π of the Sky	33 x 33	10	11.5^{m}
MASTER-VWF	20 x 21	5	11.5^{m}
Yatsugatake Camera	85 x 70	8	5^{m}
FAVOR	16 x 24	0.13	11.5^{m}
TORTORA	24 x 32	0.13	10.5^{m}

Table 5.2: Technical parameters of FAVOR and TORTORA cameras

	FAVOR	TORTORA
	Main objective	
Diameter	150 mm lens	120 mm mirror
Focal length	180 mm	150 mm
Focal ratio	1/1.2	1/1.2
	Image intensifier	
Photocathode	S20	S20
Diameter	90 mm	90 mm
Gain	150	150
Scaling factor	5.5	5.5
Quantum efficiency	10%	10%
	CCD matrix	
Model	VS-CTT285-2001	VS-CTT285-2001
Frame size	1388 x 1036	1388 x 1036
Pixel scale	$50''$/pix	$81''$/pix
Exposure	0.13 s	0.13 s
Pixel size	6.5 mum	6.5 mum
Read-out noise	6 e^{-}/pix	6 e^{-}/pix
Star FWHM	$3.1'$	$2.7'$
Mount	equatorial	alt-azimuthal
Focus	manual	automatic

PC operating the custom pipeline software under Linux OS. The pipeline performs the detection and classification of transient events of various types, and tries to recognize already known objects, by comparing the time and position of each events with catalogues of satellites and with star catalogue to minimize the number of false events due to stellar scintillations under bad weather conditions. Also, there are some other software subsystems, the most important is the controller ("BEHOLDER") process handling the interaction of wide-field camera with robotic telescope and initializing the auto-focusing process in the beginning of each observational night, and the compression of pieces of raw data related to detected events after the night. The overall scheme of all the software subsystems are shown in Fig. 5.5.

5.2.2 Software Description

The observational data is transmitted to the local PC which broadcasts them through the LAN to the storage computer equipped with a RAID array and to the PC for real-time processing. The software is installed at the three PCs and operated by WINDOWS and LINUX OSes. In order to process in real time the 13 Mb/sec data stream from the camera, one cannot use any standard reduction routines usually applied for photometry and source extraction. For this reason special software for the detection and investigation of OTs has been created. The software is installed on three PCs operated under WINDOWS and LINUX. The incoming information is a sample of 1388 $\times$ 1036 pixel CCD frames with an exposure time of 0.13 sec. The software performs the following tasks.

- Data transfer in real time from TV-CCD to LAN.
- Accumulation of initial data with volume up to 0.5 Tb per night on the RAID array.
- Data reduction in real time - detection and classification of OTs, determination of their equatorial coordinates and magnitudes, their possible identification with known objects, and the transfer of information about OTs (alerts) to the local and global networks.

The OT detection algorithm is based on the comparison of the current frame with one averaged over the 10-100 previous frames and consists of the following steps:

I. Extraction from the current frame of all pixels with intensity deviating from the mean by a given fraction of the RMS noise.

II. Location of any continuous regions of such pixels on the frame and determination of their parameters - coordinates and fluxes. All these regions are considered as optical transients (OTs) if observed on at least 3 successive frames.

III. Analysis of the OTs' shape (on a single frame) and motion (on three successive frames), their classification as meteors, satellites, or stationary transients, and determination of their parameters (trajectory, light curve, etc.).

IV. For the two latter cases - comparison of object parameters with known objects from star and satellite catalogs.

V. For stationary transients with an absence of catalog identifications, information on their parameters are sent to robotic telescopes or global networks. Thus, any transient may be classified if it is seen on at least 3 successive frames (in 0.4 sec).

5.2.3 Detection methodology

Due to very high data flow from the camera, it is impossible to use standard image reduction packages, as reported in the §5.2.2 so we have developed a fast transient detection algorithm based on the "differential imaging" method, which implies statistical analysis of temporal behaviour of each pixel over $N = 100$ previous frames, i.e. 13 seconds. The current value of the pixel I is being compared with the running mean $< I >= \sum I/N$ and standard deviation $\sigma_I = \sqrt{(\sum I^2 - (\sum I)^2)/(N-1)}$, and the significance of excess over the mean is computed as $A = (I - < I >)/\sigma_I$. Then, all the pixels with deviations over the mean of 3σ and greater are clustered into extended objects. Some objects, like single-pixel ones, are filtered out as they are most likely due to noise.

The response of such analysis to the long transient is highly non-linear, as the transient itself spoils the statistical properties of the image. It may be easily shown that the observed deviation A from the mean over the last N frames, when n of

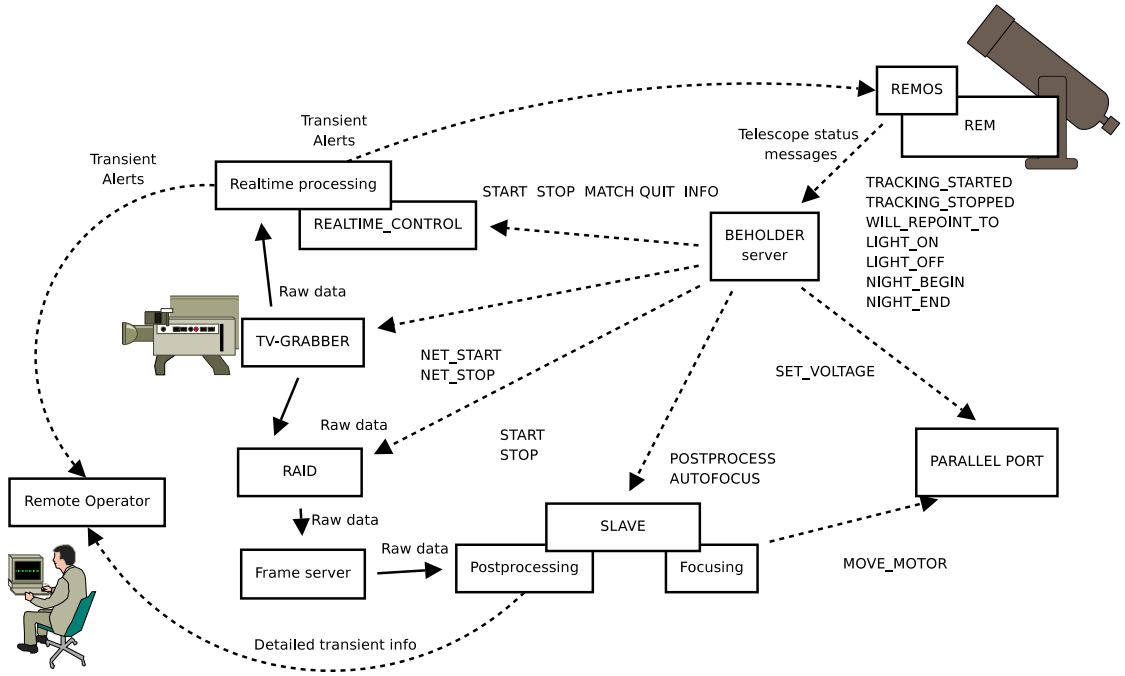

Figure 5.5: Schematic view of interoperation of various TORTORA subsystems with REM telescope.

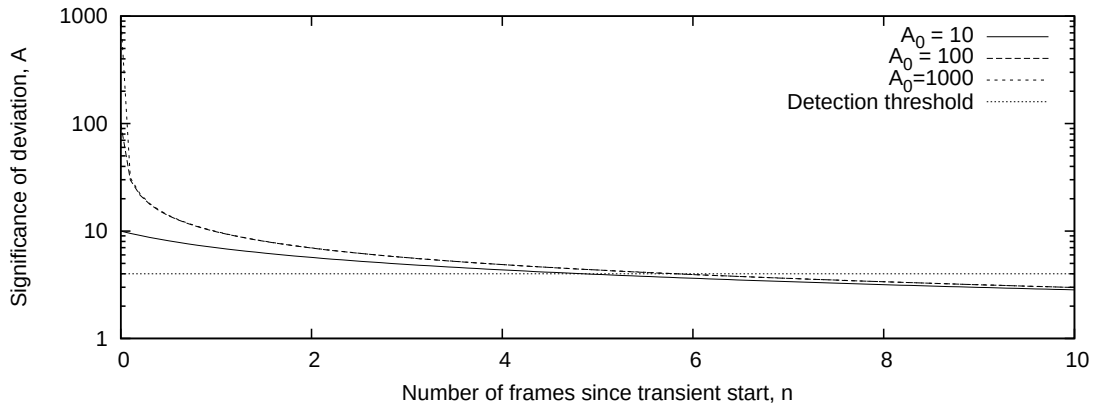

Figure 5.6: Response of the differential imaging method to the transient event of a given amplitude A_0 (in background noise units) as a function of time since its appearance (in number of frames).

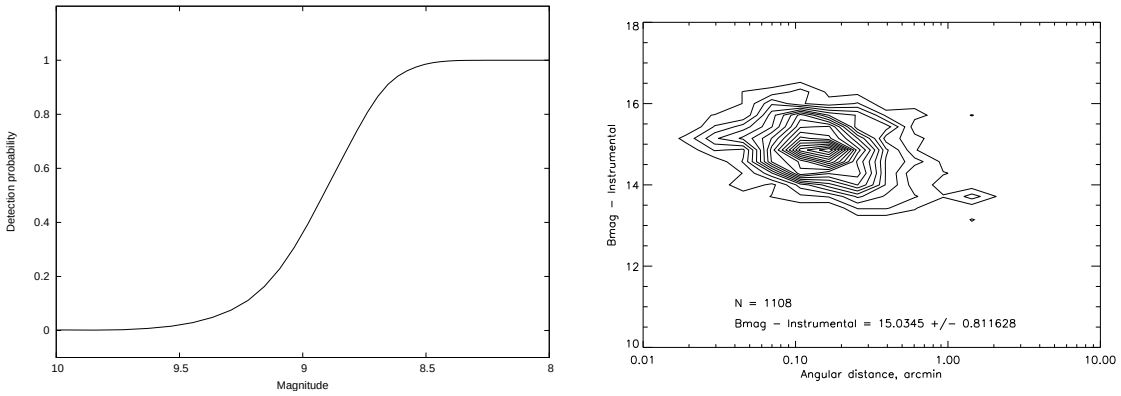

Figure 5.7: Left panel – the probability of detection of transient event of a given peak magnitude by differential imaging method for the TORTORA camera. Right panel – the distribution of spatial uncertainty of position determination versus photometric calibration coefficient for the TORTORA camera. The photometric uncertainty is mainly due to large vignetting towards the edges of the frame.

them are spoiled by the transient with A_0 flux, is

$$A = A_0 \frac{N-n}{\sqrt{N^2 + A_0^2 \frac{nN(N-n)}{N-1}}} \tag{5.1}$$

(where we neglected for simplicity the dependence of the image dispersion on its mean value). This function is shown in Fig. 5.6. It is clear that after roughly 5 frames arbitrarily bright transient is no more detected by the differential imaging, and so the real-time detection software has to extract all possible information on it during this time, i.e. in approximately half a second.

So, after the extraction of objects from current frame, the reduction pipeline compares their positions with trajectories of transients seen on previous ones (all objects here are assumed to be moving, but some of them – with zero velocity). Detection of object on three successive frames (in half a second) is enough to classify it into one of three possible classes – *noise*, if the object disappears, moving event, if it has statistically significant motion, or stationary transient. The case of slowly moving geostationary satellites is handled by comparing of event position with regularly updated satellite catalogue [3]

Detection of meteors, however, requires a different approach, as most of them may be seen on single or two successive frames only. Also, their motion are

[3] American department of defense satellite ephemerides database, available at: http://www.spacetrack.org

significantly faster than one of satellites. So, the meteors are selected by geometric length and flux criteria only. The detection efficiency of differential imaging method can be studied only numerically, as it does not see constant objects like stars. Results of numerical simulation on probability of object detection for typical TORTORA camera FWHM is presented in Fig. 5.7. The astrometric and photometric calibration is performed regularly (once per minute in a case of TORTORA camera, as it has an alt-azimuthal mounting with rotating field of view) by means of additional SExtractor (Bertin & Arnouts 1996) -based pipe-line and custom WCS matching code. The typical distribution of positional and flux errors are presented in Fig. 5.7. So, the pipeline is able to detect and classify any bright optical transient in a 0.4 second (3 frames) since its onset, before it hides from differential imaging algorithm. Example of such short flare is presented in Fig. 5.8. Then, the information on the event may be sent to the robotic telescope to perform its detailed investigation. Also, all the relevant information on the transient, including its light curve, trajectory and pieces of raw images containing it, is stored for the subsequent off-line investigation and statistical analysis.

5.2.4 Installation on the top of the REM telescope

At the begining of the May 2006 TORTORA was installed in the dome of the REM telescope located at Eso-La Silla (Chile) and successfully achieves its First Light. The TORTORA's first light images were taken on 12 May 2006. The camera is coaxially mounted to the REM telescope and a counterweight of 40 kilograms is added to the mount of the robotic telescope in order to balance its structure (see figure 5.11). No significant decrease in the speed of the REM telescope has been registered after the addition of the weight.

It was also verified that the operation of TORTORA camera has no effect on other REM devices such as REMIR and ROSS instruments (Calzoletti et al., 2005). TORTORA is completed automatically and remotely controlled and it use the weather station of REM dome. Until now he has collected $\sim$ 150 nights of observations[4]. The TORTOREM-complex has a graphical user interface available

[4]data are available under request.

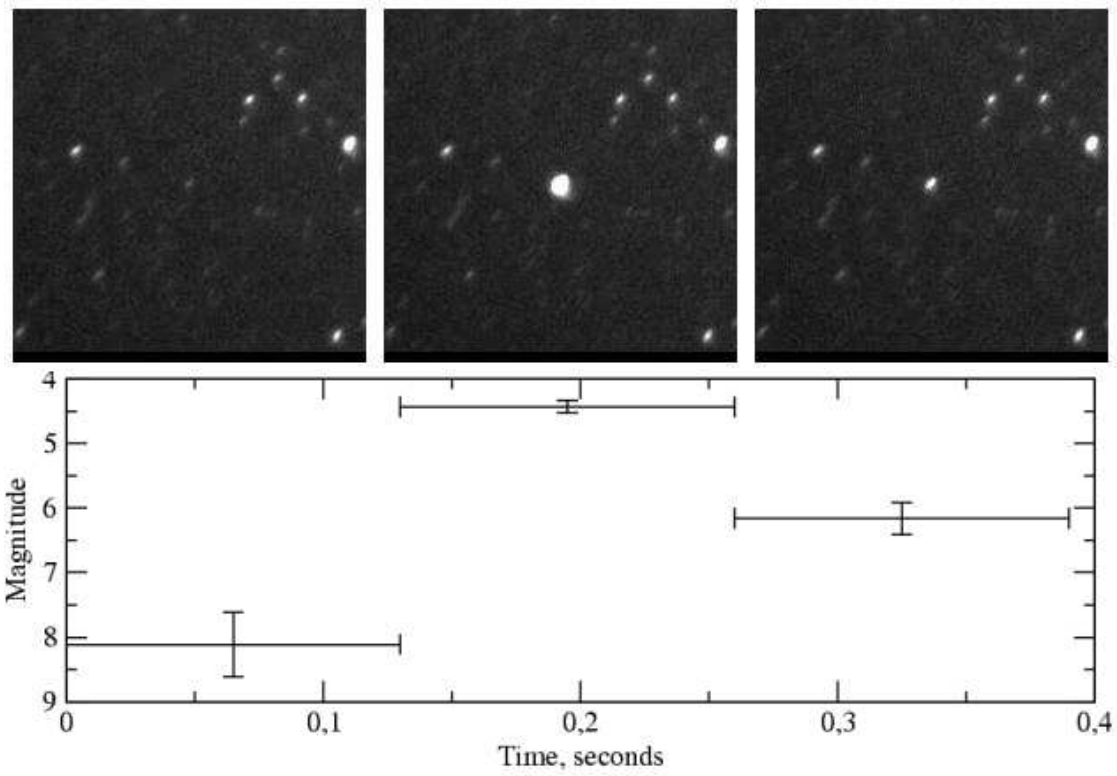

Figure 5.8: Example of a short satellite flare detected by the camera. Total length of the event is 0.4 sec (seen on 3 successive frames).

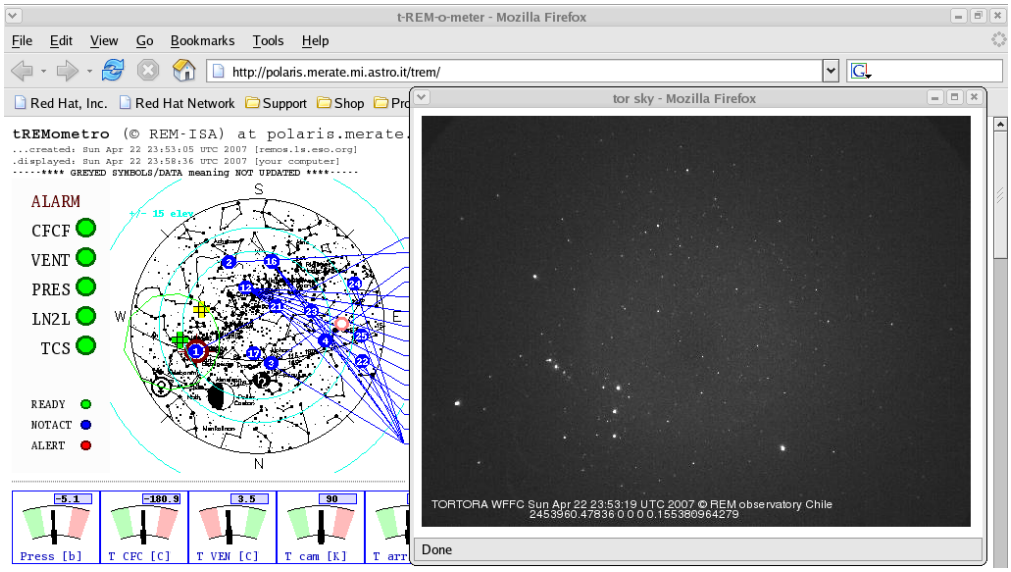

Figure 5.9: Public graphical user interface of TORTOREM system. Information about the run of the observations and the photometric conditions during the night are available in real time.

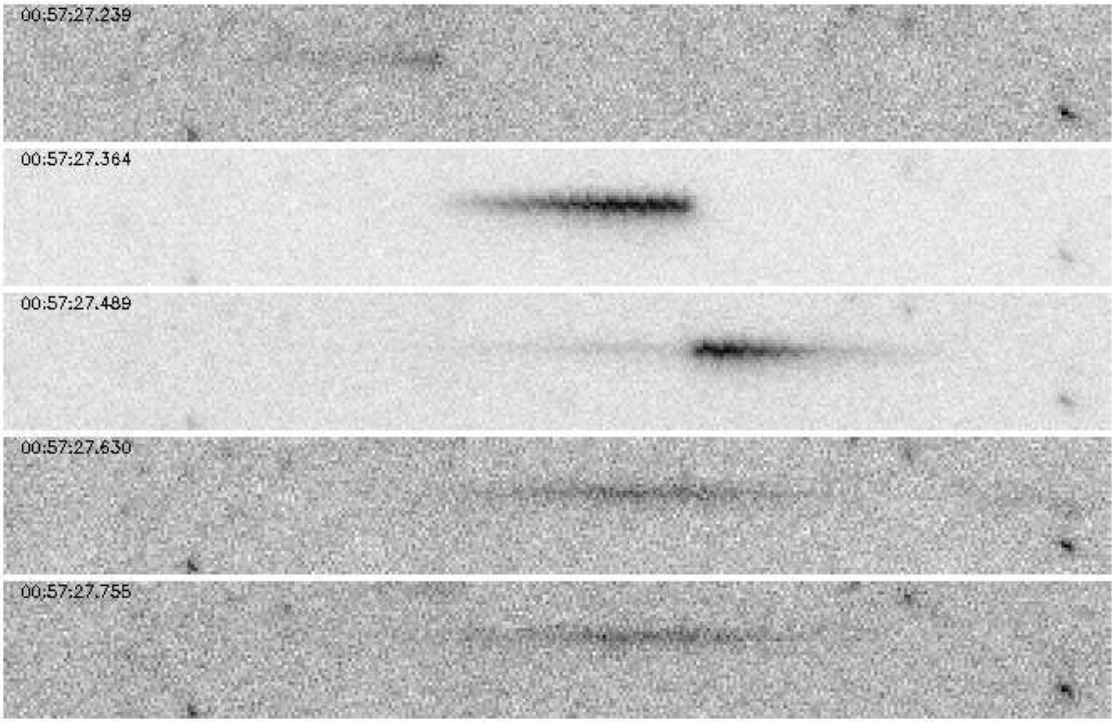

Figure 5.10: Example of a fast (approx. 0.3 seconds) and bright ($V_{peak} \approx 3$)meteor detected by the camera. Sub-frame brightness variations, as well as long-lasting tail, are clearly seen.

online. [5] Public information about the run of the observations and the photometric conditions during the night are available in real time.

5.3 Results

FAVOR camera operates in monitoring regime since June 2003, since December 2006 it follows up the center of Swift field of view. TORTORA camera operates since June 2006, approximately half of observational time (when REM is not performing its scheduled programme) it follows up Swift of view too. The back-reaction mode of TORTOREM is now in testing stage.

For each observational night, the cameras detect approximately 300 meteors and 150 satellites of various brightness. Example of a fast (0.3s) and bright ($V_{peak} \approx 3$) meteor is shown in Fig. 5.10.

[5] http://polaris.merate.mi.astro.it/trem/

5.3.1 Follow-up observations of γ-Ray Bursts

Due to REM telescope operation in trigger regime, TORTORA camera has been able to observe the regions of localization of three γ-ray bursts in a short time since the event (Guarnieri et al., 2006; Karpov et al., 2006a; Karpov et al., 2006b; Karpov et al., 2006b).

The field of GRB 060719 was observed by the camera 59 s after trigger. The summation of 100 frames with 12.8 s. effective exposure did not reveal any source down to the B = 12.4 min . We performed the Fourier analysis of 15 min data set (6750 successive frames) to search for the periodic signal at the GRB position. The upper limit for the amplitude of sinusoidal variability (i.e. the mean brightness of the sinusoidally-variable object) is B = 15.3 min over the 0.01–3.5 Hz range in PSF–sized region of the image.

GRB 061218 was initially outside the camera field of view. The system was repointed and the TORTORA began to acquire 118 sec after trigger with 7.5 Hz frame frequency (0.128 s exposure). The summation of 100 frames with 12.8 s. effective exposure did not reveal any source down to the B = 11.3 mag (3-sigma). We performed the Fourier analysis of 23 min data set (10000 successive frames) to search for the periodic signal at the GRB position. The upper limit for the amplitude of sinusoidal variability is B=16.4 (3-sigma) over the 0.01–3.5 Hz range.

Similarly the field of GRB 061202 was observed 92 sec after trigger The summation of 100 frames with 12.8 s. effective exposure did not reveal any source down to the B = 11.3 mag (3-sigma) on bright sky background. The upper limit for the amplitude of sinusoidal variability (Fourier analysis of 10 min data) is B=14.0 (1-sigma) over the 0.1–3.5 Hz range. Also, FAVOR camera observed the error box of GRB 070704A, detected by Swift, for 40 seconds before and at the time of satellite trigger. Unfortunately, according to following analysis of Swift data (Sakamoto et al., 2007), the actual burst occurred 25 seconds before our observations started (Karpov et al., 2007). The integral data on all these follow-up observations are presented in Table 5.3. Stationary flux limits have been derived from 100-frame average images (12.8 s effective exposure).

Table 5.3: Upper limits on the constant flux and sinusoidal variability of gamma-ray bursts, observed with TORTORA and FAVOR (last burst) wide-field cameras in trigger regime.

Burst	Time since event (seconds)	12 s limit (100 frames)	Variab. timescale (Hz)	Variab. limit
GRB060719	59	12.4	0.01 – 3.5	15.3^{m}
GRB061202	92	11.3	0.1 – 3.5	14.0^{m}
GRB060719	118	11.3	0.01 – 3.5	16.4^{m}
GRB060719	25	13.0	–	–

5.3.2 Untriggered search for prompt emission

One of the important result of our routine observations is the estimation of the rate of the orphan transients. These hypothetical objects are called orphan afterglows, since they are not associated with any known GRBs.

Since may 2006 we accumulated approximately 150 nigh of observations in $24deg \times 32deg = 768deg^2$ field up to 10.5 unfiltered magnitude with 0.13 sec temporal resolution. Untriggered search of optical afterglow taken by ROTSE team (Rykoff et al., 2005) provided upper limit of GRB orphan afterglow rate of $1.1 \times 10^{-8} s^{-1} deg^{-2}$. Our data in terms of aggregate time and field of view provides 12 times more strict constraint on the object of search rate. ROTSE search was oriented on afterglow emission (they used 80 sec exposure which undoubtedly smoothes bright short peaks of prompt emission as mentioned above) while we perform search of much shorter events (to be accurate, much shorter phase of the same event) with brighter limiting magnitude. Thus we can state that prompt optical transients rate is less then $7.7 \times 10^{-9} deg^{-2} sec^{-1}$ for transients that are brighter then 10.5^m on 0.13 s timescale during at least of 3 successive frames (0.4 sec). Usage of average frames sequence processing allows to strict this photometrical constraint even more.

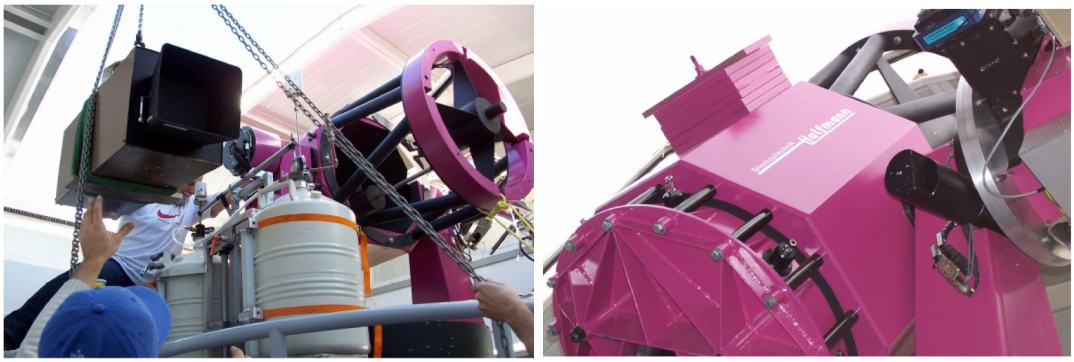

Figure 5.11: The camera is mounted coaxially with the REM telescope and a counterweight of 40 kilograms is added to the mount of REM in order to balance its structure. The TORTORA's first light images were taken on 12 May 2006.

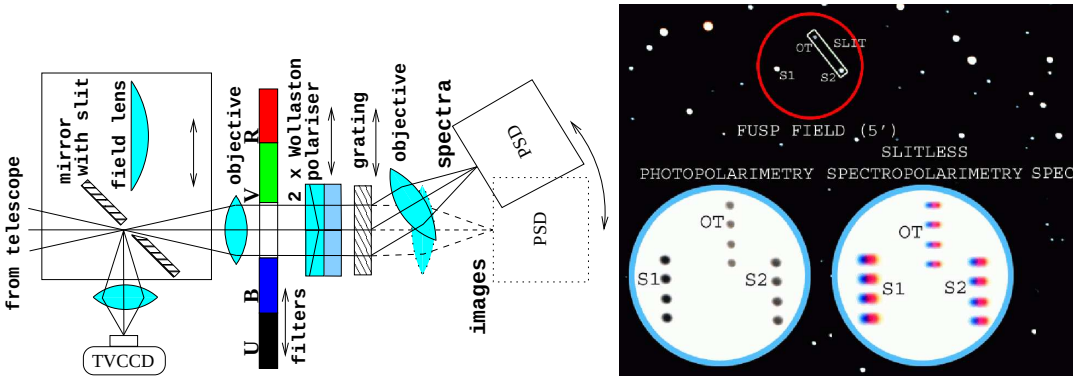

Figure 5.12: Fast universal spectrophotopolarimeter (FUSP) principal scheme (left panel) and sketch of its field of view in various modes (right panel)

5.4 Perspectives

It is important to develop the methodology of wide-field search for fast optical transients in two directions. The first is the increase of detection threshold by 2-3 magnitudes while keeping the field of view and temporal resolution. It may be achieved by means of multi-objective (or multi-telescope) systems, by decreasing field of view of single instrument and, therefore, its pixel scale. To avoid the dominance of CCD read-out noise, the quantum efficiency and amplification of image intensifier have to be increased. Another direction is the usage of instruments equipped with dispersive (or polarizing) equipment to record slitless spectra (in polarimetric mode – at least three per object) of each object in the field. Intermediate variant is possible, too. The robotic telescope carrying the fast wide field camera may be equipped with universal photospectropolarimeter (FUSP) with

high time resolution (see Fig. 5.12) able to perform detailed study of spectroscopic and polarimetric properties of 13^{m}-14^{m} transient in several seconds (Beskin et al., 2005b).

Chapter 6

TORTORA Discovery of naked Eye Burst fast optical variability.

"...sic igitur solem lunam stellasque putandum ex alio atque alio lucem iactare subortu et primum quicquid flammarum perdere semper, inviolabilia haec ne credas forte vigere."

De Rerum Natura-Libro V-

In this chapter we present the complete high temporal resolution photometry (0.13 sec effective exposure) of the prompt optical emission occurred in GRB 080319B captured with TORTORA wide-field optical camera mounted on REM robotic 60–cm telescope located at ESO–La Silla (Chile) (§5). Due to the peculiarity of the prompt optical emission of this burst and its importance for obtaining information on physics of the central engine, the analysis of the time variability are discussed with great details using different statistical tools.

6.1 Introduction to the phenomenon and its implications

6.1.1 Prompt Optical Emission

Over the past nine years the prompt optical emission contemporaneous with the γ-ray-active phase of a GRB have became subject of exciting debate in astronomy community; the brevity of these phenomena and their fleeting nature makes them elusive and difficult to study. Due the relative short duration of the prompt γ-ray emission (T $\sim$ 0.5-100 sec) simultaneous follow-up observations at optical wavelengths suffered the lacked of rapid and precise burst localizations. GRB 990123 was the first event for which optical emission was detected during the burst phase (Akerlof et al., 1999).

Nowadays the fast and accuracy localization of GRBs by Swift mission (Gehrels, 2004) and its capability to alert fast-slewing robotic telescopes [1] within few seconds after burst has allowed to significantly increase the numbers of the events that was observed optically during the bursting phase.

Although the prompt optical emission are usually not well sampled, in same cases the optical and γ-ray fluxes appear correlated e.g. GRB 041219A (Vestrand et al., 2005), GRB 051109A, GRB 051111 (Yost et al., 2007), GRB 060124 (Romano et al., 2006), GRB 060418 (Molinari et al., 2007), GRB 060526 (Dai et al., 2007), GRB 060607A (Ziaeepour et al.,2008), GRB 061007 (Mundell et al., 2007), GRB 070616 (Starling et al., 2007); instead in few events e.g. GRB 990123 (Akerlof et al., 1999) and GRB 060904B (Klotz et al., 2008) the structure of the γ–ray light curve and the locations of the optical flashes appear anticorrelated.

Li & Waxman (2008) point out that the apparent simultaneity of γ-ray and optical emission is due to the highly relativistic speed of the plasma expansion suggesting that the time delay between γ-ray and optical fluxes is expected to be shorter than one second, too brief to be identified by current optical detections that usually have lower temporal resolution.

The naked eye GRB 080319B sheds new light on the on the physical mechanism involved during the stellar black hole formation. For the first time, joining the unprecedented high TORTORA temporal resolution analysis to the high-energy mea-

[1] see http://www.uni-sw.gwdg.de/ hessman/MONET/links.html for a recent census of robotic telescopes in the world

surements obtained from satellite programs (SWIFT/BAT and KONUS/WIND), we are able to analyze the different physical components responsible for the prompt-emission using a comparable sampling-time from higher to lower energy.

6.2 Data Reduction and analysis

6.2.1 Observations

On 2008 March 19 at 06:12:49 UT (hereafter t_0) the Swift Burst Alert telescope triggered on and located GRB 080319B (trigger = 306757; Racusin et al., 2008) with a ∼3' radius error box. The bright burst was simultaneously detected by Konus-Wind (KW) satellite (Golenetskii et al., 2008) yielding the burst fluence of 6.13 ± 0.13 × 10^{-4} erg cm^{-2}. Assuming z = 0.937 (Vreeswijk et al., 2008) and standard cosmology model (H_0 = 70 Km/s/Mpc, Ω_M= 0.3 and Ω_Λ=0.7) the isotropic energy release is $E_{iso} = 1.32 \times 10^{54}$.

The γ–ray light curve showed a complex structure with several separated pulses above 70 keV and a generally smoother behaviour at lower energies.

The X-Ray Telescope began observing the burst location at 06: 13: 49.7 UT, ∼60.5 seconds after the BAT trigger finding a very bright fading and uncatalogued X-ray source at the position: RA(J2000) = 14h:31m:40.7 s, DEC(J2000) = 36d:18':14.7". The X-ray afterglow can be fit by a triple broken power-law with initial decay slope of 1.54 ± 0.01, breaking at 2790 ± 664 s to a slope of 1.85 ± 0.05, breaking again at 41.4 ±9 .0 ks to a slope of 1.17 ± 0.06, and finally breaking at 1.04 ± 0.43 Ms to a slope of 2.9 ± 2.3. (Racusin et al., 2008). The UV/Optical Telescope took a finding chart exposure of 400 sec with the V filter starting ∼ 175 seconds after the BAT trigger.

Near detection limit the late-time UVOT white filter observations are also suggestive of a break at approximately the same time as the X-ray break (Racusin et al., 2008).

The field of the GRB 080319B was imaged before the GRB event by three independently ground-based optical sky monitoring. No optical pre-cursors were detected in TORTORA (Karpov et al., 2008), Pi of the Sky (Cwiok et al., 2008) and RAPTOR (Wozniak et al., 2008) surveys with observations starting 27 minutes, 16 seconds and 90 minutes before the Swift-BAT trigger, respectively.

In RAPTOR and Pi of the sky the first image with detectable optical emission

(exposure time 10 and 5 seconds respectively) started $\sim$ 2 seconds after the BAT trigger when the optical counterpart became brighter than V $\sim$ 12.

In TORTORA high temporal resolution dataset (0.13 sec exposure time) the first frame in which we detected the optical flux started $\sim$ 9 seconds after the BAT trigger when the source became brighter than V $\sim$ 12.

The bright visual peaks occurred during the the prompt γ-ray emission have reached 5.3 magnitude approximately, this made it visible with naked eye in BOOTES constellation [2] for $\sim$ 40 seconds, assuming an observer in a dark location. Many other facilities quickly observed the bright optical emission after few minutes by its explosion after having received the rapid localization by Swift-alert e.g . REM (Covino et al. 2008), ROTSE-IIIb (Swan et al. 2008), PROMPT (Schubel et al., 2008), PAIRITEL (Bloom et al., 2008), VLT/UVES (D'Elia et al., 2008) producing the better data collection never before obtained up to now for a cosmological transient phenomenon in the universe.

6.2.2 Photometric Condition

For TORTORA system, observational conditions at a time of γ–trigger had been suboptimal. The burst occurred at $Z \approx 68^{\circ}$, the sky was bright due to nearly full moon, and the large part of camera field of view had been covered by the REM dome, with some in-dome light pollution present. Due to these reasons the automatic data processing pipeline had been turned off, but all imaged data had been stored in RAID array.

Since 05:46:22 UT REM telescope observed the box of previous burst, GRB080319A. At 06:12:49 UT, Naked-Eye Burst, GRB080319B, flashed at $\sim$10 degrees from the former, near the edge of TORTORA field of view. At 06:13:13 UT, REM started automatic repointing, and since 06:13:20 UT the burst location stayed at the center of camera field of view. Figure 6.1 shows the sample 2.5 $\times$ 2.5 degrees images centered at burst position for its different phases.

TORTORA limiting magnitude in that conditions had been significantly lower than ones of "Pi of the Sky" and RAPTOR, but its superior time resolution allowed to trace the burst time structure with unprecedented level of details (see Fig. 6.2 for summary light curves of TORTORA, "Pi of the Sky" and Swift BAT).

The values of the effective air mass at middle time exposure and the seeing as

[2] http://grb.sonoma.edu/

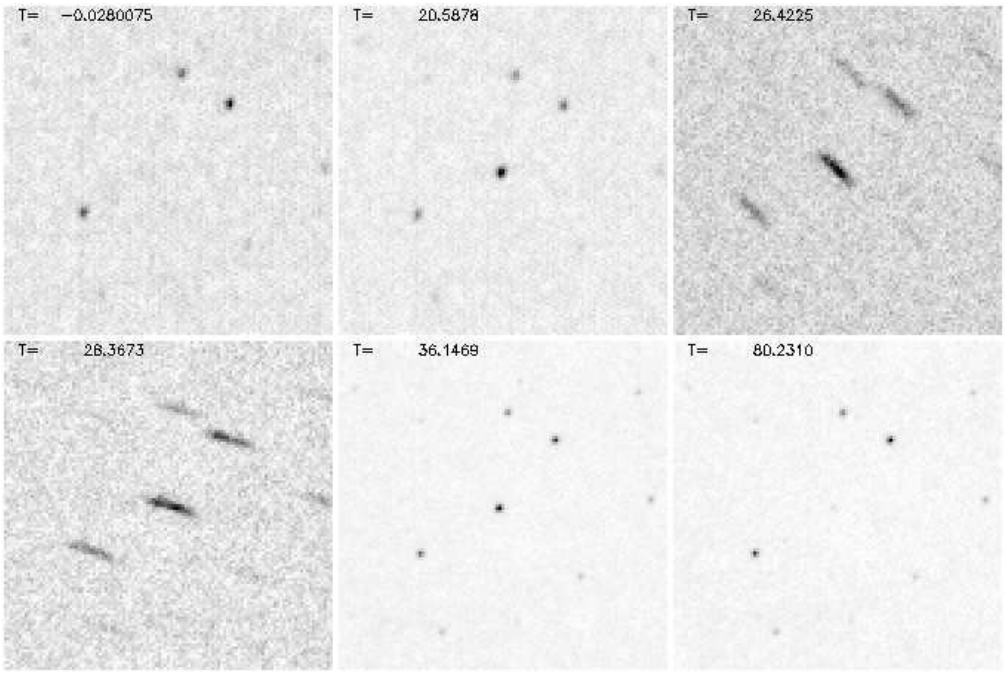

Figure 6.1: Sample images (10–frames averaged) of GRB080319B as seen by TORTORA. The trigger ($T = 0$), first peak ($T = 20.5$), two repointing ($T = 26.4$ and $T = 28.4$), last peak ($T = 36$) and early afterglow tail ($T = 80$) moments are shown. Image size is 2.5 × 2.5 degrees.

measured by La Silla–Meteo Monitor [3] were estimated ~ 2.61 and ~ 0.9" respectively. According to Schlegel et al. (1998) Galactic extinction is E(B-V) = 0.011 mag thus implying (assuming Rv=3.1) $A_B = 0.048$, $A_V = 0.036$, $A_R = 0.029$.

6.2.3 Prompt Optical Data

The TORTORA fast wide-field camera began taking data on the field of GRB 080319B at 05:46:22 UT ($t_0 = 27$ minutes before trigger) until to 06:15:41.00 ($t_0 = 188$ sec after trigger) collecting ~ 14000 unfiltered images with an effective exposure time of 0.13 seconds without temporal gap between two consecutive frames. From 23 sec up to 30 sec after the burst, the REM-telescope was slewing to the location of GRB 080319B after the alert message disseminated through the GCN notices by Swift-BAT instrument. The raw images stored in RAID has been processed at a day time by a pipeline including TV-CCD noise subtraction, flat-fielding to compensate vignetting due to objective design, and custom aperture photometry

[3] www.ls.eso.org/lasilla/dimm/

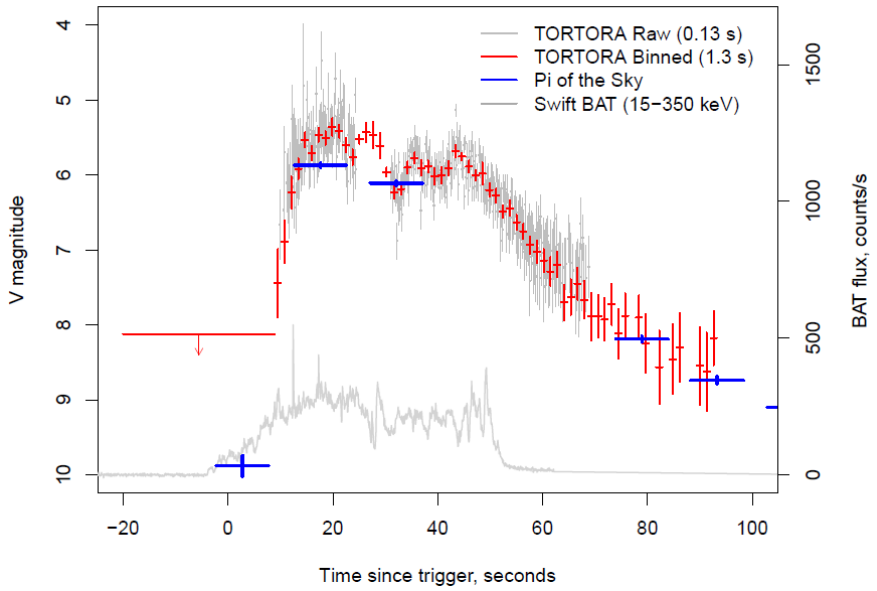

Figure 6.2: The light curve of GRB080319B acquired by TORTORA wide-field camera (upper curve, left axis) alongside with Swift BAT γ-ray one (lower curve, right axis). Also, transient brightness measurements by Pi of the Sky optical camera (1) are shown. Swift- BAT light curve is a sum of all four energy channels. TORTORA data points show both full resolution (original data frames) and low-resolution (10 images co-added). Full-resolution data are unavailable for a period of REM telescope repointing due to massive blurring of object image. Only data points with errors less than the value are shown.

code taking into account non-poissonian and non-ergodic pixel statistics caused by image intensifier (§5.3). Circular aperture photometry was performed with `PHOT/DAOPHOT` function in `IRAF`[4]. The optimal size radius of aperture was chosen to be 3.5 pixels after experiments with growth curves and the background sky annulus and dannulus were set at 10 pixels and 7 pixels, respectively. This optimal aperture size, which produces the smallest photometric errors, contained also the spatially varying PSF due to geometric distortions present in the final images.

Independent check to calculate optimized aperture photometry in order to obtain the light curve of GRB 080319B with the lowest possible noise, was also performed using `apcalc` routine within the `VAPHOT` package [5]. Corrections for the amount of missing flux from the source outside this sized aperture were made using a correction factor estimated from the growth-curve method (Stetson, 1990) implemented under `IRAF` task `mkapfile`, yielding aperture corrections typically of

[4]IRAF: Image Reduction and Analysis Facility, http://iraf.noao.edu/
[5]http://www.iac.es/galeria/hdeeg/pubs2000/photproc.pdf

order 0.008 mag.

A weighted mean of all comparison objects was calculated to produce a single comparison magnitude for each frame. To construct the light curve (fig. 6.3), differential magnitudes of the form $dm = m_{comp} - m_{OT}$ were calculated. Independent check for variability in the differential light curve was also produced using ISIS image subtraction package (Alard & Lupton 1998). Finally the photometry performed in instrumental system was calibrated towards the V magnitudes of several nearby Tycho2 stars.

We have no data on afterglow color information for GRB 080319B at early time (to $<$ 60 sec). Thus, no additional color corrections for V-band equivalence have been applied to TORTORA unfiltered data.

For the REM repointing time interval fluxes have been derived using custom elliptic aperture photometry code after summation of 10 consecutive frames with compensated motion of the stars. Unfortunately, it seems impossible to reconstruct the light curve of this interval with any better resolution due to massive blurring of star PSF caused by their motion. For all other intervals, photometry has been performed both with 10-frames (1.3 s effective exposure) binning, and with original (0.13s) time resolution. As a results, we have one more peak with in the optical light. Log of optical measurements of GRB 080319B prompt optical emission with 1.3 sec time resolution is reported in table 6.7. No correction has been made for the expected extinction corresponding to E(B-V) of 0.011. The time of each bin is in the middle of the bin (seconds). [6]

6.3 Light Curve Structure

6.3.1 Fit models and Variability analysis

TORTORA was able to detect optical emission since approximately t_0 +10s. It has tracked a fast emission rise from t_0 +10s till t_0 +15s, followed by a complex evolution till t_0 +45s and a slow decay thereafter. The rise from V $\approx 7.5^m$ till V $\approx 5.5^m$ may be approximated by a $\sim t^4$ power-law originated at T $\approx$ 0; while γ–ray emission started earlier, at $t_0 \approx$ -4s.

The decay since t_0 +45s is also a $\sim t^{-4.6}$ power-law. The complex evolution since T+15s till T+45s consists of two regions of different mean intensity levels

[6] For the large amount of data, the full resolution data are available under request

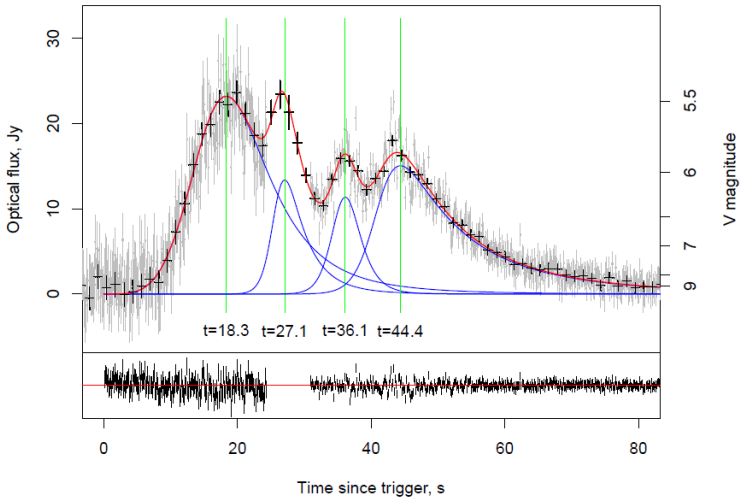

Figure 6.3: The light curve of GRB080319B acquired by TORTORA wide–field camera. The γ-emission started at T $\sim$ –4s and faded at T $\sim$ 55s. Full resolution (0.13s exposure, gray lines) data are available for all duration of γ-emission except for interval of REM telescope repointing (24s $<$ T $<$ 30s), while low-resolution ones (summation of 10 consecutive frames, 1.3 s effective exposure) – for the whole time. The light curve is approximated using Kocevski profile (see text). Four nearly equidistant flares are detected; lower panel shows the residuals of such approximation.

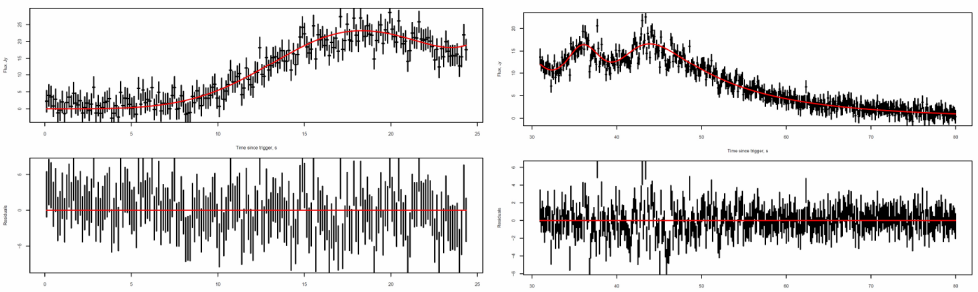

Figure 6.4: Zoom in figure 1.3. The TORTORA light curve is approximated using Kocevski profile (see text) before and after the REM repointing; lower panel shows the residuals of such approximation

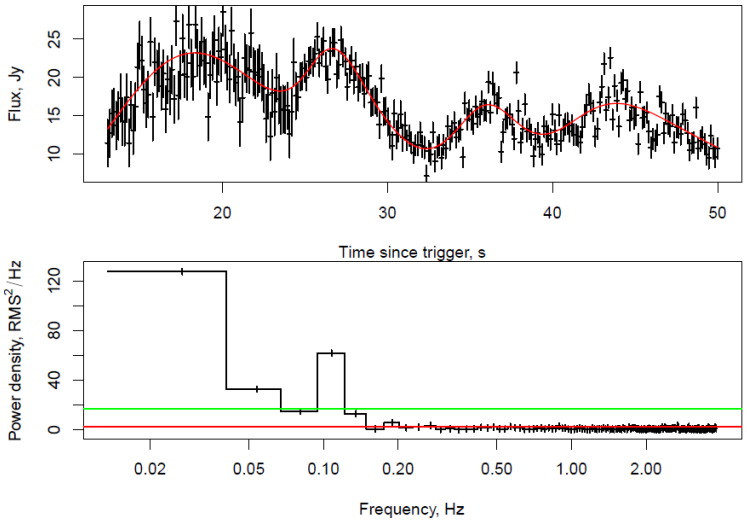

Figure 6.5: Power density spectrum of the plateau stage. The high resolution (0.13s) data for the missing second peak interval have been simulated by the white noise using the low-resolution (1.3 s) light curve. The feature at $\sim$ 9 s is clearly visible and is not a continuation of a low frequency red noise. Horizontal lines represent mean noise level and a level of noise deviations with 10^{-3} significance, estimated by bootstrapping the original data set.

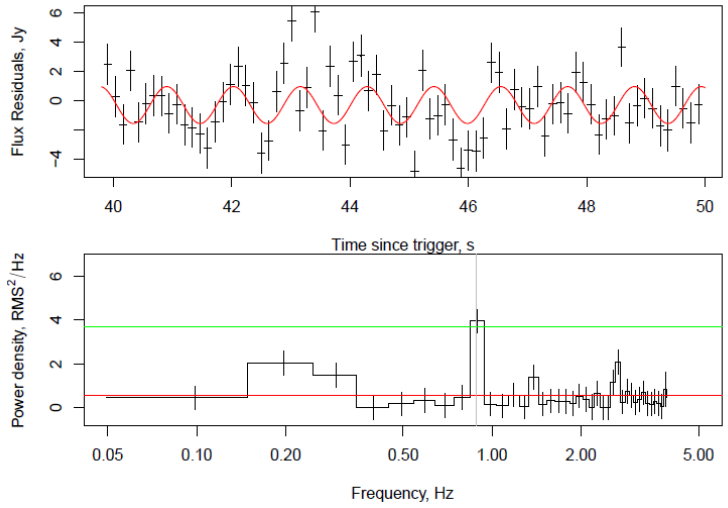

Figure 6.6: Power density spectrum of the last peak and the best fit sinusoidal approximation for the feature seen here. Horizontal lines represent mean noise estimated by bootstrapping the original data set.

F $\sim$ 20 Jy from T+15s till T+30s and F $\sim$ 13 Jy from T+30s till T+45s, which roughly correspond to two regions of γ-ray light curve (see fig. 6.9).

At the same time interval four peaks can clearly be seen in optical data with an inter-peak separation of $\sim$ 9 s. The Power density spectrum of the plateau stage (10s–50s) shows the feature at $\sim$ 9s and is not a continuation of a low frequency red noise. (see fig. 6.5) Horizontal lines represent the mean noise estimated by bootstrapping the original data set. We used the high resolution (0.13s) data and for the missing second peak interval (during REM repointing) have been simulated by the white noise using the low-resolution (1.3 s) light curve. The same result is obtained (without simulating the missing high time resolution data of the second peak interval) using the Lomb-Scargle periodogram algorithm (Scargle, 1982) suitable for time series with unevenly spaced X-values.

The well detected peaks are approximates with profile describe in Kocevski et al. (2003). (see figs. 6.3 and 6.4). The best-fit parameters for the decomposition of the light curve into 4 peaks with shape described by Kocevski profile are shown in table 6.1. Here, T_0 and F_0 are the peak maximum positions and fluxes, while r and d are the power–law indices of their rising and declining parts.

After we subtracted the smooth light curve which approximates these four peaks from the full-resolution data and performed Fourier analysis of residuals to look for short time scale variability. There is no evidence of any significant feature on the first continuous part (before REM repointing) of the light curve. The second part, however, show a features at $\nu \sim 0.9$ Hz with a significant level of 0.01, which seems to be localized around the last peak. No other intervals of transient light curve show similar features, nor do the comparison stars. The fig. 6.6 shows the Power Density Spectrum of the last peak and the best fit sinusoidal approximation for the periodic emission. Horizontal lines represent mean noise level estimated by bootstrapping the original data set.

6.3.2 Two Regions of Different Mean Intensity Level

As reported in the previous section, the complex evolution since t_0+15s till t_0+45s consists of two regions of different mean intensity levels which correspond to two regions of γ-ray light curve.

The BAT data are processed with the `heasoft` package (v.6.4) adopting the ground–refined coordinates provided by Swift team (Cummings et al., 2008). For

T_{peaks} and power–law indices		
T_{peak}	rising r	declining d
18.3 ± 0.3	4.0 ± 0.4	5.4 ± 4.1
27.0 ± 0.3	24.8 ± 8.3	9.7 ± 4.9
36.1 ± 0.2	25.9 ± 7.6	22.0 ± 17
44.4 ± 0.5	21.9 ± 3.3	5.1 ± 0.2

Table 6.1: Best–fit parameters for the decomposition of the light curve into 4 peaks with shape described by Kocevski profile, shown in Figs 6.3 and 6.4. Here, T_{peaks} is the peak maximum positions, while r and d are the power-law indices of their rising and declining parts

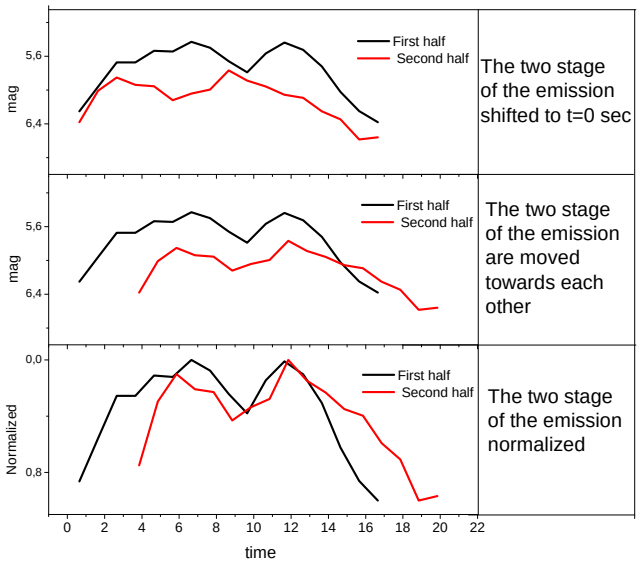

Figure 6.7: The two regions of the different mean intensity level, in black color the first part and in red color the second part. In the top panel the two equal parts are arbitrary shifted to a common time. In the middle panel the second stage of the emission is shifted ~ 3 sec along the time axis. The correlation coefficient after the 3 sec shift is ~ 0.8. The bottom panel show the two stage of the emission arbitrarily normalized to compare the morphological structures.

more details on the process of data reduction see §3.

For this reason, we divided the light curve into two equal parts, and computed the parameters, as the mean the variance, the standard deviation, the skewness and the kurtosis (listed in Table 6.1) and estimated the autocorrelation functions of the two halves. Since this is symmetric for real data, only the positive lags are plotted. We apply the bootstrap method for time series (block bootstrap method) [7] to derive estimates of standard errors. The algorithm generates bootstrap replicates of a statistic applied to a time series. The replicate time series can be generated using fixed or random block lengths or can be model based replicates. The results of the autocorrelation function are plotted in fig 6.8.

This intrinsic similarities in the temporal properties of the two halves of the light curve seems also to be reflected in the similarities of the autocorrelation functions. The rate at which the autocorrelation function decays to zero may be interpreted as a measure of the memory of the process and thus fig 6.8 indicates that the memory of the second part of the light curve is the same as the first part. The mean, the variance, the standard deviation and the autocorrelation function of the first and second half of the light curve do not show significant differences. Differences are found in the values of skewness and kurtosis. [8]

The fig. 6.7 shows the two regions of the different mean intensity level (in black color the first part and in red color the second part) in the prompt optical emission of GRB 080319B. In the top panel the two equal parts are arbitrary shifted to a common time. In the middle panel the second stage of the emission is shifted $\sim$ 3 sec along the time axis. The correlation coefficient after the 3 sec shift is ~ 0.8.

[7] Bootstrapping is the practice of estimating properties of an estimator (such as its variance) by measuring those properties when sampling from an approximating distribution. One standard choice for an approximating distribution is the empirical distribution of the observed data. In the case where a set of observations can be assumed to be from an independent and identically distributed population, this can be implemented by constructing a number of resamples of the observed dataset (and of equal size to the observed dataset), each of which is obtained by random sampling with replacement from the original dataset. In general in all the GRB light curves the measurements are not independent but correlated so block bootstrap methods are required.

[8] In many statistical analyzes a characterization of the dataset includes skewness and kurtosis. Skewness is a measure of symmetry, or more precisely, the lack of symmetry. A distribution, or data set, is symmetric if it looks the same to the left and right of the center point. Kurtosis is a measure of whether the data are peaked or flat relative to a normal distribution. That is, data sets with high kurtosis tend to have a distinct peak near the mean, decline rather rapidly, and have heavy tails. Data sets with low kurtosis tend to have a flat top near the mean rather than a sharp peak. The skewness for a normal distribution is zero and the kurtosis for a standard normal distribution is three.

The bottom panel show the two stage of the emission arbitrarily normalized to compare the morphological structures.

It is clear that the two structures are self-similarity. The mean, the variance, the standard deviation and the autocorrelation function of the first and second half of the light curve are comparable, while the morphological structures are gradually distorted (for example skewed) during the emission as shown by the calculated values of skewness and kurtosis.

We emphasize that these behaviors are directly linked to the internal engine activity. The observed variability time scale, δt, reflects the variability of the source, while the overall duration of the burst reflects the overall duration of the activity of the inner engine. Numerical simulations (Kobayashi et al., 1997) have shown that not only are the time scales preserved but the source's temporal behavior is reproduced on an almost one-to-one basis in the observed light curve.

The same analysis is performed for the prompt γ–ray emission and opposite conclusions are obtained. The intrinsic properties, of the underlying system, change during their complex evolution. This intrinsic difference in the temporal properties of the two halves of the light curve seems also to be reflected the difference of the autocorrelation functions. Like the mean and variance, the autocorrelation function of the first and second half of the light curve show differences, so the γ-ray light curve of GRB 080319B is non-stationary. It is interested to note that the skewness parameter remains unchanged (see table 6.3 and fig. 6.8).

Optical First Stage: Parameters				
Mean	Std	Variance	Skewness	Kurtosis
5.80 ± 0.03	0.30 ± 0.03	0.09 ± 0.03	0.94 ± 0.04	-0.36 ± 0.05
Optical Second Stage: Parameters				
Mean	Std	Variance	Skewness	Kurtosis
6.10 ± 0.02	0.24 ± 0.04	0.06 ± 0.03	0.84 ± 0.03	-0.16 ± 0.06

Table 6.2: The optical light curves is divided into two equal parts and mean, variance, skewness and kurtosis are computed.

γ First Stage: Parameters				
Mean	Std	Variance	Skewness	Kurtosis
16.17 ± 0.06	2.1 ± 0.08	4.41 ± 0.08	-0.28 ± 0.04	-0.44 ± 0.07

γ Second Stage: Parameters				
Mean	Std	Variance	Skewness	Kurtosis
13.31 ± 0.05	1.6 ± 0.06	2.60 ± 0.05	-0.29 ± 0.05	-0.54 ± 0.06

Table 6.3: The γ-ray light curve is divided into two equal parts and mean, variance, skewness and kurtosis are computed.

6.3.3 Observed and Intrinsic Optical Parameters

The four well-detected optical peak flux $F_{opt,1..4}$ [equation **4.1**] is obtained using the calibration of Fukugita et al. (1995) and corrected for galactic extinction (Schlegel et al. 1998). Host galaxy reddening correction A_v is applied assuming the value reported by (Racusin et al. 2008). The independently fits the extinction at different SED epoches (T_0+150 s, 250 s, 350 s, 720 s, 1500 s, 5856 s, 104 s, 3×10^4 s, 8×10^4 s, 2×10^5 s, and 5×10^5 s) yield a mean value of E(B–V)=0.05.

The isotropic equivalent Luminosity L_{opt} for the well-detected optical peaks is related to the peak optical flux $F_{opt,1..4}$ using the equation [**4.2**] For k-correction [**4.3**]we assume $\beta = 0.50 \pm 0.07$ as repoted in Racusin et al. (2008). The optical fluence S_{opt} is determined by numerically integrating the prompt light curve from 2.75 sec to 86.00 sec. The first optical data from "Pi of the Sky" is added in our calculations. The isotropic equivalent of the total optical energy in V band $E_{opt,V}$ in the rest frame of the source is determinated from the optical fluence using the equation [**4.4**]

The prompt optical duration $t_{90,opt}$ is determined as the time since the afterglow detection during which 90% of the optical fluence was received. The prompt optical emission in the proper frame $T_{90,opt}$ was calculated as $t_{90,opt}/(1+z)$

In addition the peak distance in the observer and rest frame of the source are marked with the following notation $d_{Peak1,2}$, $d_{Peak2,3}$,$d_{Peak3,4}$ and distinguished using capital and lowercase letters.

The event is extreme not only in observed properties but intrinsically: it is the most luminous event ever recorded at optical wavelengths and has an exceedingly

Peak Flux		
Flux	value	unit
$F_{opt,1}$	$2.19 \times 10^{-8} \pm 1.64 \times 10^{-9}$	$erg\ s^{-1}\ cm^{-2}$
$F_{opt,2}$	$2.17 \times 10^{-8} \pm 2.86 \times 10^{-9}$	$erg\ s^{-1}\ cm^{-2}$
$F_{opt,3}$	$1.49 \times 10^{-8} \pm 8.08 \times 10^{-9}$	$erg\ s^{-1}\ cm^{-2}$
$F_{opt,4}$	$1.60 \times 10^{-8} \pm 8.87 \times 10^{-9}$	$erg\ s^{-1}\ cm^{-2}$

Peak Luminosity		
Lum	value	unit
$L_{peak,1}$	$7.15 \times 10^{49} \pm 5.35 \times 10^{48}$	$erg\ s^{-1}$
$L_{peak,1}$	$7.08 \times 10^{49} \pm 9.32 \times 10^{48}$	$erg\ s^{-1}$
$L_{peak,1}$	$4.84 \times 10^{49} \pm 2.63 \times 10^{48}$	$erg\ s^{-1}$
$L_{peak,1}$	$5.23 \times 10^{49} \pm 2.89 \times 10^{48}$	$erg\ s^{-1}$

Table 6.4: Prompt Optical Parameters: Peak Flux and Peak Luminosity

Fluence and observed duration		
Par.	value	unit
S_{opt}	$7.17 \times 10^{-7} \pm 1.80 \times 10^{-7}$	$erg\ cm^{-2}$
$t_{90,opt}$	53.6 ± 3	sec

Energy and intrinsic duration		
Par.	value	unit
$E_{opt,V}$	$1.21 \times 10^{51} \pm 3.02 \times 10^{50}$	erg
$T_{90,opt}$	27.63 ± 3	sec

Table 6.5: Prompt Optical Parameters: Energy and observed and intrinsic duration

high isotropic-equivalent energy release in γ-rays. The previous record was held in brightness by GRB 990123, GRB 050904, GRB 061007. In spite of its initial brightness, the behavior of the afterglow at middle/late time does not appear to be peculiar. The extrapolated luminosity e.g. at 10 hour and 13 hour in the rest frame of the source ($L_{opt,10} \approx 3.16 \times 10^{44}$ and $L_{opt,13} \approx 9.77 \times 10^{43}$ respectively) are comparable with the average luminosity of the afterglow sample detected over the past years. The table 1.2 shows the average extrapolated luminosity during the afterglow evolution for a sample of 87 GRBs, confirming the universality of afterglows properties (§4.1.5) at middle/late stage also for the naked–eye GRB 080319B.

It interesting to note that the peaks detected during the γ-ray emission do not follow a cosmological evolution as show in §4.2

Observed Peak Distance		
Par.	value	unit
$d_{Peak1,2}$	8.7 ± 0.4	s
$d_{Peak2,3}$	9.0 ± 0.3	s
$d_{Peak3,4}$	8.2 ± 0.5	s

Intrinsic Peak Distance		
Par.	value	unit
$D_{Peak1,2}$	4.48 ± 0.4	s
$D_{Peak2,3}$	4.64 ± 0.3	s
$D_{Peak3,4}$	4.22 ± 0.5	s

Table 6.6: Prompt Optical Parameters: Observed and Peak distance

Table 6.7: Log of Observations of GRB 080319B Prompt Optical Emission. 1.3 sec time resolution. Time t_0 is measured from BAT trigger.

t_0(s)	**mag**	**exp**	**err**	t_0(s)	**mag**	**exp**	**err**
6.91	8.28	0.65	0.82	47.10	6.05	0.65	0.07
8.21	8.55	0.65	1.05	48.40	6.09	0.65	0.11
9.50	7.41	0.65	0.38	49.70	6.25	0.65	0.08
10.80	6.80	0.65	0.21	50.99	6.35	0.65	0.10
12.10	6.25	0.65	0.15	52.29	6.59	0.65	0.09
13.39	5.96	0.65	0.10	53.59	6.56	0.65	0.10
14.69	5.67	0.65	0.10	54.88	6.82	0.65	0.10
15.98	5.67	0.65	0.10	56.18	6.83	0.65	0.11
17.28	5.53	0.65	0.07	57.48	7.11	0.65	0.13
18.58	5.54	0.65	0.07	58.77	7.17	0.65	0.14

Continued on next page

Table 6.7 – continued from previous page

t_0(s)	mag	exp	err	t_0	mag	exp	err
19.87	5.43	0.65	0.07	60.07	7.28	0.65	0.16
21.17	5.50	0.65	0.08	61.37	7.50	0.65	0.20
22.47	5.66	0.65	0.09	62.66	7.51	0.65	0.18
23.76	5.79	0.65	0.09	63.96	7.70	0.65	0.22
25.06	5.57	0.65	0.06	65.26	7.74	0.65	0.24
26.36	5.44	0.65	0.13	66.55	7.72	0.65	0.23
27.65	5.53	0.65	0.17	67.85	7.71	0.65	0.23
28.95	5.72	0.65	0.17	69.15	8.02	0.65	0.30
30.25	6.02	0.65	0.06	70.44	8.08	0.65	0.33
31.54	6.25	0.65	0.10	71.74	8.10	0.65	0.32
32.84	6.38	0.65	0.07	73.03	8.17	0.65	0.35
34.14	6.01	0.65	0.07	74.33	8.85	0.65	0.66
35.43	5.85	0.65	0.05	75.63	8.20	0.65	0.35
36.73	5.94	0.65	0.07	76.92	8.99	0.65	0.69
38.03	5.96	0.65	0.07	78.22	8.41	0.65	0.44
39.32	6.12	0.65	0.07	79.52	9.13	0.65	0.86
40.62	6.04	0.65	0.07	80.81	9.03	0.65	0.78
41.92	6.00	0.65	0.07	82.11	9.16	0.65	0.84
43.21	5.77	0.65	0.06	83.41	8.80	0.65	0.60
44.51	5.89	0.65	0.06	84.70	9.03	0.65	0.78
45.81	5.96	0.65	0.06	86.00	8.91	0.65	0.70

6.4 Prompt γ vs Prompt optical

6.4.1 Peaks Shifted

The cross correlation between the TORTORA light curve and the BAT prompt emission are performed using a sampling time equal to 1.3 sec in order to minimize the error in cross correlation method. For 1.3 sec bin the photometric error associated with TORTORA measures are on average less than 25 %. Moreover the optical light curve has an equidistant sampling in the time so as to ensure proper cross correlation.

A visual comparison shows that similar morphological structure are presented in plateau (15 sec–50sec) phase of the two emission. The power–law index of their rising and declining part are quite different. This result indicates that optical and γ emission are generated in different or nearby spatial region. When attempting to shift back the optical plateaux to a certain time, the correlation coefficient between the two emission gradually become larger. The maximum correlation between optical and γ light curve is obtained for a delay $\sim 2 \pm 0.65$ seconds in observed frame. The correlation is $r = 0.82$. The fig 6.11 shows TORTORA optical flux shifted back 2 seconds along with correspondingly rebinned Swift/BAT γ-ray flux. γ–ray light curve is in arbitrary unit for illustrative purposes. The error associated to the peak distance is calculated taking in account the middle time of the bin.

Finally the the estimation of the Hurst exponent (§3). The Hurst exponent for the prompt optical emission, $H_H \sim 0.95$, is consistent with the values found in the high energy emission, $H_H \sim 0.91$ (table 3.2).

Though the two emission are related, the degree of stationarity seems to be different.

6.5 Interpretation of the Chromatic Afterglow

6.5.1 two-component jet model

The optical, X-ray, and γ-ray emissions from this burst are explained reasonably well by a two-component jet model, consisting of an ultra-relativistic narrow jet surrounded by a broader and less energetic jet with a lower Lorentz factor (Racusin et al., 2008).

The empirical triple broken power-law of the X-ray light curve is then interpreted as the superposition of two broken power-law components representing these two jets. On the other hand, the X-ray light curve in the interval 50 s $<$ t $<$ 40 ks is dominated by the forward shock of the narrow jet component interacting with a surrounding medium produced by the wind of the progenitor star in the slow cooling case. The first break in the X-ray light curve is attributed to a jet break in this narrow jet. Since this break is not seen in the optical light curve, the optical flux from the narrow jet must be much less than that of the wide jet. The optical emission after t_0 + 800 s is dominated by a single power-law with consistent with

the expectation for forward shock emission from the wide jet with. The late X-ray afterglow after 40 ks is also dominated by the forward shock of the wide jet.

At approximately 11 days post-burst, the X-ray light curve breaks to a steeper slope (confirmed by a late observation with the Chandra X–ray Observaory). This break can be interpreted as the jet break of the wide jet. The forward shock of the wide jet also accounts for the observed radio emission, which is strongly modulated by the effects of Galactic scintillation when the source is small.

In detail the afterglow of GRB 080319B can be well described by a two-component jet model, with a very narrow ($\sim 0.4^{\circ}$) and highly relativistic jet, coaxial with a wider ($\sim 8^{\circ}$) jet having more conventional properties. Considering the rarity of this event, this model is probably statistically acceptable.

The probability of observing within the tiny solid angle of the narrow jet is small ($\sim 10^{-3}$). If every GRB has such a narrow jet, we should expect to detect the narrow jet emission from a GRB every $\sim$ 3–10 years. Had we observed GRB 080319B even slightly off-axis, the behavior may have appeared similar to many other GRB afterglows. Despite the incredibly high flux and fluence of GRB 080319B, the total jet-corrected observed energy budget ($\sim 4 \times 10^{50}\ erg$) is moderate, and is consistent with the overall distribution for all GRBs.

6.6 Discussion and Conclusion

6.6.1 Residual Collisions at Large Radii

Two-component jet may explains the late time optical/X–ray late afterglow and the exceptional brightness of this event. To explain the prompt optical emission additional theoretical considerations must be made.

Here we summarize the observed properties previously reported and discuss them into the frame of the various theories.

I. The delay between the γ /optical peak emissions is $\sim$ 1 sec in the rest frame of the source. They arise from nearby region of the central engine.

II. Optical and γ emission have the same modulation due to internal engine (self-affinity).

III. Optical emission and γ-ray emission have the same physical nature and follow a similar energetic trend (two contemporary regions of different mean

intensity level in optical and γ radiations). Moreover the Hurst exponent H for optical and γ–ray flux are comparable indicating that the processes at work during the emissions are of the same nature.

IV. the γ–ray emission is non-stationarity while the optical component appears to be stationarity. Apparently the morphological structure of the two light curves appear quite similar with respect to their linear properties, however they are intrinsically different, with state characterized by different degree of complexity.

V. Although a coherent periodicity is ruled out, the pulses exhibit a recurrence time ~ 9 sec.

VI. The last peak shows a short time scale variability

The Observational parameters derived for the prompt optical emission appear to satisfy the predictions of Li & Waxman, (2008). According to this theory the optical emission could be produced by "residual" collisions at large radii. The late residual collisions seem take in account the relatively bright optical emission (see fig.6.13). In detail the fluctuations in flow properties on short, ~ 1 ms, time scale, which drive the γ-ray producing collisions at small radii, are expected to lead to residual collisions at much larger radii, where the optical depth to optical photons is low.

The time delay between γ-ray and optical emission in this model,

$$\tau_{\rm delay} \approx R_{\rm op}/2\Gamma^2 c \sim 0.2 R_{\rm op,15}\Gamma_{2.5}^{-2}{\rm s}, \tag{6.1}$$

is expected to be within few seconds, in agreement with the observational data. Thus, optical and γ-ray emission may appear to be simultaneous if the temporal resolution of the optical observations is greater than several seconds. For the first time the temporal resolution of TORTORA made it possible to determine systematic time delay between the two wave bands.

Wei (2007) has suggested that optical emission may be generated by strong internal shocks at radii $R/c > 10^6$ s, driven by shells emitted with a large time delay, ~ 10 s, following those producing the main γ-ray emission. In the residual collision model the optical emission is naturally expected to arise, without postulating the existence of delayed shells, by residual collisions at $R/c \sim 10^4$ s, in

which the characteristic emitted photon frequency is low, $h\nu \sim 1$ eV, due to the reduction of the Lorentz factor variance in the flow (rather than by the large radius $R/c > 10^6$ s). The optical emission is produced at large radii, where synchrotron self-absorption is avoided.

This may explain why we observe self–affinity phenomena in which the small *replica* may be somewhat distorted with respect to the whole, retaining a degree of similarity. The small pieces are rescaled by different amounts in the x and y directions through anisotropic transformation. The underlying physical process is the same also if gradually change over time, decreasing the number of collisions and its energetic so reducing the degree of complexity. Probably this particular physical shell evolution may explain the detected nonstationarity/stationarity of the γ–ray emission and optical respectively.

As the flow radius increases, the typical number $n(R)$ of initial shells that merge into one single shell increases, and the variance of the Lorenz factors of the resulting shells decreases. For a group of shells with a small Lorenz factor variance, the velocities v_i of the shells in the shells' center of momentum frame are not highly relativistic. In this case, conservation of momentum implies that the velocity of a merged group of shells is given by the average of merged shells' velocities, $\bar{v} = (1/n)\sum_{i=1}^{n} v_i$, and that the variance of the velocities of merged groups of shells is $\sigma_v(n) = \sigma_{v,0}/\sqrt{n}$ where $\sigma_{v,0}$ is the initial variance. This, in turn, implies that the variance of (observer frame) Lorenz factors, $\sigma_\Gamma(n)/\Gamma \approx \sigma_v(n)/c$, evolves like $\sigma_\Gamma(n) = \sigma_{\Gamma,0}/\sqrt{n}$. Collisions of merged groups of n shells will therefore take place at a radius $R(n) \sim \Gamma^3 c \times n t_{\rm var}/\sigma_\Gamma(n)$, which implies

$$n \propto R^{2/3}, \quad \sigma_v \propto \sigma_\Gamma \propto R^{-1/3}. \tag{6.2}$$

The outflow energy that may be dissipated and radiated away is the energy associated with the random velocities of the shells (in the outflow rest frame). This energy decreases as

$$E_{\rm fluc} \propto \Gamma \sigma_v^2 \propto R^{-2/3}. \tag{6.3}$$

The γ and optical emissions of GRB 080319B, apparently quite similar with respect to their linear properties, are intrinsically different, characterized by different degree of freedom. When the initial shells merge into one single shell the variance of the Lorenz factors and of the resulting shells decreases. The decrease in velocity and the increase in mass of the shell may gradually generate a phenomenon less

complex with less degrees of freedom

However we rule out the possible interpretation of the optical flashes resulted from external shock emission (Zou et al., 2009). This is not consistent with ~ 1 second delay in the rest frame of the source between the optical and γ-rays signals. The optical flash may result from external shock emission if we observe several seconds delay between the optical and γ–rays signals.

We rule out also that the optical emission may arise from internal forward-reverse shocks (Yu, Wang & Dai 2008) in according to the self-affinity detected in the two emissions. Into the framework of the internal shock model, Yu, Wang & Dai 2009 speculate that the collisions between a series of relativistic shells generate lots of paired forward and reverse shocks. If the Lorentz factors of these two types of shocks are significantly different with each other (e.g., one shock is relativistic and the other is Newtonian) then the synchrotron emission produced by the forward and reverse shocks respectively could peak at two quite different energy bands. In addition, this scenario predicts an accompanying inverse-Compton (IC) GeV emission with a luminosity comparable to that of the synchrotron MeV emission, which can be tested with future Fermi observations.

Finally the four nearly equidistant flares and the short time scale variability detected in the last peak may be explain into the framework of massive accretion disk instability around the newly born black hole and jet-precession mechanism (Beskin et al., in preparation)

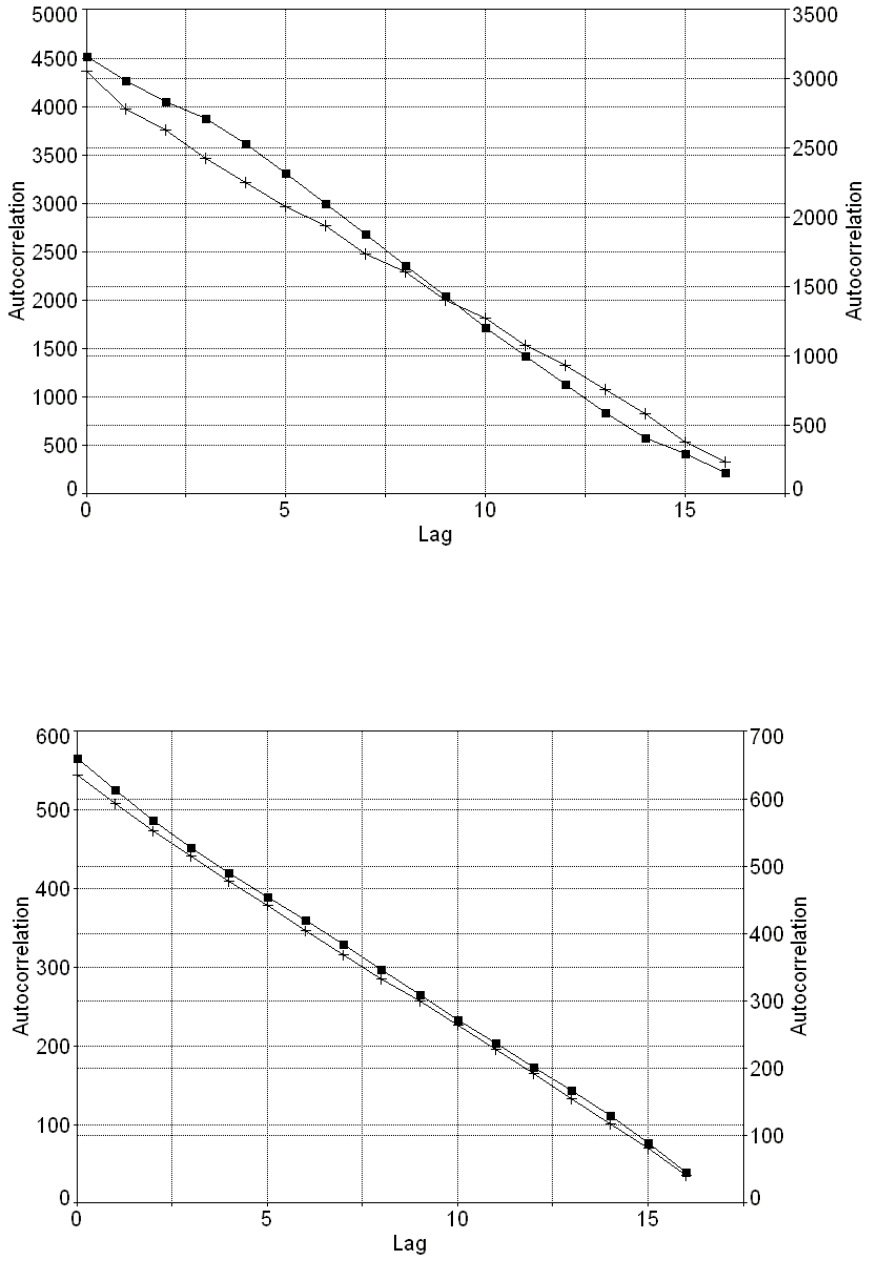

Figure 6.8: Autocorrelation functions of the two half. The first part of the emissions are indicated with square symbols and the second part of the light curves are plotted using cross symbols. Since this is symmetric for real data, only the positive lags are plotted. The rate at which the autocorrelation function decays to zero may be interpreted as a measure of the memory of the process. Top: prompt optical emission. Bottom: prompt γ-ray emission

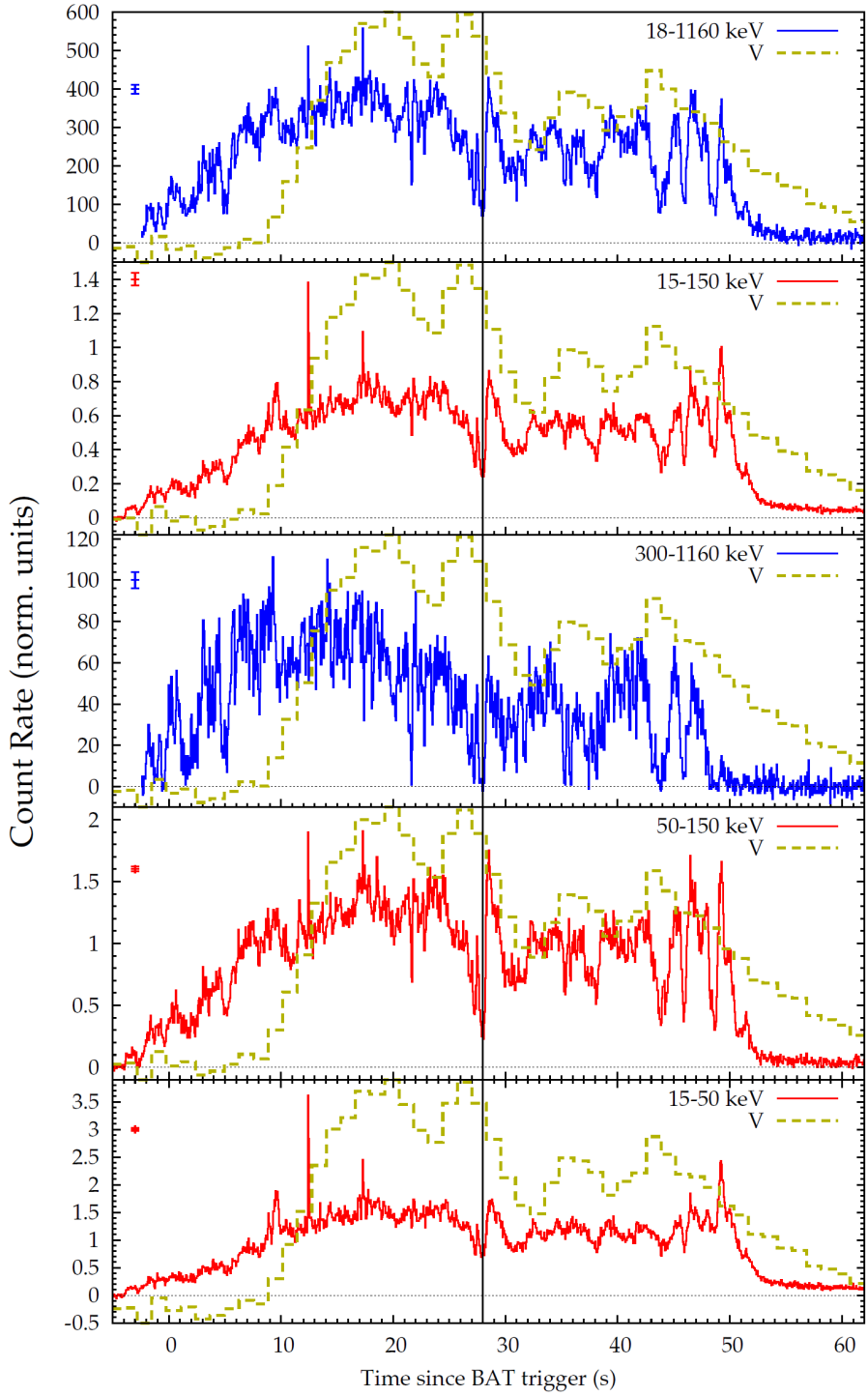

Figure 6.9: From bottom to top: the solid lines show the 15–50, 50–150 (BAT), 300–1160 keV (KW), and full passband 15–150 keV (BAT) and 18–1160 keV (KW) light curves of GRB 080319B. The corresponding binning time is 64 ms. The typical error bar on the count rates is shown in the top left of each panel. In each plot the optical flux as measured by TORTORA is also shown (dashed line). Flux units are arbitrary. The vertical line splits the profile in two parts.

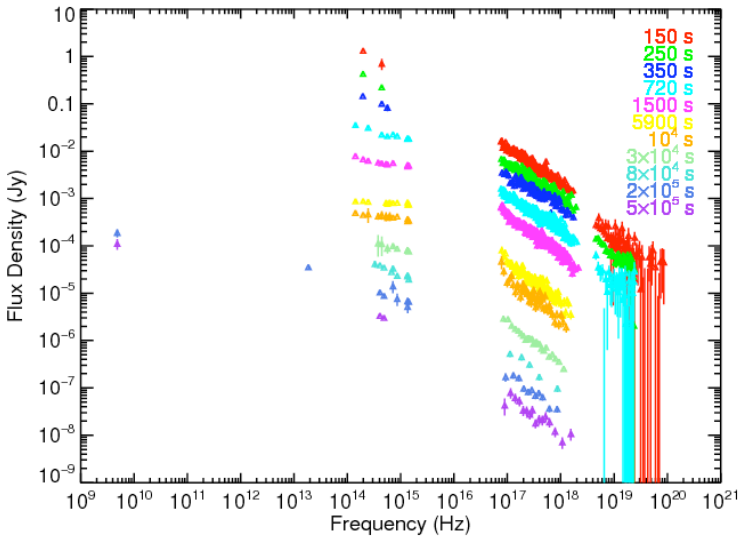

Figure 6.10: Different SED epoches. There is only a modest amount of dust in the host galaxy reference frame as shown. SMC consistently provides the best fits. The SMC law generally best represents the low metallicity dwarf galaxies that host GRBs. From Racusin et al., 2008.

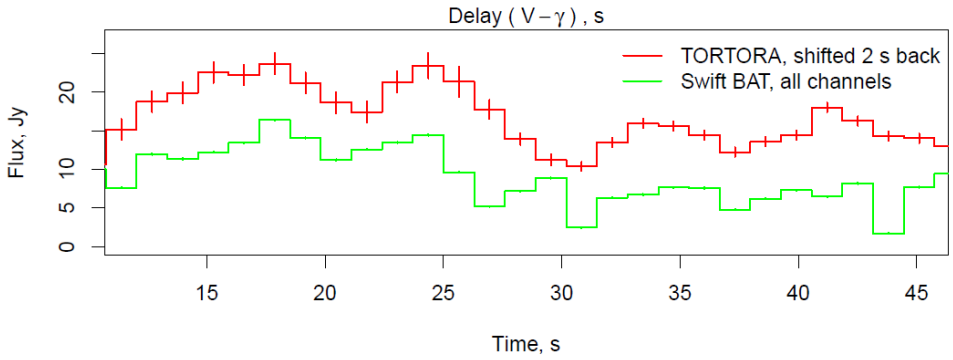

Figure 6.11: TORTORA optical flux shifted back 2 seconds along with correspondingly rebinned Swift–BAT γ-ray flux. The correlation is $r = 0.82$. γ-ray curve is arbitrarily scaled and shifted for illustrative purposes.

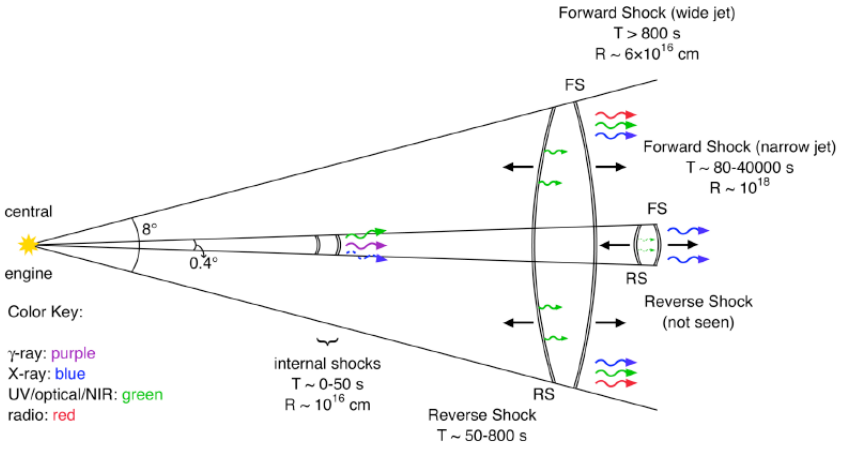

Figure 6.12: Schematic of Two-Component Jet Model. Summary diagram showing spectral and temporal elements of our two-component jet model. The prompt γ–ray emission is due to the internal shocks in the narrow jet, and the afterglow is a result of the forward and reverse shocks from both the narrow and wide jets.

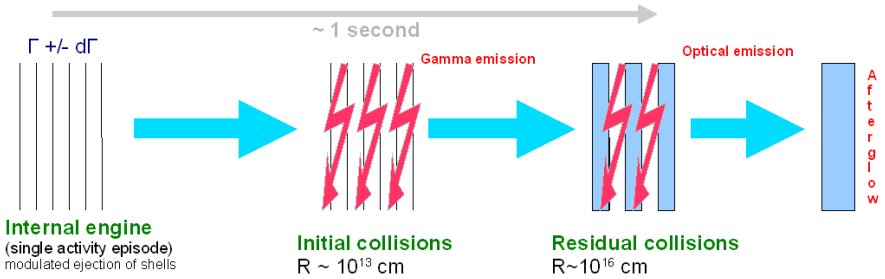

Figure 6.13: Residual collision model; the short fluctuations in flow properties, which drive the γ-ray producing collisions at small radii, are expected to lead to residual collisions at much larger radii, where the optical depth to optical photons is low.

Conclusion

Here we briefly report the results obtained in the present phd thesis work.

The possibility to image on time scales of seconds the behavior of transient events that seem to populate the universe at any epochs, has suggested to try to seek additional informations using nonlinear analysis methods. In particular it is introduced a suitable statistical tool, named Hurst exponent, H, to characterize the complex and random structures that these emissions manifest during their short and erratic duration. Our numerical simulations show that for BAT/Swift GRB the best estimates of H are provided by Higuchi method and Aggregate Variance method. We have found that the observational properties of the prompt γ-ray emission do not seem to follow any cosmological evolution trend and they are the manifestation of same physical phenomenon that is self-affinity at every scale and at any epoch of the universe. Moreover in our analysis we found H $\sim$ 0.8. This value is significantly larger than the value of 0.5 that would correspond to variations produced by a white noise process indicating that the physics that produces the prompt emission is a correlated random process. The PDS slope found in the previous work coincides with the Kolmogorov law. The calculation of Hurst exponent in our analysis suggest opposite conclusion and it reveal that the diversity of GRB is due to realizations of the same process which is self-affinity over a range of time scales. Finally if there are two bursts with the same form of time profile but different duration, the H indexes of these bursts will be the same. This properties suggest us, for example, to comparison different astrophysical object: AGN and GRB.

The optical data gathered here show a cosmological evolution trend on various

intrinsic GRB features. In particular, we have found that the optical burst duration, the isotropic optical luminosity at the observed maximum and the time integrated isotropic energy are all redshift-dependent. This fact suggests that the intrinsic optical afterglow luminosity follows the cosmological evolution of a circumburst environment which determines the optical afterglow luminosity rate. Cosmological evolution trend in optical afterglow may be appreciated during particular stage of the afterglow emission (100-6000 sec after their explosion). In particular in our sample there are 11 well-detected peaks that are not coincident with the work of the γ-ray activity phase. The peak luminosity for these objects have a strong correlation with the redshift r=0.92. They are important tool to study the properties of the interstellar medium and the physical mechanism of the external shock emission during the transition phases. We have speculated in the frame work of the internal/external shock model. The afterglows begins while internal shocks are still going on and the initial part of the afterglow overlaps the late. Thus, when the γ–ray afterglow is completely extinguished, the external shock following the evolution of the Universe around them. This phase lasts a few minutes, after the light curves gradually standardize showing common behavior. We believe the the redshift-dependence is well-observed in the peaks that arise during the afterglow evolution, because their energy exceeds the residual γ–ray flow that contaminates the optical emission during the transition phase between internal/external shock.

Our team have successfully installed TORTORA camera on the top of the REM telescope. The TORTORA's first light images were taken on 12 May 2006. The optical monitoring systems which operated in the past and those still working, like ROTSE, RAPTOR, Pi of the Sky are not able to resolve the temporal structure of prompt optical emission down to timescale shorter than 5–10 seconds. TORTORA camera operates since June 2006, approximately half of observational time (when REM is not performing its scheduled programme) it follows up Swift of view too. Since may 2006 we accumulated approximately 150 nigh of observations in $24deg \times 32deg = 768deg^2$ field up to 10.5 unfiltered magnitude with 0.13 sec One of the important result of our routine observations is the estimation of the rate of the orphan transients. Thus we can state that prompt optical transients rate is less then $7.7 \times 10^{-9} deg^{-2} sec^{-1}$ for transients that

are brighter then 10.5^m on 0.13 s timescale during at least of 3 successive frames (0.4 sec).

TORTORA camera has successfully observed the prompt optical emission of the remarkable case of the naked-eye GRB 080319B before, after and during the γ-ray activity phase and discovered its fast optical variability.

The similarity of the overall structure of the optical and *gamma*-ray light curves, namely the presence of two stages of emission with different average levels, a nearly simultaneous rise and fall of the emission, suggests that they reflect the same prolonged activity of the inner engine. Moreover the presence of four nearly equidistant peaks in the optical light curve may suggest the periodicity of the inner engine activity. Finally the observational parameters derived for the prompt optical emission ~ 1 delay between the γ-ray and optical peaks in the rest frame of the source) appear to satisfy the predictions of Li & Waxman, (2008). According to this theory the optical emission could be produced by "residual" collisions at large radii. We rule out the possible interpretation that the optical flashes are generated from external shock emission (Zou et al., 2009) as well as that the optical emission may arise from internal forward-reverse shocks (Yu, Wang & Dai 2008) taking in account the self-affinity of the two phenomena.

The afterglow of GRB 080319B can be well described by a two-component jet model, with a very narrow ($\sim 0.4^\circ$) and highly relativistic jet, coaxial with a wider ($\sim 8^\circ$) jet having more conventional properties. Considering the rarity of this event, this model is probably statistically acceptable.

The probability of observing within the tiny solid angle of the narrow jet is small ($\sim 10^{-3}$). If every GRB has such a narrow jet, we should expect to detect the narrow jet emission from a GRB every $\sim$ 3–10 years.

The event is extreme not only in observed properties but intrinsically: it is the most luminous event ever recorded at optical wavelengths and has an exceedingly high isotropic-equivalent energy release in γ-rays. The previous record was held in brightness by GRB 990123, GRB 050904, GRB 061007. In spite of its initial brightness, the behavior of the afterglow at middle/late time does not appear to be peculiar. The extrapolated luminosity e.g. at 10 hour and 13 hour in the rest frame of the source ($L_{opt,10} \approx 3.16 \times 10^{44}$ and $L_{opt,13} \approx 9.77 \times 10^{43}$ respectively) are comparable with the average luminosity of the afterglow sample detected over the past years. The table 1.2 shows the average extrapolated luminosity during the

afterglow evolution for a sample of 87 GRBs, confirming the universality of afterglows properties (§4.1.5) at middle/late stage also for the naked-eye GRB 080319B. Finally the four nearly equidistant flares and the short time scale variability detected in the last peak may be explain into the framework of massive accretion disk instability around the newly born black hole and jet-precession mechanism (Beskin et al., in preparation)

It is the first time that such accurate analysis can be made for the prompt optical emission of a GRB and many mysteries are yet to be disclosed.

Our Reference

The bulk of our work is presented in the following articles:

Investigation of gamma-ray bursts with known redshifts: Statistical analysis of parameter Astronomy Letters 35:1, 7-24 D. Bad'in, G. Beskin & G. Greco, 2009

G. Beskin, S. Karpov, S. Bondar, G. Greco, A. Guarnieri, C. Bartolini, A. Piccioni, E. Molinari, G. Chincarini, 2008,
TORTORA discovery of Naked-Eye Burst fast optical variability,
AIP Conference Proceedings, Volume 1065, pp. 251-254

G. Beskin, S. Karpov, S. Bondar, G. Greco, A. Guarnieri, C. Bartolini, G. Chincarini, E. Molinari,
Fast Optical Variability Of Naked-Eye Burst
In preparation

G. Beskin, S. Bondar, E. Ivanov, S. Karpov, E. Katkova, A. Pozanenko, A. Guarnieri, C. Bartolini, A. Piccioni, G. Greco, E. Molinari, S. Covino, 2008,
Monitoring with high temporal resolution to search for optical transients in the wide field,
HIGH TIME RESOLUTION ASTROPHYSICS, The Universe at Sub-Second Timescales. AIP Conference Proceedings, Volume 984, pp. 73-80

S. Covino, C. Guidorzi, R. Margutti, S. Campana, G. Chincarini, P. D'Avanzo, D. Fugazza, E. Molinari, A Moretti, F. Zerbi, S. Karpov, G. Beskin, V. M. D'Elia, F. Fiore, V. Testa, G. Greco, C. Bartolini, A. Guarnieri, A. Piccioni, E. Palazzi, L. Nicastro, S. Bondar, M. Della Valle, V. La Parola, V. Mangano, G. Cusumano, M. Perri, G. Tosti, 2009,
GRB 080319B: the prompt emission of the "Naked Eye Burst", RELATIVISTIC ASTROPHYSICS: 5th Sino-Italian Workshop on Relativistic **Astrophysics. AIP Conference Proceedings, Volume 1059, pp. 59-62**

G. Greco, G. Beskin, S. Bondar, S. Karpov, C. Bartolini, , A. Guarnieri, A. Piccioni,

G. Chincarini, S. Covino, C. Guidorzi and E. Molinari, 2008,
TORTORA Light Curve of GRB 080319B,
Conference Proceedings of the Italian Physical Society, in press.

GRBs with optical afterglow and known redshift: A statistical study, Il Nuovo Cimento B, vol. 121, Issue 12, p.1487-1488 G. Greco, D. Bad'in, G. Beskin, C. Bartolini, S. Karpov, A. Guarnieri, A. Piccioni, A. Biryukov, 2006

Statistical Analysis of GRBs with Known Redshifts AIP Conference Proceedings, Volume 1065, pp. 75-78 G. Greco, G. Beskin, D. Bad'in, S. Karpov, C. Bartolini, A. Guarnieri, 2008

A. Guarnieri, C. Bartolini, G. Beskin, S. Bondar, G. Greco, S. Karpov, D. Nanni, A. Piccioni, F. Terra, E. Molinari, G. Chincarini, F. M. Zerbi, S. Covino, V. Testa, G. Tosti, F. Vitali, L. A. Antonelli, P. Conconi, G. Cutispoto, G. Malaspina, L. Nicastro, E. Palazzi, E. Meurs, P. Goldoni, 2006,
TORTOREM OPTICAL UPPER LIMIT, **GCN CIRCULAR 5372**

S. Karpov, G. Beskin, S. Bondar, C. Bartolini, G. Greco, A. Guarnieri, A. Piccioni, D. Nanni, F. Terra, E. Molinari, G. Chincarini, F.M. Zerbi, S. Covino, V. Testa, G. Tosti, F. Vitali, L.A. Antonelli P. Conconi, G. Cutispoto, G. Malaspina, L. Nicastro, E. Palazzi, E. Meurs, P. Goldoni, 2008,
TORTORA light curve
GCN CIRCULAR 7558

S. Karpov, G. Beskin, S. Bondar, C. Bartolini, G. Greco, A. Guarnieri, A. Piccioni, D. Nanni, F. Terra, E. Molinari, G. Chincarini, F.M. Zerbi, S. Covino, V. Testa, G. Tosti, F. Vitali, L.A. Antonelli P. Conconi, G. Cutispoto, G. Malaspina, L. Nicastro, E. Palazzi, E. Meurs, P. Goldoni, 2008,
GRB 080319B: TORTORA light curve
GCN CIRCULAR 7502

S. Karpov, G. Beskin, S. Bondar, C. Bartolini, G. Greco, A. Guarnieri, A. Piccioni, D. Nanni, F. Terra, E. Molinari, G. Chincarini, F.M. Zerbi, S. Covino, V. Testa, G. Tosti, F. Vitali, L.A. Antonelli P. Conconi, G. Cutispoto, G. Malaspina, L. Nicastro, E. Palazzi, E. Meurs, P. Goldoni, 2006,
TORTOREM OPTICAL UPPER LIMIT, **GCN CIRCULAR 5897**

S. Karpov, G. Beskin, S. Bondar, C. Bartolini, G. Greco, A. Guarnieri, A. Piccioni, D. Nanni, F. Terra, E. Molinari, G. Chincarini, F.M. Zerbi, S. Covino, V. Testa, G. Tosti, F. Vitali, L.A. Antonelli P. Conconi, G. Cutispoto, G. Malaspina, L. Nicastro, E. Palazzi, E. Meurs, P. Goldoni, 2006,
TORTOREM OPTICAL UPPER LIMIT, **GCN CIRCULAR 5941**

E. Molinari, S. Bondar, S. Karpov, G. Beskin, A. Biryukov, E. Ivanov, C. Bartolini, G. Greco, A. Guarnieri, A. Piccioni, F. Terra, D. Nanni, G. Chincarini, F.M Zerbi, S. Covino, V. Testa, G. Tosti, F. Vitali, L.A. Antonelli, P. Conconi, G. Malaspina, L. Nicastro, E. Palazzi, E., 2006,
TORTOREM: Two-telescope complex for detection and investigation of optical transient,
Il Nuovo Cimento B, vol. 121, Issue 12, p.1525-1526

E. Molinari, G. Beskin, S. Bondar, S. Karpov, V. Plokhotnichenko, V. de-Bur, G. Greco, C. Bartolini, A. Guarnieri, A. Piccioni, 2008,
Ground-based complex for detection and investigation of fast optical transients in wide field,
SPIE–The International Society for Optical Engineering

J. L. Racusin, S. V. Karpov, M. Sokolowski, J. Granot, X. F. Wu, V. Pal'shin, S. Covino, A. J. van der Horst, S. R. Oates, P. Schady, R. J. Smith, J. Cummings, R. L. C. Starling, L. W. Piotrowski, B. Zhang, P. A. Evans, S. T. Holland, K. Malek, M. T. Page, L. Vetere, R. Margutti, C. Guidorzi, A. P. Kamble, P. A. Curran, A. Beardmore, C. Kouveliotou, L. Mankiewicz, A. Melandri, P. T. O'Brien, K. L. Page, T. Piran, N. R. Tanvir, G. Wrochna, R. L. Aptekar, S. Barthelmy, C. Bartolini, G. M. Beskin, S. Bondar, M. Bremer, S. Campana, A. Castro-Tirado, A. Cucchiara, M. Cwiok, P. D'Avanzo, V. D'Elia, M. Della Valle, A. de Ugarte Postigo, W. Dominik, A. Falcone, F. Fiore, D. B. Fox, D. D. Frederiks, A. S. Fruchter, D. Fugazza, M. A. Garrett, N. Gehrels, S. Golenetskii, A. Gomboc, J. Gorosabel, G. Greco, A. Guarnieri, S. Immler, M. Jelinek, G. Kasprowicz, V. La Parola, A. J. Levan, V. Mangano, E. P. Mazets, E. Molinari, A. Moretti, K. Nawrocki, P. P. Oleynik, J. P. Osborne, C. Pagani, S. B. Pandey, Z. Paragi, M. Perri, A. Piccioni, E. Ramirez-Ruiz, P. W. A. Roming, I. A. Steele, R. G. Strom, V. Testa, G. Tosti, M. V. Ulanov, K. Wiersema, R. A. M. J. Wijers, J. M. Winters, A. F. Zarnecki, F. Zerbi, P. Mészáros, G. Chincarini & D. N. Burrows, 2008,
Broadband observations of the naked-eye big gamma-ray burst GRB 080319B,
Nature 455, 183-188

Bibliography

Akerlof, C., Balsano, R., Barthelmy, S., Bloch, J., Butterworth, P., Casperson, D., Cline, T., Fletcher, S., Frontera, F., Gisler, G., et al., 1999 *Nature*, 398, 400

Alard & Lupton, 1998 *Astrophys. J.*, 503,325

Amati, L. et al. 2002, A&A, 390, 81

Amati, L. 2006, *Mon. Not. R. astr. Soc.*, 372, 233

Amati, L. et al. 2008, *Mon. Not. R. astr. Soc.*, 391, 577A

Arkhangelskaja I., 2002, *COSPAR Scientific Assembly* The Second World Space Congress, held 10-19 October, 2002 in Houston, TX, USA.

Band, D.L. et al., 1997, *Astron. J.*, 485, 747

Barthelmy, Scott D., Barbier, Louis M., Cummings, Jay R., Fenimore, Gehrels, Neil, Hullinger, Derek, Krimm, Hans A., Markwardt, Craig B., Palmer, David M., Parsons, Ann., et al., 2005 *Space Science Reviews* 120, 143

Barthelmy, S. D., Butterworth, P., Cline, T. L. & Gehrels, N. 1998, *American Astronomical Society* 192, 4311B

artolini, C., Beskin, G., Cosentino, G., et al., 2001 *Gamma-Ray Bursts in the Afterglow Era, Workshop* 581, 981

Bassingthwaighte, J.B., Raymond, G.M. 1995 *Annals of Biomedical Engineering* 23, 491

Beloborodov, Andrei M., Stern, Boris E., Svensson, R. 2000 *Astrophys. J.*, 535, 158B

Beskin, G. M., Plokhotnichenko, V., Bartolini, C., Guarnieri, A., Masetti, N., Piccioni, A., Shearer, A., Golden, A., and Auriemma, G. 1999 *American Astronomical Society* 138, 589

Beskin, G. M., Plokhotnichenko, V., Bartolini, C., Guarnieri, A., Masetti, N., Piccioni, A., Shearer, A., Golden, A., & Auriemma, G. 2005a *Astron. Astrophys. Suppl.*, 138, 589

Beskin, G., Bad′in, V., Biryukov, A., Bondar, S., Chuntonov, G., Debur, V., Ivanov, E., Karpov, S., Katkova, E., Plokhotnichenko, V., Pozanenko, A., Zolotukhin, I., Hurley, K., Palazzi, E., Masetti, N., Pian, E., Nicastro, L., Bartolini, C., Guarnieri, A., Piccioni, A., Conconi, P., Molinari, E., Zerbi, F. M., et al., 2005a *Nuovo Cimento c* 28, 751

Bloom, J. S., et al., 2001, *Astrophys. J.*, 121, 2879

Bloom, J. S., Frail, D. & Kulkarni, S. R. 2003, *Astrophys. J.*, 594, 674

Bloom, J. S., Perley, D. A., Li, W., Butler, N. R., Miller, A. A., Kocevski, D., Kann, D. A., Foley, R. J., Chen, H.-W., Filippenko, A. V., et al., 2009 *Astrophys. J.*, 691, 723

Boër, M. & Gendre, B. 2000, A&A, 361, L21

Bondi H., 1970 *Q. J. R. of Astron. Soc* 11, 443

Borozdin, K. N., Brumby, S. P., Galassi, M. C., McGowan, K., Starr, D., Vestrand, T., White, R., Wozniak, P., & Wren, J. A. 2002 *SPIE Conference* 4847, 344

Briggs, M.S. et al., 1999, *Astron. J.*, 524, 82

Burd, A., Cwiok, M., Czyrkowski, H., Dabrowski, R., Dominik, W., Grajda, M., Husejko, M., Jegier, M., et al., 2005 *New Astronomy* 10, 409

Butler, N. R. & Kocevski, D. 2007, *Astrophys. J.*, 671, 656

Calzoletti, L., Melandri, A., Testa, V., Antonelli, L. A., Vitali, F., D'Alessio, F., di Paola, A., Zerbi, F. M., Chincarini, G., Cunniffe, R. et al., 2005 *Nuovo Cimento c* 28, 759C

Castro-Tirado, A. J., Soldán, J., Bernas, M., Páta, P., Rezek, T., Hudec, R., Mateo Sanguino, T. J., de La Morena, B., Bern´a, J. A., Rodríguez, J., et al., 1999 *Astrophys. J. Suppl.*, 138, 583

Cavallo, G. & Rees, M. J. 1978, *Mon. Not. R. astr. Soc.*, 183, 359

Chang, H.-Y. 2006 *J. of Astron. and Space Sciences* 1, 81

Chang, H.-Y., Yoon, S.-J., Choi, C.-S. 2002 A&A, 383, L1

Chen, H.-W., Prochaska, J. X., Bloom, J. S. & Thompson, I. B. 2005, *Astrophys. J.*, 634, L25

Cohen, E., PIRAN, T., 1995, *Astrophys. J. L.*, 444, 25

Costa, E. et al., 1997, *Nature*, 387, 783

Collazzi, A. C., & Schaefer, B. E. 2008, *Astrophys. J.*, 688, 456

Covino, S., D'Avanzo, P., Fugazza, D., Antonelli, L. A., Calzoletti, L., Campana, S., Chincarini, G., Conciatore, M. L., Cutini, S., et al., 2008 *GRB Coordinates Network* 7446,1

Cummings, J., Barthelmy, S. D., Fenimore, E., Gehrels, N., Krimm, H., Markwardt, C., McLean, K., Palmer, D., Parsons, A., Racusin, J. L., et al., 2008 *GRB Coordinates Network* 7462,1

Cwiok, M., Dominik, W., Kasprowicz, G., Majcher, A., Majczyna, A., Malek, K., Mankiewicz, L., Molak, M., Nawrocki, K., Piotrowski, L. W., Rybka, D., Sokolowski, M., Uzycki, J., Wrochna, G., and Zarnecki, A. F. 2008 *GRB Coordinates Network* 7445, 1

Dai, X.; Halpern, J. P.; Morgan, N. D.; Armstrong, E.; Mirabal, N.; Haislip, J. B.; Reichart, D. E.; Stanek, K. Z. 2007, *Astrophys. J.*, 658, 509

Daigne, F. & Mochkovitch, R. 2003, *Mon. Not. R. astr. Soc.*, 342, 587

Dainotti, M. G.; Cardone, V. F.; Capozziello, S. 2008, *Mon. Not. R. astr. Soc.*, 391L 79D

Drago, A. & Pagliara, G. 2008 *Astrophys. J.*, 665, 1227

avies, R. B. & Harte, D. S. 1987, *Biometrika* 74, 95

D'Elia, V., Fiore, F., Perna, R., Krongold, Y., Covino, S., Fugazza, D., Lazzati, D., Nicastro, F., Antonelli, L. A., Campana, S. 2008 *Astrophys. J. L.*, submitted

Della Valle, M., Chincarini, G., Panagia, N., Tagliaferri, G., Malesani, D., Testa, V., Fugazza, D., Campana, S., Covino, S., Mangano, V., Antonelli, L. A., D'Avanzo, P., Hurley, K., Mirabel, I. F., Pellizza, L. J., Piranomonte, S., Stella, L. 2006, *Nature*, 444, 1050

Feder, J. 1988 *Fractals, Plenum Press, New York.* 1, 1

Fenimore, E.E. et al., 1988, *Astrophys. J. L.*, 335, 71

Firmani, C., Avila-Reese, V., Ghisellini, G. & Ghirlanda, G. 2006, *Mon. Not. R. astr. Soc.*, 370, 185

Fishman, Gerald J., Meegan, Charles A. 1995, *Ann. Rev. Astron. Astr.*, 33, 415

Foley, S. et al. 2008, A&A, 484, 143

Frail, D. A. et al. 1997, *Nature*, 389, 261

Frail, D. A. et al. 2001, *Astrophys. J.*, 562, L55

Fukugita, M.; Shimasaku, K.; Ichikawa, T., 1995 *Pub. Astron. Soc. Pac.*, 107, 945

Galama, T., Groot, P. J., Van Paradijs, J., et al. 1997, *Nature*, 387, 479

Gehrels, N. 2004 *American Astronomical Society* 36, 1543

Gendre, B., Boër, M., 2005, A&A , 430, 465

Gehrels, N. et al. 2006, *Nature*, 444, 1044

Gendre, B., Pelisson, S., Boër, M. Basa, S., Mazure, A., 2008, *Astron. Astrophys.*, submitted

Gehrels et al. 2008, *Astrophys. J.*, 689, 1161G

Ghirlanda, G., Ghisellini, G. & Lazzati, D. 2004, *Astrophys. J.*, 616, 331

Ghisellini, G. 2004 *AIP Conference Proceedings* 703, 300

Gliozzi, M., Brinkmann, W., Räth, C., Papadakis, I. E., Negoro, H., Scheingraber, H. 2002 A&A, 391, 875G

Golenetskii, S., Aptekar, R., Mazets, E., Pal'Shin, V., Frederiks, D., Cline, T. 2008 *GRB Coordinates Network* 7482, 1

Greenhough, J., Chapman, S. C., Chaty, S., Dendy, R. O., and Rowlands G. 2002 A&A, 385, 693

Guarnieri, A., Bartolini, C., Beskin, G., Bondar, S., Greco, G., Karpov, S., Nanni, D., Piccioni, A., Terra, F., Molinari, E., Chincarini, G., Zerbi, F. M., Covino, S., Testa, V., Tosti, G., Vitali, F., Antonelli, L. A., et al., 2006 *GRB Coordinates Network* 5372, 1

Guidorzi, C. et al. 2006, *Mon. Not. R. astr. Soc.*, 371, 843

Hafizi, M. & Mochkovitch, R. 2007, *Astron. Astrophys.*, 465, 67

Hakkila, J., Giblin, T. W. 2004, *Astrophys. J.*, 610, 361

Hakkila, J., Giblin, T. W., Norris, J., Fragile, P.C., & Bonnell, J.T. 2008 *Astrophys. J. L.*, in press

Higushi, T. 1988 *Physica D* 277, 283

Higushi, T. 1990 *Physica D* 254, 269

Hjorth, J., Sollerman, J., Moller, P., et al. 2003, *Nature*, 423, 847

Hurst, H. E. 1951 *Transactions of the American Society of Civil Engineers* 116, 770

Ioka, K. & Nakamura, T. 2001, *Astrophys. J. L.*, 554, L163

Jones, C.L., Lonergan, C.T., Mainwaring D.E. 1996 *Journal of Physics A: Math. Gen.* 2509, 2527

Kann, D. A., et al., 2008, *Astrophys. J.*, submitted (arXiv:0804.1959)

Khan Md. M. R., and Tanizuka N. 2001 *Proceedings of the First CRL TDC Symposium* 19, 4

Khan Md. M. R., and Tanizuka N. 2002 *Proceedings of the First CRL TDC Symposium* 21, 5

Karpov, S., Beskin, G., Biryukov, A., Bondar, S., Hurley, K., Ivanov, E., Katkova, E., Pozanenko, A., & Zolotukhin, I. 2005 *Nuovo Cimento c* 28, 747

Karpov, S., Bad'in, D., Beskin, G., Biryukov, A., Bondar, S., Chuntonov, G., Debur, V., Ivanov, E.,Katkova, E., Plokhotnichenko, V., Pozanenko, A., Zolotukhin, I., Hurley, K., Palazzi, E., Masetti, N., Pian, E., et al., 2004 *Astronomische Nachrichten* 325, 677

Karpov, S., Beskin, G., Bondar, S., Bartolini, C., Greco, G., Guarnieri, A., Nanni, D., Piccioni, A., Terra, F., Molinari, E., Chincarini, G., Zerbi, F. M., Covino, S., Testa, V., Tosti, G., Vitali, F., Antonelli, L. A., et al., 2006a *GRB Coordinates Network* 5897, 1

Karpov, S., Beskin, G., Bondar, S., Bartolini, C., Greco, G., Guarnieri, A., Nanni, D., Piccioni, A., Terra, F., Molinari, E., Chincarini, G., Zerbi, F. M., Covino, S., Testa, V., Tosti, G., Vitali, F., Antonelli, L. A., et al., 2006b *GRB Coordinates Network* 5941, 1

Karpov, S., Beskin, G., Bondar, S., Bartolini, C., Greco, G., Guarnieri, A., Nanni, D., Piccioni, A., Terra, F., Molinari, E., Chincarini, G., Zerbi, F. M., Covino, S., Testa, V., Tosti, G., Vitali, F., Antonelli, L. A., et al., 2006c *GRB Coordinates Network* 7452, 1

Karpov, S., Beskin, G., Bondar, S., Ivanov, E., Katkova, E., and Pozanenko, A. 2007 *GRB Coordinates Network* 6603, 1

Karpov, S., Beskin, G., Bondar, S., Bartolini, C., Greco, G., Guarnieri, A., Nanni, D., Piccioni, A., Terra, F., Molinari, E., Chincarini, G., Zerbi, F., Covino, S., Testa, V., Tosti, G., Vitali, F., Antonelli, L., Conconi, P., Cutispoto, G., Malaspina, G., Nicastro, L., Palazzi, E., Meurs, E., and Goldoni, P. 2008 *GRB Coordinates Network* 7452,1

Klebesadel, R.W. et al. 1973, *Astrophys. J. L.*, 182, 85

Klotz, A., Gendre, B., Stratta, G., Galli, A., Corsi, A., Preger, B., Cutini, S., Pélangeon, A., Atteia, J. L., Boër, M., Piro, L. 2008 A&A 483, 847

Kobayashi, S. 2000, *Astron. J.*, 545, 807

Kocevski, D. & Liang, E. 2003, *Astrophys. J.*, 594, 385

Kouvelioyou, C. et al., 1993, *Astrophys. J. L.*, 413, 101

Lawrance, A. J. & Lewis, P. A. W. 1980, *J. R. Statist. Soc. B Methodological* 42, 150

Li, L-X. 2007, *Mon. Not. R. astr. Soc.*, 379, L55

Li, Z. & Waxman, E. 2008 *Astrophys. J.*,674, L65

Li, L.X. 2006 *Mon. Not. R. astr. Soc.*372, 1357

Liang, E. & Zhang, B., 2006, *Astrophys. J.*, 638, L67

Liang, E. W. et al. 2006, *Astrophys. J.*, 653, L81

Liang, E. W. & Zhang, B. 2005, *Astrophys. J.*, 633, 611

Lithwick, Y., and R. Sari, 2001, *Astrophys. J.*, 555, 540

Lithwick, Y., Sari , R., 2001, *Astron. J.*, 555, 540

Mandelbrot, B. B. 1972 *Annals of Economic and Social Measurement* 257,1

McBreen et al., 2001, A&A, 380, L31

McBreen, S., McBreen, B., Quilligan, F., Hanlon, L. F.W. 2004 *Pub. Astron. Soc. Pac.*, 312, 114

Metzger , M.R. et al., 1997, *Nature*, 387, 878

Molinari, E., Bondar, S., Karpov, S., Beskin, G., Biryukov, A., Ivanov, E., Bartolini, C., Greco, G., Guarnieri, A., Piccioni, A., et al., 2006 *Nuovo Cimento c*121,1525

Molinari, E., Vergani, S. D., Malesani, D., Covino, S., D'Avanzo, P., Chincarini, G., Zerbi, F. M., Antonelli, L. A., Conconi, P., Testa, V., et al., 2007 A&A, 469, L13

Mundell, C. G., Melandri, A., Guidorzi, C., Kobayashi, S., Steele, I. A., Malesani, D., Amati, L., D'Avanzo, P., Bersier, D. F., Gomboc, A., et al., 2007 *Astrophys. J.*, 660, 489

Nakar, E. 2007 *Physics Reports*442,166

Nardini, M., Ghisellini, G., Ghirlanda, G., et al., 2006, *Astron. Astrophys.*, 451, 821

Nardini, M., Ghisellini, G., Ghirlanda, G. 2008 *Mon. Not. R. astr. Soc.*, 386,L87

Nemiroff, R. J. 2000, *Astrophys. J.*, 544, 805

Nemiroff, R. J. 1994, *Comm. Astrophys* 17, 189

Norris, J. 2002, *Astrophys. J.*, 579, 386

Norris, J. 2002, *Astrophys. J.*, 579, 386

Norris, J. P. & Bonnell, J. T. 2006, *Astrophys. J.*, 643, 266

Nousek, J. A.; Kouveliotou, C.; Grupe, D.; Page, K. L.; Granot, J.; Ramirez-Ruiz, E.; Patel, S. K.; Burrows, D. N.; Mangano, V.; Barthelmy, S., et al., 2006 *Astrophys. J.*, 642,389

Nysewander, M., Fruchter, A.S., Pe'er A. 2008, *Astrophys. J.*, submitted

Oates, S.R. et el. 2008 *Mon. Not. R. astr. Soc.*, accepted

Omodei, N., Bellazzini, J., & Montangero, S. 2004 A&A, 414, 1177

Panaitescu A., & Vestrand W.T. *Mon. Not. R. astr. Soc.*, 387, 497

Peng, C-K., Buldyrev, Halvin, S. 1994 *Phys. Rev. E* 49, 1685

Peng, Z.-Y., Lu, R.-J., Qin, Y,-P, Zhang, B,-B. 2007 *Chin. J. of Astron. and Astrophys*7, 428

Piccioni, A., Bartolini, C., Cosentino, C., Di Cianno, A., Di Paolantonio, A., Giuliani, C., Guarnieri, A., Micolucci, E. & Ricca Rosellini, S. 1993 *MmSAI* 64, 641

Piran T. 2005, *Rev. Mod. Phys* 76, 1143

Racusin, J. L., Gehrels, N., Holland, S. T., Kennea, J. A., Markwardt, C. B., Pagani, C., Palmer, D. M., and Stamatikos M. 2008 *GRB Coordinates Network* 7427, 1

Racusin, Judith L., Burrows, D. N., Falcone, A., Zhang, B., Liang, E., Zhang, B. B. 2007 *American Astronomical Society* 211, 1007R

Racusin, J. L., Karpov, S. V., Sokolowski, M., Granot, J., Wu, X. F., Pal'Shin, V., Covino, S., van der Horst, A. J., Oates, S. R., Schady, P. 2008 *Nature*, 455, 183

Ramirez-Ruiz, E. & Merloni A. 2001 *Mon. Not. R. astr. Soc.*, 320, L25

Ramirez-Ruiz, E. & Merloni, A. 2001 *Mon. Not. R. astr. Soc.*, 320, L25

Reichart, D. et al. 2001, *Astrophys. J.*, 552, 57

Rhoads, J.E., 1997 *Astrophys. J. L.*, 487, 1

Rizzuto, D. et al. 2007, *Mon. Not. R. astr. Soc.*, 379, 619

Romano, P., Campana, S., Chincarini, G., Cummings, J., Cusumano, G., Holland, S. T., Mangano, V., Mineo, T., Page, K. L., Pal'Shin, V., et al., 2006 A&A , 456, 917

Roming, P. W. A. et. al. 2009 *Astrophys. J.*, 690, 163

Rossi, E., Lazzati, D., Rees, M. J. *Mon. Not. R. astr. Soc.*, 332, 945

Rykoff, E. S., Aharonian, F., Akerlof, C. W., Alatalo, K., Ashley, M. C. B., Güver, T., Horns, D., Kehoe, R. L., et al., 2005 *Astrophys. J.*, 631, 1032

Sahu, K.C. et al., 1997, *Nature*387, 476

Sakamoto, T., Barthelmy, S. D., Beardmore, A. P., Chester, M. M., Gehrels, N., Godet, O., Holland, S. T., Immler, S., Marshall, F. E., O′Brien, P. T., Palmer, D. M., Sato, G., Sbarufatti, B., and Starling, R. L. C. 2007 *GRB Coordinates Network* 6594, 1

Salmonson, J. D. & Galama, T. J. 2002, *Astrophys. J.*, 569, 682

Salmonson, J.D. & Galama T. J. 2002 *Astrophys. J.*, 569, 682

Salmonson, J. D. 2000, *Astrophys. J. L.*, 544, L115

Sari, R., 1997, *Astrophys. J. L.*, 489, L37

Sari, R., Piran, T., Narayan, R., 1998 *Astrophys. J.*, 497, L17

Sato, R., Ioka, K., Toma, K., Nakamura, T., Kataoka, J. Kawai, N., Takahashi, T. 2007 *Astrophys. J.*, 657, 359

Scargle, J. D. 1982 *Astron. J.*, 263, 835

Schaefer, B. 1985 *Astron. J.*, 11, 1363

Schaefer B., 1985 *Astrophys. J.*, 11, 1363

Schaefer, B. E. 2007, *Astrophys. J.*, 660, 16

Schaefer, B. E. 2003, *Astrophys. J.*, 538, L67

Schlegel, David J., Finkbeiner, Douglas P., Davis, Marc. 1998 *Astrophys. J.*, 500, 525

Schubel, M., Reichart, D., Nysewander, M., Lacluyze, A., Ivarsen, K., Crain, J. A., Foster, A., Brennan, T., Haislip, J., Styblova, J., Trotter, A. 2008 *GRB Coordinates Network* 7461,1

Stanek, K. Z., Matheson, T., Garnavich, P. M., et al. 2003, *Astrophys. J.*, 591, L17

Starling, R. L. C.; O'Brien, P. T.; Willingale, R.; Page, K. L.; Osborne, J. P.; de Pasquale, M.; Nakagawa, Y. E.; Kuin, N. P. M.; Onda, K.; Norris, J. P et al., 2007 *Mon. Not. R. astr. Soc.*384, 504

Stern, B., E. 1999, *Pub. Astron. Soc. Pac.*, 190, 31

Stetson, Peter B. 1990 *Pub. Astron. Soc. Pac.*, 102, 932

Stratta, G., Guetta, D., D'Elia, V., Perri, M., Covino, S., & Stella L. 2008 A&A, in press

Swan, H., Rykoff, E. S., Guver, T., McKay, T. A., Yuan, F., Schaefer, B. E., Quimby, R. 2008 *GRB Coordinates Network* 8807, 1

Tamagawa, T., Usui, F., Urata, Y., Abe, K., Onda, K., Tashiro, M., Terada, Y., Fujiwara, H., Miura, N., Hirose, S., Kawai, N., Yoshida, A., Mori, M., and Makishima, K., 2005 *Nuovo Cimento c* 28, 771

Taqqu, M.S., Teverovsky, W., Willinger, V. 1996 *Estimators for long-range dependence: an empirical study, Fractals* 1, 1

Thöne, Christina C., Fynbo, Johan P. U., Östlin, Göran, Milvang-Jensen, Bo, Wiersema, K., Malesani, D., et al. 2008 *Astrophys. J.*, 676, 1151

Timmer, J. & Koenig, M. 1995, A&A, 300, 707

Tingfeng, Y., et al. 2006, *Mon. Not. R. astr. Soc.*, 367, 1751

Tsutsui, R. 2008, *Mon. Not. R. astr. Soc.*, 386, L33

Van Paradijs, J. ET AL., 2000, *Ann. Rev. Astron. Astr.*, 38, 379

Vestrand, W. T., Wozniak, P. R., Wren, J. A., Fenimore, E. E., Sakamoto, T., White, R. R., Casperson, D., Davis, H., Evans, S., Galassi, M., et al., 2005 *Nature*, 435, 178

Vianello, G., Götz, D., & Mereghetti, S. 2008, A&A, in press

Vreeswijk, P. M., Milvang-Jensen, B., Smette, A., Malesani, D., Fynbo, J. P. U., Jakobsson, P., Jaunsen, A. O., Ledoux, C. 2008 *GRB Coordinates Network* 7451, 1

Walker, K.C. et al., 2000, *Astron. J.*, 537, 264

Wei, D. M. 2007, *Mon. Not. R. astr. Soc.*, 374, 525

Willingale, R. et al. 2006, *Astrophys. J.*, submitted

Woosley, S. E. 1993, *Astrophys. J.*, 405, 273

Wozniak, P., Vestrand, W., Wren, J., and Davis, H. 2008 *GRB Coordinates Network* 7464, 1

Wu, B. & Fenimore, E. 2000, *Astrophys. J. L.*, 535, L29

Yang, Z. Y., Song, L. M., Shen, R. F., Li, Z., & Lu, Y. S. 2005 *Chin. J. of Astron. and Astrophys*, 46, 117

Yi T. F., Xie G. Z., & Zhang F.W. 2008 *Chin. J. of Astron. and Astrophys*, 1, 81

Yi, T., Liang, E., Qin, Y. & Lu, R. 2006, *Mon. Not. R. astr. Soc.*, 367, 1751

Yonetoku, D. et al. 2004, *Astrophys. J.*, 609, 935

Yost, S. A., Swan, H. F., Rykoff, E. S., Aharonian, F., Akerlof, C. W., Alday, A., Ashley, M. C. B., Barthelmy, S., Burrows, D., Depoy, D. L., et al., 2007 *Astrophys. J.*, 657, 925

Yu, Y. W., Wang, X. Y., Dai, Z. G. 2009 *Astrophys. J.*, 692, 1662

Zhang, Z.-B., Deng, J.-G., Lu, R.-J., & Gao, H.-F. 2006a, *Chin. J. of Astron. and Astrophys*, 6, 312

Zhang, Z., Xie, G. Z., Deng, J. G., & Jin, W. 2006b, *Mon. Not. R. astr. Soc.*, 373, 729

Zhang, Bing, Fan, Y. Z., Dyks, Jaroslaw, Kobayashi, Shiho, Mészáros, Peter, Burrows, David N., Nousek, John A., Gehrels, Neil, 2006c *Astrophys. J.*, 642, 354.

Ziaeepour, H., Holland, S. T., Boyd, Patricia T., Page, K., Oates, Samantha, Markwardt, Craig B., et al., 2008 *Mon. Not. R. astr. Soc.*, 385, 453

Zolotukhin, I., Beskin, G., Biryukov, A., Bondar, S., Hurley, K., Ivanov, E., Karpov, S., Katkova, E., & Pozanenko, A. 2004 *Astronomische Nachrichten* 325, 675

Zou, Y. C., Piran, T., Sari, R. 2009 *Astrophys. J.*, 692, L92